

Sulfur Speciation in Urban Soils
Studied by X-Ray Spectroscopy and Microscopy

Dissertation

zur Erlangung des mathematisch-naturwissenschaftlichen Doktorgrades

”Doctor rerum naturalium”

-

im Promotionsprogramm Prophys
der Georg-August University School of Science (GAUSS)

vorgelegt von

Mareike Mathes

aus Ostercappeln

Göttingen, 2013

Betreuungsausschuss

Dr. Jürgen Thieme, Submicron Resolution X-ray Spectroscopy Beamline, Experimental Facilities Division, Brookhaven National Laboratory

Prof. Dr. Tim Salditt, Institut für Röntgenphysik, Fakultät für Physik, Universität Göttingen

Mitglieder der Prüfungskommission

Referent: Prof. Dr. Tim Salditt, Institut für Röntgenphysik, Fakultät für Physik, Universität Göttingen

Koreferentin: PD Dr. Simone Techert, Strukturdynamik (bio)chemischer Systeme, Max-Planck-Institut für biophysikalische Chemie

Weitere Mitglieder der Prüfungskommission

Prof. Dr. Sarah Köster, Institut für Röntgenphysik, Fakultät für Physik, Universität Göttingen

Prof. Dr. Hans Ruppert, Geowissenschaftliches Zentrum, Universität Göttingen

PD Dr. Jürgen Niemeyer, Abteilung Pflanzenernährung und Ertragsphysiologie, Department für Nutzpflanzenwissenschaften, Universität Göttingen

Prof. Dr. Hans Hofsäss, II. Physikalisches Institut, Fakultät für Physik, Universität Göttingen

Zusätzliches Mitglied der Prüfungskommission

Dr. Jürgen Thieme, Submicron Resolution X-ray Spectroscopy Beamline, Experimental Facilities Division, Brookhaven National Laboratory

Tag der mündlichen Prüfung: 14.05.2013

Abstract

The presented thesis is of pronounced interdisciplinary character; based on applied physics, it addresses a challenging analytical task in soil science.

The goal of this work is to specify and analyze the sulfur pool of urban soils with major anthropogenic impact, i.e. the dumping of war debris. This impact obviously influences soil composition and soil formation processes, but may, due to sulfate leaching, also be a substantial risk to urban water quality. Therefore, the sulfur load of different debris components was studied and the sulfur content of different soil samples was evaluated and correlated to different parameters, such as position of the respective soil horizon within the soil profile or location of the soil profile in the surrounding terrain.

In terms of methods, the goal of this work is to show that x-ray absorption spectroscopy and x-ray microscopy are highly suitable to address the analytical problem of sulfur speciation in complex soil samples. Two major advantages are important to stress at this point: (a) the capability to differentiate the occurring oxidation states of sulfur (speciation) and (b) the capability to combine spectroscopy with spatial resolution on the micron and sub-micron scale in terms of spectromicroscopy.

An important part of this work was to evaluate under which experimental parameters and in combination with which data analysis method x-ray absorption spectroscopy of sulfur in urban soil samples can be carried out optimally.

The following modalities of x-ray absorption spectroscopy were used: sulfur K-edge XANES spectroscopy, x-ray microscopy in terms of x-ray fluorescence imaging, and a combination of both, x-ray spectromicroscopy.

With pure XANES spectroscopy, the averaged sulfur pool of whole soil horizons as well as of single debris components was studied, applying different data analysis methods. These are peak fitting, principle component analysis (PCA), and linear combination fitting (LCF). Each of the methods gives particular insight into different sample properties, that may be mutually adaptable or complementary. PCA (when considering target transformation) and LCF are crucially dependent on an appropriate database of standard spectra.

With x-ray fluorescence imaging and spectromicroscopy, soil aggregates, debris particles, and soil solution were analyzed on the micrometer scale. These measurements show highly heterogeneous sample composition and clear gradients in sulfur speciation and oxidation state within single particles. The weathering of the anthropogenic material is therefore directly observable.

This work demonstrates the general applicability of sulfur x-ray spectroscopy and spectromicroscopy to analytical problems in urban soils. It also addresses the proper sample preparation techniques.

This work was supported by the DFG under contract number TH 445/11-1, AOBJ: 552902: "Mechanismen der Sulfatfreisetzung aus Trümmerschuttböden", which was a joint project of the working groups of Dr. Jürgen Thieme, Institute for X-Ray Physics, University of Göttingen

(affiliation when the project started) and Prof. Dr. Gerd Wessolek, Department of Ecology, Technical University Berlin.

Contents

1. Introduction to Sources, Distribution, and Analysis of Sulfur in Soils	1
1.1. Soil genesis	1
1.2. Sulfur in soils	3
1.3. Sulfur lixiviation in urban soils of Berlin	4
2. Methods and Instrumentation	7
2.1. Interaction of x-rays with matter	7
2.1.1. Absorption	8
2.1.2. Scattering	10
2.2. XAFS - X-ray absorption fine structure	11
2.2.1. XANES - X-ray absorption near edge structure	12
2.2.2. Detection methods	13
2.2.3. Sulfur XANES	16
2.3. Data analysis methods	20
2.3.1. PCA - Principal component analysis	21
2.3.2. Peak fitting	22
2.3.3. LCF - Linear combination fitting	24
2.4. μ -XRF - X-ray fluorescence microscopy	24
2.5. Beamlines used for experiments	25
2.5.1. Spectroscopy beamlines	25
2.5.1.1. SLRI - beamline BL8	25
2.5.1.2. BESSY II - beamline KMC-1	25
2.5.1.3. NSLS - beamline X15B	26
2.5.2. Spectromicroscopy and fluorescence beamlines	28
2.5.2.1. APS - beamline 2-ID-B	28
2.5.2.2. APS - beamline 2-ID-E	28
2.5.2.3. ESRF - beamline ID21	28
3. Spectroscopy Experiments	29
3.1. Sample Preparation	29
3.2. Standards	30
3.3. Consistency of data taken at different synchrotrons	35
3.3.1. Standards	36
3.3.2. Debris Components	40
3.3.3. Soils	41
3.4. Reference samples	44
3.5. Soil samples	47
3.5.1. Schulgarten	48

3.5.2.	Teufelsberg	51
3.5.3.	Peak fitting	56
3.5.4.	PCA	59
3.5.4.1.	SLRI dataset	59
3.5.4.2.	BESSY II dataset	63
3.5.5.	LCF	69
3.5.5.1.	LCF of prepared mixtures	69
3.5.5.2.	LCF of soil samples	77
3.5.6.	Error analysis	82
4.	Spectromicroscopy experiments	85
4.1.	Spectromicroscopy samples	85
4.1.1.	Resins	87
4.1.2.	Soils	90
4.1.2.1.	Soil sample spread on tape	90
4.1.2.2.	Soil sample in Kalloctyl	93
4.1.2.3.	Soil sample in LR-White	96
4.1.3.	Soil solution	101
5.	Conclusion	103
5.1.	Spectroscopy experiments	103
5.2.	Spectromicroscopy experiments	105
A.	Appendix	113
A.1.	Standard database	113
A.2.	Resins	117
A.3.	Embedding procedure LR-White	117

1. Introduction to Sources, Distribution, and Analysis of Sulfur in Soils

Sulfur is the 10th most abundant element on the earth. It is of particular environmental and biochemical importance, simultaneously being an essential nutrient and environmental pollutant. It is heterovalent, highly reactive, and exhibits a wide range of formal oxidation states, ranging from -2 in sulfides (e.g. H_2S , FeS) to $+6$ in sulfates (e.g. CaSO_4). Sulfur readily forms bonds with both, more electronegative and more electropositive elements. Therefore, it exhibits a diverse geochemical affinity and high mobility, moving freely among the lithosphere, hydrosphere and atmosphere.

While the total concentration of sulfur in a given sample can easily be determined, the speciation and quantification of different sulfur compounds still represents a challenge. Wet chemical methods of fractionation are subject to many uncertainties and potential errors [64], [79], [60], [23], [47]. Temperature resolved mass spectrometry was applied in some studies, but this method is limited to the speciation of thermally stable forms [74]. S-NMR is also of little use since the predominant sulfur isotope lacks nuclear spin. Other isotopes with spin have low natural abundance and provide weak signals with large linewidths [44], [25]. Therefore, sulfur was often called a spectroscopically "silent element".

However, synchrotron based X-Ray Absorption Near Edge (fine) Structure (XANES) spectroscopy at the K-absorption edge of sulfur ($E = 2472 \text{ eV}$) has become a common tool for sulfur speciation and quantification of the respective species in a variety of materials. Since the foundational papers of George [21] and Waldo [76], sulfur speciation on the basis of XANES was successfully applied to petroleum, coals [22], marine sediments [73], soil extracts [79], [48], whole soils [47], [37] and to various other fields.

XANES is a non-destructive method that is able to probe samples in situ in their natural environment. Depending on the specific beamline respectively endstation, different environments can be applied during measurement, such as different humidity, temperature (including cryogenic measurements), gas atmospheres, etc. Samples can be measured as solids, liquids, or in solution of any solvent. Micro- and nanoprobe also offer space-resolved measurements, analyzing heterogeneous samples in their natural state.

1.1. Soil genesis

Soil genesis (pedogenesis) or soil formation from parent material, generally rocks, takes place at the surface of the earth, under specific conditions that are characteristic to the developing soil: specific climate, litter providing vegetation, composition of soil microorganisms, etc. Soil genesis results from weathering, mineral new formation, decomposition, humification, formation

of texture, and different substance relocations originating in specific parent material (rock and litter).

Soil genesis starts at the surface and successively proceeds to deeper regions. Thereby, different layers of different properties evolve, the so called soil horizons. The uppermost horizons are litter-like, especially the organic L- and O-horizons, whereas deeper mineral horizons are increasingly rock-like. A two-dimensional vertical cut through the bulk soil is called soil profile. Human impact may alter soil formation processes drastically, either in altering the soils themselves (e.g. fertilization, mining, dumps) or the soil forming conditions (e.g. climate or vegetation). Soils can be classified by different systems, essentially a German and an international one [9], [17], [57]. In the following, those soil types and horizons, that are relevant to this work are briefly introduced (in German taxonomy). Soil horizons are divided into a few types of master horizons, subordinate properties are ascribed by pre- and suffixes, as summarized in table 1.1.

Master horizon	
horizon	Characteristics
A	mineral horizon at or close to the surface with accumulated humus
C	mineral horizon of loose rocks, little affected by pedogenic processes
M	mineral horizon, rearranged by soil tilling, with humus content
II	indicates rock formations, that are not the parent material of the horizons above
prefix/ suffix	
h	accumulation of humus (< 15 %)
j	anthropogenically applied natural substrate
y	technogenic deposit (rubble, slag, ash, waste, etc.)

Table 1.1.: Characteristics of the soil horizons relevant to this work, cp. [9], [57].

The soil types relevant to this work are Pararendzina and Kolluvisol:

Pararendzina: is a soil consisting exclusively of A- and C-horizons. It evolves in dry regions from loess, marl, carbonate gravel, sand or sandstone, but also from building rubble by accumulation of humus.

Kolluvisol: is a soil consisting of A-, M- and C-horizons, whereat the C-horizon is usually not the parent material of the soil above. It is typical on hillside toes, hollows, small valleys, etc. and evolves from humous soil fractions, that have been deposited and rearranged from other (often higher) terrain by erosion from wind and water.

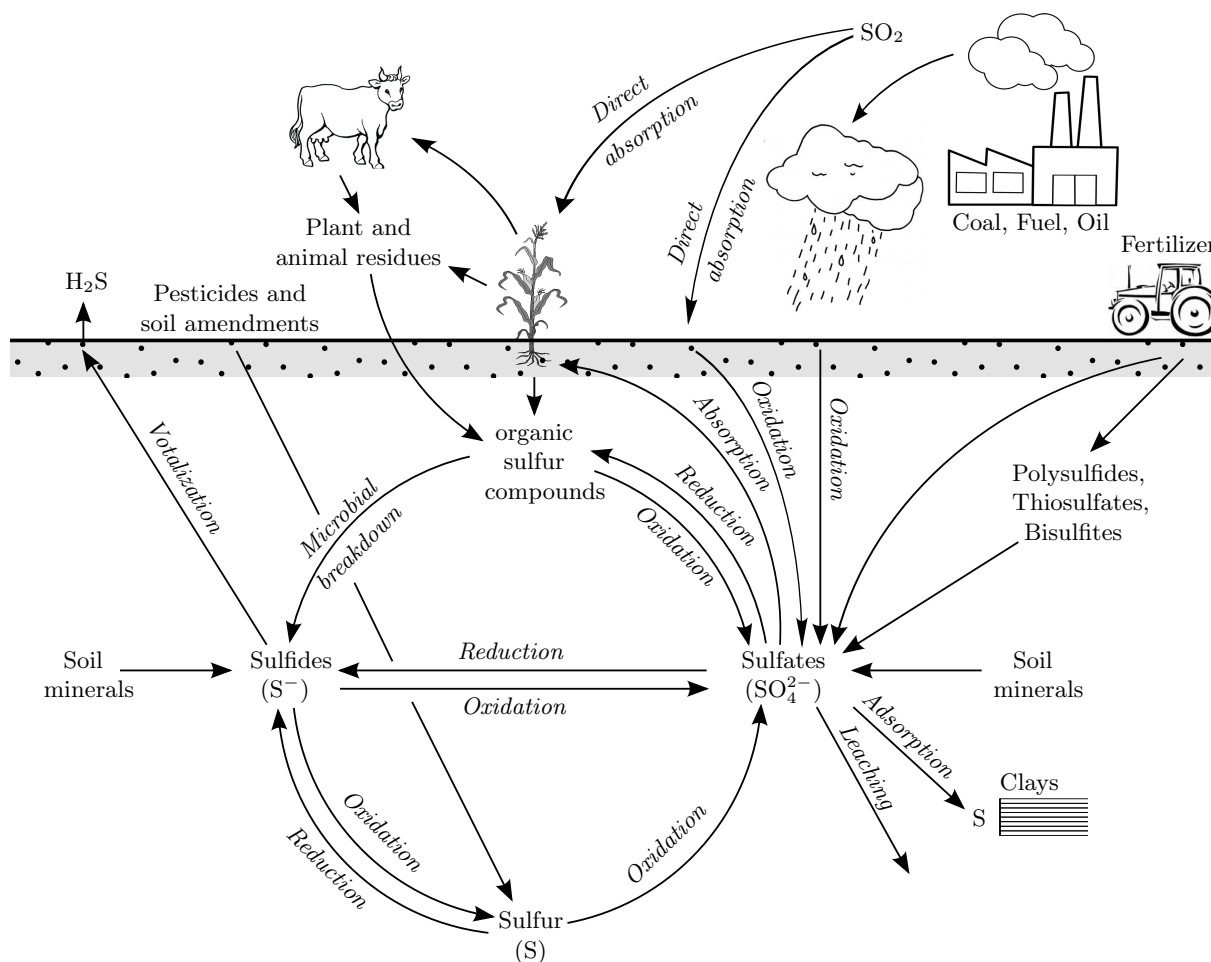


Figure 1.1.: Scheme of the sulfur cycle in soils in accordance to [64].

1.2. Sulfur in soils

Soils are the primary component in the global biogeochemical sulfur cycle and may act as source as well as sink for various sulfur species. Under reducing conditions, sulfur occurs as an anion or ligand element, forming bonds directly to metal cations. Therefore, it plays an important role in complexation of toxic trace metals. In oxidizing environments sulfur acts as a complex-forming cation and in some intermediate oxidation states, it occurs in both anionic and cationic forms. Inorganic species relevant for geochemistry and mineralogy are sulfides (S^{2-}), bisulfides (HS^-), disulfides (S_2^{2-}), other polysulfides (S_n^{1-} , S_n^{2-}), native sulfur (S^0), thiosulfates ($\text{S}_2\text{O}_3^{2-}$), sulfites (SO_3^{2-}), and sulfates (SO_4^{2-}) [16]. Organic forms are mentioned later on.

Soils vary greatly in sulfur content. The lowest concentrations are found within soils developed from sands ($\sim 0.02 \text{ g/kg}$), whereas the highest concentrations are found in soils developed in tidal areas ($\sim 35 \text{ g/kg}$). The normal range of sulfur content in terrestrial soils of humid and semihumid regions is 0.1 to 0.5 g/kg. (Gipsrendzinas however can even consist primarily of

gypsum: $\text{CaSO}_4 \cdot 2\text{H}_2\text{O}$.) In pristine H-, O- and A-topsoils of humid regions, sulfur exists mainly in organic forms (80 – 95 %). In subsoils mineral sulfur forms prevail. However, these ratios may vary significantly in urban soils. In urban soils, inorganic sulfur species may be enriched due to high amounts of anthropogenic components.

Figure 1.1 schematically illustrates the biogeochemical sulfur cycle according to [64]. Most transformation processes and changes in the oxidation state of sulfur occur within soils. The principal original source of sulfur in soils are metal sulfides of Fe, Zn, Pb, Cu, Hg, Ni, Ag, etc. from igneous rocks. Weathering of these primary minerals converts sulfides to sulfates (SO_4^{2-}), whereat the oxidation of reduced sulfur is largely a biological process of soil bacteria. Further sulfur sources for soils are fertilizers, pesticides, irrigation water, precipitation, and direct absorption of sulfur gases (SO_2). However, under aerobic conditions, minerally bound sulfur exists almost exclusively as gypsum ($\text{CaSO}_4 \cdot 2\text{H}_2\text{O}$) and, to a much lesser extent, as epsomite ($\text{MgSO}_4 \cdot \text{H}_2\text{O}$). Under anaerobic conditions, mineral sulfur is mainly retained as pyrite (FeS_2) and sometimes as native sulfur. Sulfate is used by plants and microorganisms and converted into organic forms, like sulfur containing amino acids, such as cysteine and methionine, sulfonates, and ester sulfates. The latter, in turn, are readily mineralized by microorganisms. Plant and animal residues are returned to the soil and subject to microbial decay. The majority is then incorporated into microbial biomass and hence into humus. Losses of sulfur occur by runoff and leaching; under anaerobic conditions, soils can be a source of sulfur gases (H_2S). Environmental concerns regarding the sulfur cycle focus on anthropogenically induced inputs of SO_2 into the atmosphere (however, nowadays effective emission-control systems are widely applied), leaching of SO_4^{2-} , acid sulfate soils, and formation of H_2SO_4 from pyrite in mine soils. Since sulfates are readily soluble in water (2 g/l), they are usually leached from soils of humid regions and no significant SO_4^{2-} accumulation occurs. The greatest leaching losses occur on coarse-textured soils under intense rainfall. Some soils have the capacity to retain SO_4^{2-} in an adsorbed form. Adsorption is restricted to acidic soils and is due to anion exchange of Fe- and Al-oxides and clay minerals. Typical constraints are: more SO_4^{2-} is adsorbed by the lower soil horizons than by the surface layer, adsorption increases as soil pH decreases, the clay Kaolinite adsorbs more than Montmorillonite, soils rich in Fe- and Al-oxides adsorb even more, organic matter diminishes adsorption [64], [9].

1.3. Sulfur lixiviation in urban soils of Berlin

Urban soils in the inner city of Berlin, Germany, have been dominantly influenced by anthropogenic impact during the town's settlement history. Natural soils are nonexistent, while landfills of natural or anthropogenic substrates (or mixtures) predominate. These landfills include clay, marl, sand, peat, building-, war-, and roadwork rubble, industrial and domestic waste, ashes, and slags. These substrates induce soil contamination with heavy metals and organic pollutants [40].

During the Second World War, about 30 % of all residential buildings were completely and, in addition, 45 % partially destroyed, resulting in about $75 \cdot 10^6 \text{ m}^3$ building rubble respectively debris. This rubble contained roughly $5.6 \cdot 10^6 \text{ t}$ sulfur. It was partially used to fill bomb craters, but in large parts, it was deposited in mountains of rubble. The biggest of these rubble dumps is the "Teufelsberg"-hill in the western districts of Berlin with $12 \cdot 10^6 \text{ m}^3$ debris. This hill is the

main subject of this study. Assuming ideal leaching conditions, only 25% of this sulfur reservoir may have been lixiviated into Berlin's groundwater over the past 50 to 60 years.

Nowadays, the sulfate content within near-surface groundwater aquifers is continuously rising, spaciouly exceeding the German federal limits for drinking water (240 mg/l), with peak values above 1000 mg/l, as illustrated in figure 1.2. This increase in sulfate concentration cannot entirely be explained by common sources, such as acid rain, and is assumed to originate from sulfate leaching from war debris within the urban soils. As the sulfate contents in the rivers of Berlin are also rising, mainly due to oxidation of pyrite in still open surface mines at the river's upper sections, and since the peak of sulfate leaching from war debris is still imminent, a substantial risk arises for urban water quality. Sulfate concentrations above 500 mg/l cause alterations in the taste of drinking water and may induce diarrhoea. Additionally, these high amounts of dissolved sulfate may strongly affect the infrastructure of the local waterworks, because sulfate is very corrosive to metals as well as concrete.

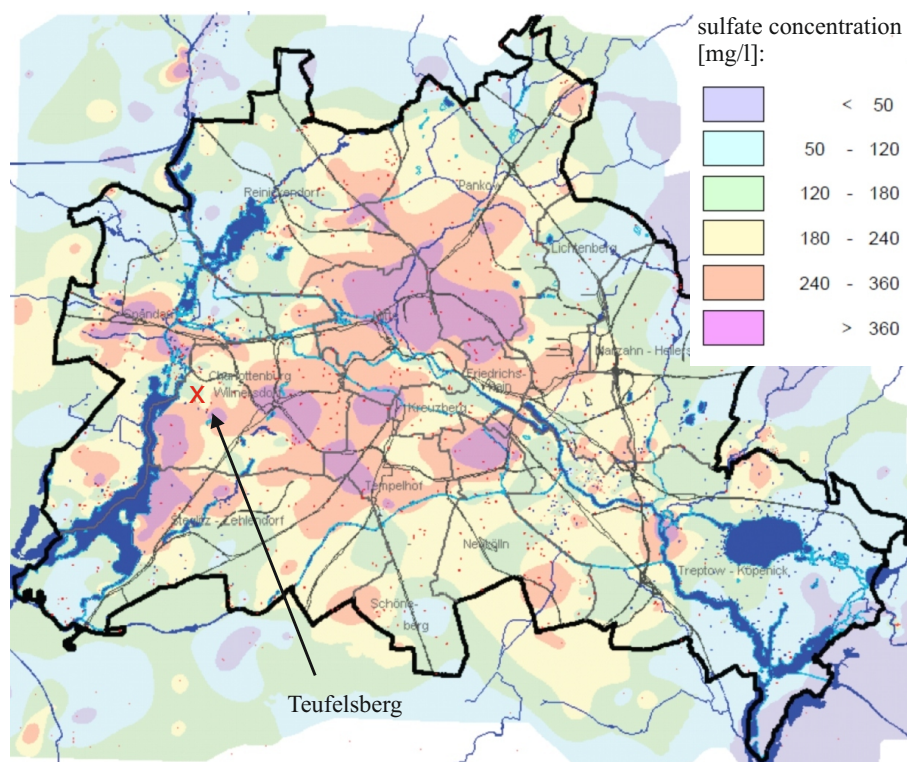


Figure 1.2.: Sulfate concentrations in the groundwater in the city of Berlin, [20].

One approach in understanding this sulfur release into the environment is to consider the relevant processes in terms of soil formation from building rubble. With XANES spectroscopy at the K-absorption edge of sulfur, it should be possible to determine the sulfur pool in these urban soils, to quantify the occurring sulfur species, and to find dependencies on e.g. hillside position as reported by Thieme et al. [69] for a hillside forest. Additionally, it allows the comparison with sulfur pools of natural soils. With spatially resolved measurements of soil aggregates and debris particles, species dependent gradients may be observed, directly showing weathering of anthropogenic parent material and sulfate lixiviation.

2. Methods and Instrumentation

This chapter gives a succinct overview of the most important theoretical foundations of this work, applied methods and experimental instrumentation. The former are mainly x-ray physics, x-ray absorption fine structure, x-ray fluorescence and data analysis methods. Experimental instrumentation is focused on the descriptions of the beamlines used for the experiments.

2.1. Interaction of x-rays with matter

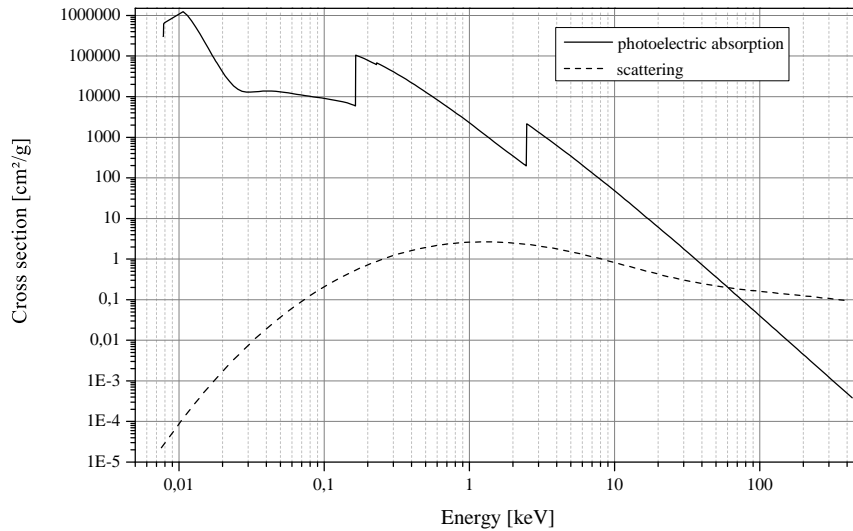


Figure 2.1.: Log-log plot of the photoelectric absorption (solid) and scattering (dotted) cross sections for sulfur as a function of energy, showing L- and K-absorption edges at 162.5 eV (L_{III}), 163.6 eV (L_{II}), 230.9 eV (L_I) and 2472 eV; data taken from NIST database [11].

The attenuation of x-rays penetrating matter is caused by three interaction mechanisms: pair production, scattering, and photoelectric absorption. As the minimal photon energy necessary for pair production is 1.022 MeV, this process is forbidden in the energy range relevant to XAFS (X-ray Absorption Fine Structure): ~ 100 eV up to several 10 keV. Figure 2.1 shows a log-log-plot of the cross sections for photoelectric absorption and for scattering as a function of energy for sulfur. Obviously, the dominant attenuation mechanism in the energy range of interest, around the K-absorption edge of sulfur at 2472 eV, is photoelectric absorption, as the absorption cross section exceeds that of scattering by about two orders of magnitude. This ratio

varies for different elements. Simplistically, the dominance of absorption over scattering grows with atomic number Z and then persists to higher energies.

2.1.1. Absorption

In photoelectric absorption, a photon of a certain energy is absorbed by an atom by transferring its energy to an inner shell electron (typically 1s, 2s, 2p), which is excited to an empty bound, quasi bound, or continuum state. The photon is annihilated in this process. Generally, the absorption cross section decreases by $\sim \frac{1}{E^3}$ as the photon energy increases, implying that x-rays become more penetrating with increasing energy, and the cross section varies with the atomic number of the absorber Z , approximately as Z^4 .

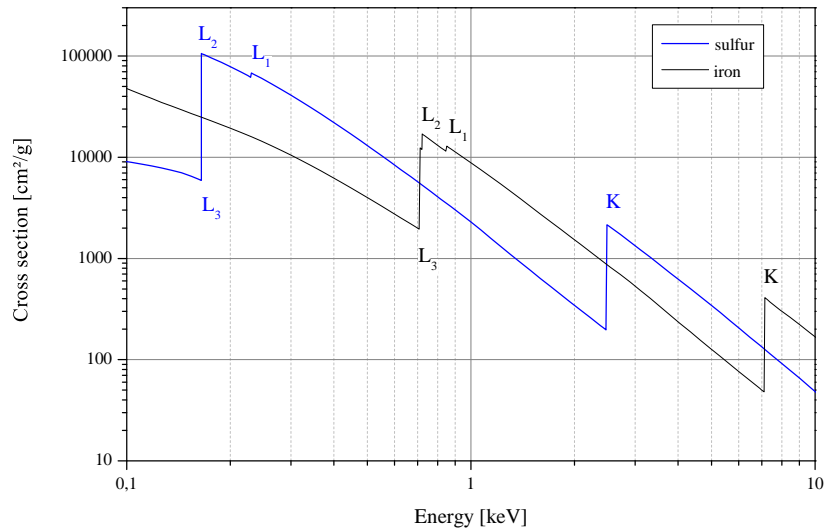


Figure 2.2.: Log-log plot of the photoelectric absorption cross sections of sulfur (blue) and iron (black). Fine structure is not shown. Data taken from NIST database [11].

Figure 2.2 shows the absorption cross sections of sulfur and iron versus x-ray energy. At certain energies, characteristic to the element, sudden increases in absorption, the absorption edges, can be observed. At these edges, the photons have sufficient energy to liberate electrons from correspondingly lower shells of the absorbing atom. The liberated electrons are called photoelectrons and possess a specific kinetic energy, depending on the incident photon energy and their former binding energy. The common nomenclature used to label the absorption edges can be found in figure 2.3. The atom, now having a core hole, is in an excited, unstable state with a finite lifetime of the order of 10^{-15} s. The decay occurs mainly via two competing processes, either as fluorescence radiation or by emission of Auger electrons. In both processes, another electron of a higher shell of the atom fills the core hole. In fluorescence, a photon is thereby emitted with an energy equal to the difference in binding energies of the two involved shells and therefore characteristic to the emitting element. In Auger decay, the energy released by the electron filling the core hole is not emitted by radiation, but is transferred to another electron.

This Auger electron is thereby excited to the continuum. The Auger process is named after the shells of the participating electrons, e.g. KLL. These processes, photoelectric absorption, fluorescence, and Auger decay, are schematically illustrated in figure 2.4, for the case of a core hole in the K shell of the atom and a KLL Auger process. The relative rates of the two decay processes are described by the fluorescence and Auger yields, ω_f and ω_a , respectively, with $\omega_f + \omega_a = 1$. For atoms of low Z , the Auger process is favored, with $\omega_f = 8\%$ and $\omega_a = 92\%$ at the K absorption edge of sulfur, for instance.

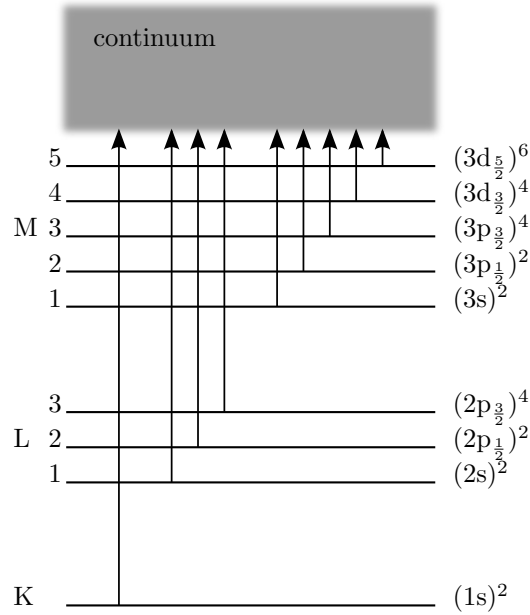


Figure 2.3.: Scheme of the common nomenclature to label the absorption edges of elements. The K edge corresponds to the energy necessary to excite an electron from the K-shell or 1s state, respectively, to the continuum; etc.

The quantity measured in absorption experiments is the linear absorption coefficient μ ($\mu = \rho_a \sigma_a$), where ρ_a is the atomic number density, namely concentration of atoms or molecules per unit volume, and σ_a the absorption cross section. The total absorption coefficient of a given sample is the sum of absorptions by each constituent element:

$$\mu = \sum_i m_i \mu_i \quad (2.1)$$

where m_i is the mass fraction of element i having the absorption coefficient μ_i .

As illustrated in figure 2.5, the incident x-ray intensity I_0 is attenuated in each infinitesimal sheet of material of thickness dx by dI . After transversing the whole material the x-ray intensity is reduced to $I(x)$ according to Beer's Law:

$$I(x) = I_0 e^{-\mu x} \quad (2.2)$$

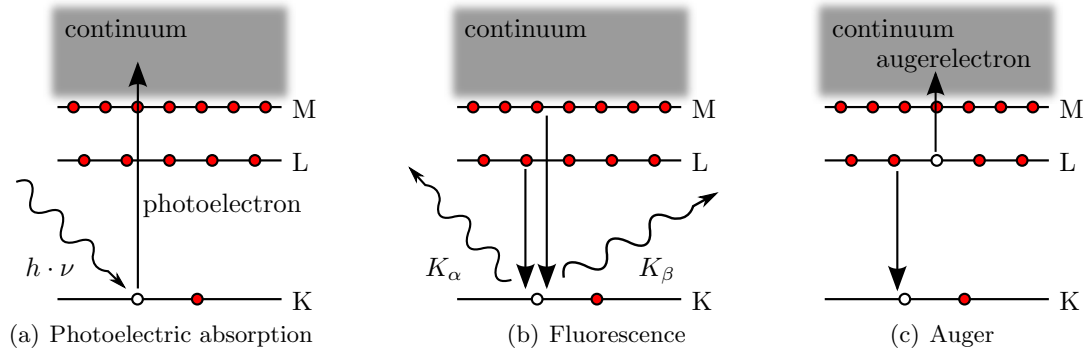


Figure 2.4.: Schematic energy level diagrams (only K, L and M shells are shown) of the photoelectric absorption process and the two decay mechanisms, fluorescence x-ray emission and Auger electron emission.

The quantity μ^{-1} is the absorption length, the characteristic length after which the initial beam intensity is attenuated to $\frac{1}{e}$. For pure solid sulfur at its K absorption edge (2472 eV) the absorption length is 22 μm below and 2.2 μm above the edge.

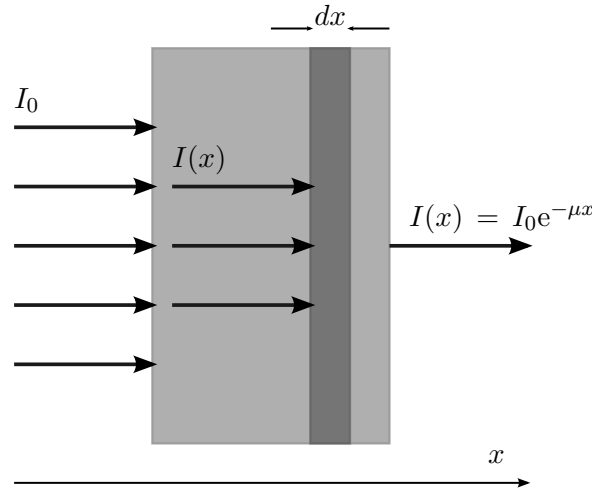


Figure 2.5.: Attenuation of an x-ray beam through a sample due to absorption.

2.1.2. Scattering

X-ray scattering occurs in two forms, elastic and inelastic scattering. In elastic scattering, a photon of specific ω and \vec{k} impinges on the sample, interacts, and another photon of the same frequency but different wavevector \vec{k}' is emitted. In inelastic scattering, not only the wavevector but also the frequency of the emitted photon differs from that of the incident photon. Generally, the emitted photon is of lower energy and therefore lower frequency. The energy difference is transferred to the sample and may induce electronic transitions.

Elastic scattering contributes significantly to the undesired background in fluorescence experiments and is described by Bragg's Law:

$$n\lambda = 2d\sin\theta \quad (2.3)$$

Here, λ is the wavelength, d the interplanar lattice distance and θ the scattering angle. A more detailed overview of the fundamentals of x-ray physics is given in several textbooks, e.g. [2], [12], [4], [65], [10].

2.2. XAFS - X-ray absorption fine structure

The element specific step-like absorption edges, described in the previous sections, are superimposed by oscillations, namely the x-ray absorption fine structure. A typical x-ray absorption spectrum can roughly be divided into two parts, the near-edge region and the region several eV above the edge, as shown in figure 2.6 for potassium persulfate. The near-edge region is called X-Ray Absorption Near Edge Structure (XANES) or Near Edge X-Ray Absorption Fine Structure (NEXAFS). Both acronyms are synonyms with XANES generally more used for harder x-rays and NEXAFS for soft x-ray experiments. The region well above the edge is called Extended X-Ray Absorption Fine Structure (EXAFS), e.g. [29].

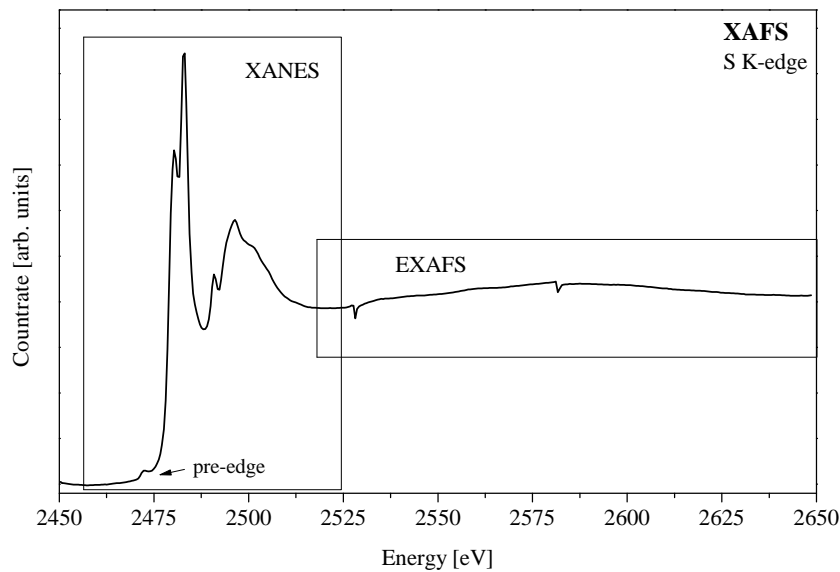


Figure 2.6.: X-ray absorption spectrum of K₂S₂O₈ with the XANES region and the beginning of the EXAFS region. Data taken from ESRF database [24].

In a more detailed consideration, the spectrum can be separated into four parts [60], which actually further separates the XANES region on the basis of the origin of its features:

The pre-edge region: The incident photon energy is below the ionization threshold and the occurring discrete peaks correspond to transitions to bound valence states. The so-called "white line", which is a common feature directly at the absorption edge, is normally also

considered to be a pre-edge peak. The phrase white line originates from early experiments, where photographic films were used to record the spectra. This line was simply the brightest on the film.

The sharply rising absorption edge: The edge itself corresponds to ionization of an inner shell electron into the continuum, as described in the sections above. Its inflection point can be used to approximately estimate the core binding energy. The position of the edge, but also shape and positions of the pre-edge features depend on the oxidation state of the absorbing atom and geometry and character of the bonding to the neighboring atoms. For sulfur, white line and absorption edge are very close in energy and are therefore superimposed.

The near edge region: The near edge region is the region located several eV above the edge. Different authors ascribe 30 to 100 eV above the edge to this region. Bianconi [8] suggested that the energy difference dividing the XANES and EXAFS region should be approximately that, at which the wavelength of the photoelectron is equal to the nearest neighbor distance. A more detailed estimate is given in [1]. For the sulfate ion, the nearest neighbor distance is only about 149 pm [32] which yields a XANES region up to 68 eV above the absorption edge. This assignment derives from the concept that the excited electron in this range is in the continuum, but with very low kinetic energy. Therefore, it is strongly scattered by the neighboring atoms and the resulting wavefunction is determined by multiple scattering effects of the first or maybe further coordination shells.

The EXAFS region: The EXAFS region directly follows the XANES region, with some potential overlap, and extends to up to 1000 eV above the absorption edge, depending on the specific element. For S, the EXAFS oscillations are relatively weak. In this region, the kinetic energy of the excited core electron is high and the plane wave approximation is valid. The electrons are only weakly scattered by the surrounding atoms and single scattering dominates. The EXAFS oscillations are then due to interference effects between the outgoing and backscattered wavefunction of the photoelectron, causing a modulation of the absorption coefficient. The EXAFS spectrum is therefore sensitive to absorber-backscatterer distances, the number of backscatterers and the atomic number of backscatterers [55], [62], [51].

2.2.1. XANES - X-ray absorption near edge structure

While the interpretation of the pre-edge peaks and the absorption edge as transitions of core electrons to respectively bound valence levels, molecular orbitals, or unoccupied antibonding states below the ionization threshold or ionization to the continuum is generally accepted, the origin of the fine structure right above the edge is still a matter of discussion. The oscillations in this region are often referred to as shape resonances, multiple scattering resonances, transitions to molecular orbitals, or something in between. Dehmer [13] describes the XANES region above the absorption edge by means of an effective potential barrier located near the electronegative atoms in the molecule, temporary trapping the excited electron. As described above, Bianconi [8] explains the near-edge features by multiple scattering of the photoelectron by the first coordination shells. Sekiyama et al. [58] built on the concept of Dehmer and described a pseudopotential barrier in molecules where electronegative ligand atoms surround a central atom, thereby separating excited states into inner- and outerwell states below and above the ionization threshold.

Stoehr [65] describes molecular orbital (MO) approaches as well as multiple scattering (MS) approaches, such as the X α Multiple Scattering Method with muffin-tin potentials, to explain and calculate the XANES structure. For further interpretation of the features above the absorption edge, he sticks to transitions of core electrons to antibonding molecular orbitals located in the continuum, but within a potential barrier. On the other hand, the post-edge features are often simply referred to as molecular orbital transitions to higher orbitals, or orbitals of the absorbing atom hybridized with orbitals of ligand atoms, e.g. [16]. Wende [78] seizes the picture first established by Dehmer, explaining shape resonances by temporary trapping of the excited core electron by a barrier of the molecular potential in a quasi-bound state, and states that these resonances can be explained without introducing any potential barrier by pure scattering of the photoelectron at the intramolecular valence region. In 2005, Rehr et al. [50] reported of their real space multiple scattering approach that can treat both, EXAFS and XANES. However, with certain differences, XANES spectra can be explained by localized electronic transitions between atomic or molecular orbitals and also by the multiple scattering of released photoelectrons by the nearest neighbor atoms, e.g. [31], [3], [50]. At present, there are various programs available to calculate XANES spectra based on molecular orbital as well as multiple scattering theories.

Concerning electron transitions from core-electron orbitals to unoccupied atomic or molecular valence orbitals, the atomic dipole selection rules apply: $\Delta L = \pm 1$, $\Delta J = 0, \pm 1$, with ΔL being the orbital angular momentum and ΔJ the total angular momentum quantum number, e.g. [65].

2.2.2. Detection methods

The x-ray absorption coefficient $\mu(E)$ can be measured either directly by measuring the transmission of the incident x-rays through the sample, or indirectly by measuring the decay products of the relaxation process following the creation of a core hole, namely the emitted electrons or fluorescence photons. Since the number of produced core holes is proportional to the number of absorbed photons and therefore to the absorption coefficient, the number of decay products, Auger electrons and fluorescence photons, is also proportional to the absorption coefficient, with a distinct ω_a / ω_f ratio. A schematic illustration of the subsequent detection methods and experimental modes is given in figures 2.7(a) to 2.7(c).

Transmission: The x-ray transmission (figure 2.7(a)) through a sample of thickness x is usually obtained by measuring the incident x-ray intensity I_0 e.g. in an ionization chamber and the x-ray intensity after the sample I_T with a second ionization chamber or a photodiode, e.g. [12], [10], [65]. The x-ray absorption coefficient can then be derived directly from Beer's Law:

$$\mu(E) = \frac{1}{x} \ln \left(\frac{I_0}{I_T} \right) \quad (2.4)$$

This detection method requires homogeneous samples, of which the maximal thickness should be roughly four times the absorption length (at the specific energy above the edge) to prevent thickness effects. For sulfur measurements for example, the maximal sample thickness would be roughly 12 μm .

Electron Yield: Electron yield measurements (figure 2.7(b)) can intrinsically be divided into different modes, of which total electron yield and Auger electron yield are the most common ones. The incident x-ray intensity is measured in the same way as for transmission measurements. In total electron yield, all electrons escaping from the sample are measured (often by electrically contacting the sample), whereas in Auger electron yield, only electrons of a specific energy, corresponding to the Auger transition, are measured. The absorption coefficient is calculated as follows:

$$\mu(E) \propto \frac{I_{EY}}{I_0} \quad (2.5)$$

This detection method is quite surface sensitive, since the escape depth of electrons is small compared to photons. At the sulfur K-edge the information depth is ~ 70 nm. Samples need to be conductive, which can for example be achieved by diluting with a small quantity of graphite.

Fluorescence Yield: For fluorescence measurements (figure 2.7(c)), the incident x-ray intensity is measured in the same way as in transmission experiments, and the fluorescence intensity is measured by either solid state fluorescence detectors or photodiodes or Lytle Detectors [63]. The fluorescence detector is usually set at 90° to the beam to minimize the scattering background, while the sample is also set at an angle to the beam, usually 45° . The x-ray absorption coefficient is derived as follows:

$$\mu(E) \propto \frac{I_F}{I_0} \quad (2.6)$$

Compared to electron yield measurements, fluorescence experiments provide bulk information (at the sulfur K-edge ~ 10 μm information depth) and are suited for thick and / or low concentrated samples. For concentrated samples, self-absorption may occur, which significantly distorts the spectra. Fluorescence x-rays generated within the sample are by a certain probability, that obviously increases with increasing concentration, reabsorbed. In essence, the peak heights are reduced and the FWHM (full width at half maximum) is increased. If the sample is made of particles, special care has to be taken, as it is not sufficient that the average concentration is low. Particle sizes need to be considerably smaller than the specific absorption length.

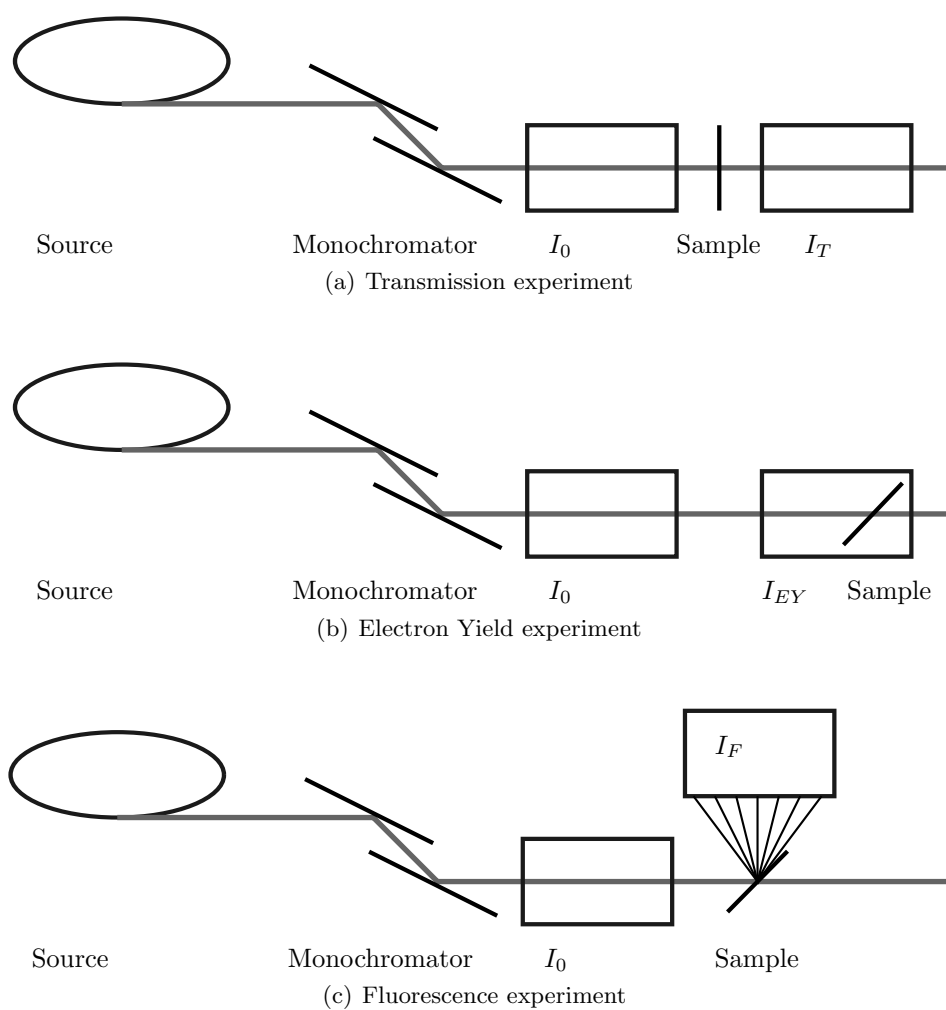


Figure 2.7.: Schematic illustration of different experimental modes and detection methods in accordance to [10]. Depicted are the x-ray beam, the x-ray source in terms of the electron storage ring of a synchrotron, a double crystal monochromator, the I_0 detector, the sample and the I_T , I_{EY} or I_F detector.

2.2.3. Sulfur XANES

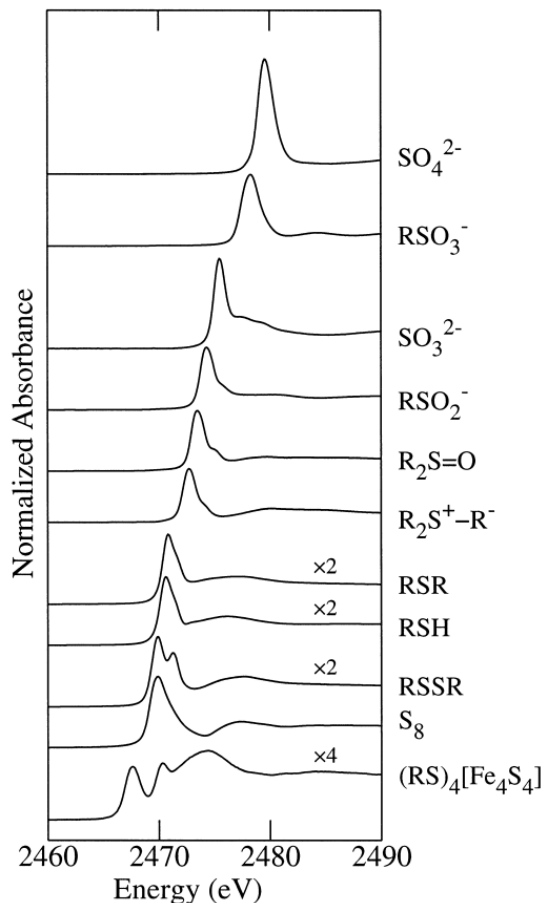


Figure 2.8.: Sulfur K-edge XANES spectra of a series of sulfur compounds of different oxidation state. R represents an organic molecule. Taken from [45]. For better visibility of the spectral features, some spectra are multiplied by two, the lowermost by four (indicated by x2 and x4 respectively). Pickering et al. ([45]) used an energy calibration where the lowest peak of sodium thiosulfate is set to 2469.2 eV.

For sulfates, the tetrahedral sulfate anion SO_4^{2-} has two unoccupied antibonding valence orbitals, a_1^* of S3s character and t_2^* of S3p character. The prominent white line, in figure 2.9 marked as **a** for Sodium sulfate, is usually assigned to the dipole-allowed $\text{S}1s \rightarrow t_2^*$ transition, $\text{S}1s \rightarrow a_1^*$ being dipole forbidden [58], [15], [42], [30]. However, Szilagyi et al. [67] state that the sulfate white line corresponds to transitions of S1s electrons to a (triply degenerate) t_2^* orbital of S4p character (which also corresponds to [53]). The broader post-edge features **b** and **c** are

As mentioned in chapter 1, sulfur is a highly reactive, heterovalent element that occurs in a wide range of formal oxidation states, ranging from -2 in some sulfides to +6 in sulfates. Typical sulfur K-edge XANES spectra of different substances covering the whole range of oxidation states are shown in figure 2.8. The spectra are sensitive to oxidation state, chemical environment, type of bonding, group symmetry, and several other boundary conditions, discussed in the following. Spectra of different species are characterized by number and positions of pre-edge peaks, position of white-line (which is normally also considered pre-edge) and absorption edge, and number and positions of post-edge features. Generally, the pre-edge and white-line peaks are attributable to transitions of sulfur 1s core electrons to the lowest symmetry-available unoccupied antibonding states. These are atomic or molecular orbitals with substantial p-orbital character [16], [44], [25]. Post-edge features are often referred to as multiple scattering resonances [72], [16], but also as further molecular orbital transitions [58], [15], [30]. The assignment of distinct peaks to specific molecular orbital transitions was performed by several researchers for a variety of sulfur compounds, essentially all being sulfides or sulfates. Sarangi et al. [53] stated more generally, that in pure ionic compounds, the sulfur K-edge white line and edge correspond to $\text{S}1s \rightarrow \text{S}4p$ and $\text{S}1s \rightarrow \text{continuum}$ transitions, respectively. In covalent binding environments, however, the transitions also include $\text{S}1s \rightarrow \varphi^*$ transitions, where φ^* represents all molecular orbitals with significant Sp atomic orbital contribution [53].

ascribed to transitions of S1s electrons to S3d-like e^* and t_2^* orbitals, respectively [58], and are often referred to as d-type shape resonances [41]. Li et al. [30] observed that post-edge features become more complicated from Magnesium sulfate to Barium sulfate and suppose a greater back-scattering efficiency of the heavier cations to be the cause.

For sulfides, the peak assignment is more dependent on the specific sulfide. Li et al. [30] investigated several metal sulfides. For pyrite, as shown in figure 2.9, they assigned peaks **a** and **b** to transitions of S1s electrons to S3p-like states mixed with metal (Fe) 3d-like states and to S3d-like states, respectively. Fleet et al. [16] divided metal sulfides into insulators and conductors, assigning the white line to transitions of S1s electrons to either S3p-like orbitals or S3p-like orbitals hybridized with empty metal 3d-like orbitals.

Pre-edge peaks are essentially observed and investigated for sulfates. Okude et al. [42] investigated pre-edge peaks in hydrated transition metal sulfates, and observed that with an increase of the number of 3d electrons in the cations, the intensity of the pre-edge peak decreases, while the main peak shifts to lower energy. They assigned these pre-edge peaks to S3p states hybridized with 3d and 4s states of the cations. Figueiredo et. al [15] investigated the influence of the sharing degree of oxygen atoms of the sulfate anions with metal cations on pre-edge peaks. They found out, that only minerals containing exclusively isolated $[\text{SO}_4]$ tetrahedra (i.e. fully hydrated sulfates) display XANES spectra with the characteristic white line that is free from any pre-edge peaks or shoulders. For copper sulfate, Szilagyi et al. [67] realized, that the pre-edge peaks are also influenced by the degree of covalency of the metal sulfate bonding.

As can be assumed from figure 2.8, the white line shows characteristic chemical shifts, depending on the measured sulfur species. These shifts are reproducible to ± 0.1 eV, identical compound, e.g. CaSO_4 as sulfate, and identical energy calibration presupposed [16]. Several groups demonstrated a nearly linear shift of the sulfur white line to higher energies with increasing formal oxidation state [22], [76], [72]. The total shift range is very large compared to other elements, about 12 eV, varying from 2470.2 eV for Pyrrhotite with a formal oxidation state of -2 (although there might be sulfides with even lower white line energy positions) to 2482.5 eV for sulfates with a formal oxidation state of +6, e.g. Calcium sulfate. The given values correspond to an energy calibration where the sulfate peak of CaSO_4 is set to 2482.5 eV, which is the energy calibration used throughout this work. The chemical shifts are generally explained by the reduced screening of the inner shell electrons from the nuclear charge with rising oxidation state (loss of valence electrons) [22], [30] [25]. The reduced screening leads to more tightly bound inner shell electrons, which is also evident from XPS (where higher binding energies are measured for increased formal sulfur oxidation states) [30]. The energy of the sulfur p orbitals is less influenced by the reduced screening than the s orbitals and therefore, the energy of S1s $\rightarrow \varphi^*$ transitions increases with an

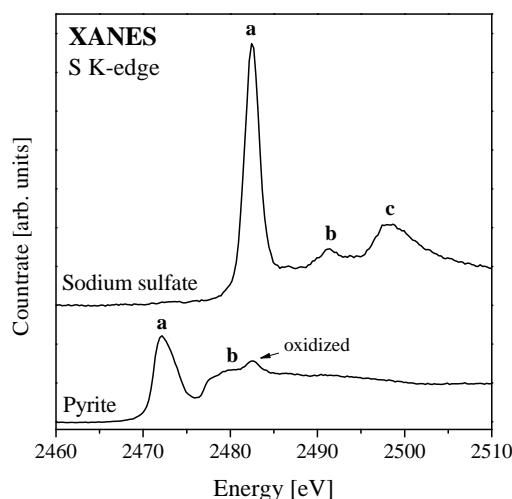


Figure 2.9.: Sulfur K-edge XANES spectra of a sulfate (Sodium sulfate) and a sulfide (Pyrite). Peaks corresponding to different transitions are marked by letters, see text for explanation.

increasing formal oxidation state [22], [25]. Additionally, for positive sulfur oxidation states, the more oxidized species form stronger bonds due to a greater overlap of sulfur and ligand orbitals, which should also result in a shift of the sulfur white line towards higher energies [30]. Sarangi et al. [53] reinforced the second aspect and reported, that the effect of sulfur oxidation state on white line position is rather indirect. The white line reflects orbital energy differences and their DFT calculations demonstrated, that the changes in atomic potential due to reduction or oxidation affect core and valence orbitals almost equally. The pronounced shift in white line position therefore mainly derives from variations in orbital mixing and energies following from bonding, as bond strength typically increases with oxidation state.

An exception from the typical progression in white line energy position are semiconducting metal sulfides with a formal oxidation state of -2. Among them are those sulfur species with the lowest white line energy positions, but their white line shifts linearly to higher energies by 2 – 3 eV with increasing band gap. As the energy of their core orbitals must be very similar, the shifts depend mainly on the φ^* orbitals, which are of type S3p mixed with metal 3d. Therefore, the shift is directly linked to their band gap [30].

Other irregularities in the relation of formal oxidation state and sulfur white line position are due to the fact that the electronic oxidation state, i.e. the actual electronic density in the valence shell, rather than the formal oxidation state influences the local binding environment [79], [25]. Formal oxidation states are assigned by using a set of certain rules, e.g. assigning all shared electrons to the more electronegative atoms or assigning shared electrons simply by analogy with similar structures. They give a simple approach for describing changes in electronic charge during redox reactions or in compounds without considering the electronic structure of the respective atoms in detail. One special caveat in assigning formal oxidation states by conventional rules arises for organic sulfur compounds, since carbon and sulfur possess the same electronegativity (2.5). Therefore, Vairavamurthy et al. [72] introduced a new term, the oxidation index. The oxidation index is assigned to sulfur compounds using their XANES white line position and is characteristic for different types of sulfur functionality. The oxidation index is derived from a linear scale in which Vairavamurthy set elemental sulfur as 0 and sulfate as +6, as shown in figure 2.10 (mainly organic compounds are considered). This new oxidation scale leads to distinct ranges of oxidation indexes for a variety of sulfur functional groups: di- and polysulfides -0.1 – 0.3, thioethers and thiols 0.4 – 0.8, thiophenes 0.8 – 1.1, sulfonium compounds 1.8 – 1.9, sulfoxides 2.1 – 2.4, sulfones 4.1 – 4.6, sulfonates 5.0 – 5.3 and ester sulfates 5.9 – 6.3. In the following, the term oxidation state will further be used, since this is the common denomination, but it will rather be meant as electronic oxidation state or oxidation index. Sarangi et al. [53] and Franck et al. [18] stressed a similar point and argued that care should be taken when measuring model compounds for comparison with spectra of unknowns, because compounds with identical formal oxidation states can show dramatic differences in sulfur K-edge spectra, depending on their molecular structure, see e.g. figure 2 in [18].

The intensity of the spectral features, i.e. the size of the white line, are also dependent on the sulfur oxidation state, as can be observed in figure 2.8. To a first approximation, the size of the white line, and therefore the respective transition probability, should be proportional to the number of available final states (S3p vacancies) and should increase with increasing valence [22], [76]. Additionally, the reduced screening of the nuclear charge with increasing valence results in contracted 1s and 3p orbitals and an increased orbital overlap, also contributing to a higher transition probability to φ^* orbitals [61].

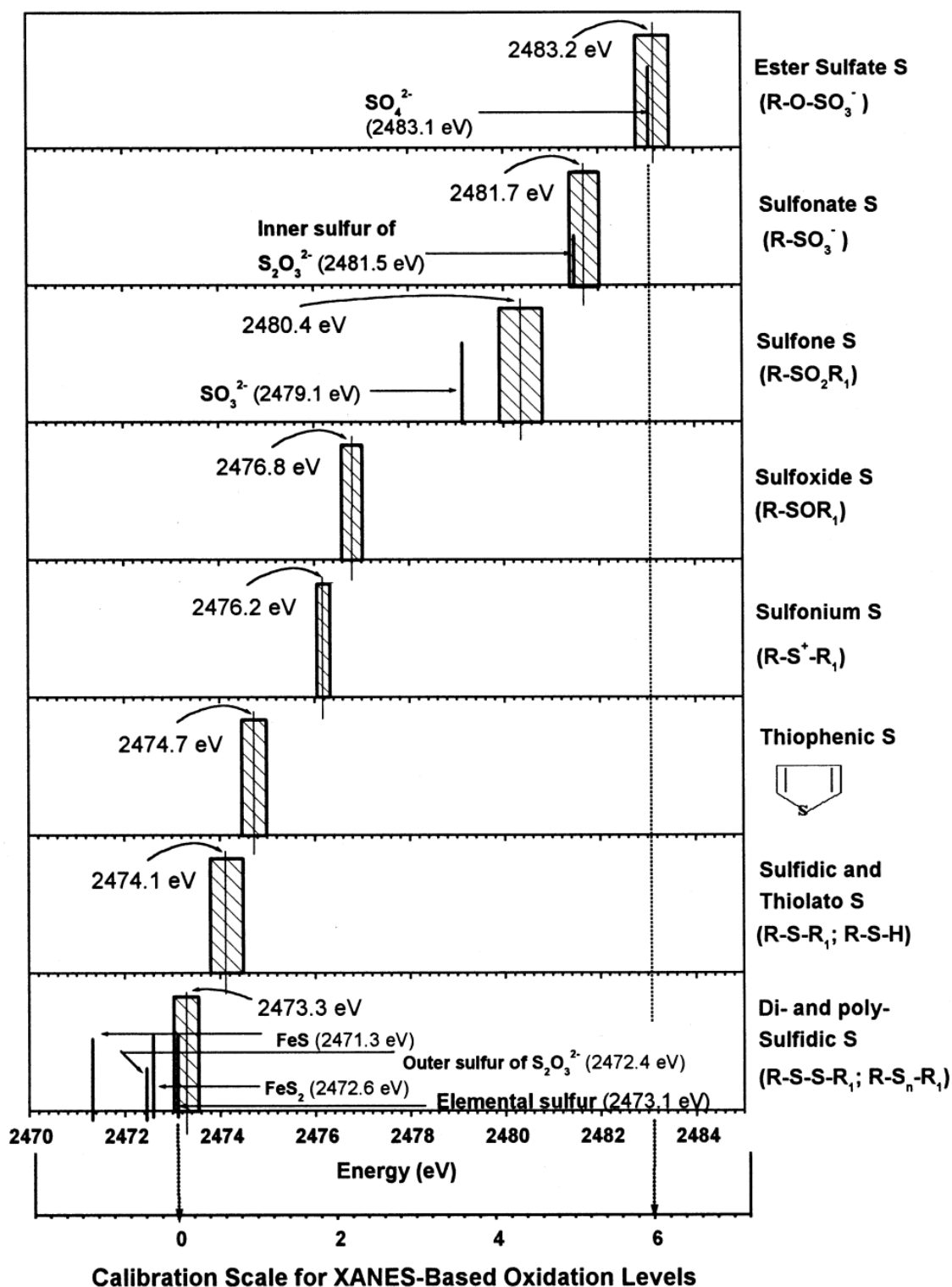


Figure 2.10.: Variation of peak energy and assigned oxidation index based on different organic sulfur functional groups. Inorganic compounds are represented by single lines. Taken from [72]. Vairavamurthy used an energy calibration, where the sulfate white line is set to 2483.1 eV.

However, sulfur compounds with similar peak energies exhibit similar peak areas [76], while for one sulfur compound, the peak area is proportional to the amount of that compound present in the sample [22], [16]. Thus, the precision to measure trace amounts of a certain sulfur fraction is also dependent on oxidation state (with a higher precision for oxidized forms).

Special attention needs to be paid to fluorescence measurements, as self-absorption effects may significantly distort the spectra. Fluorescence x-rays that are generated in the sample are to a certain probability, that is obviously dependent on concentration and sample thickness, reabsorbed. Therefore, it occurs when samples are either too concentrated or too thick, and results in attenuated and broadened white line peaks. Then, the proportionality of peak area and concentration mentioned above is no longer valid. To minimize the effect, solid samples may be ground with inert diluents (e.g. boron nitride or carbon), but in many cases, the required particle size that must be obtained is too small to be achievable by conventional grinding (e.g. $< 1\text{ }\mu\text{m}$ for sulfate) [44]. Xia et al. [79] reported, that self-absorption for sulfur measurements commonly only occurs for thick samples with a sulfur concentration $> 0.3\%$ by weight and should be no problem for thin samples ($\sim 30\text{ }\mu\text{m}$) and a sulfur concentration of $< 5\%$ by weight. Albeit, this estimation does not consider particle size effects. In principal, self-absorption can be corrected mathematically in the spectra, but in order to do that exact knowledge of the sample composition, thickness, concentration, etc. is necessary. Another possible solution are electron yield measurements, as transmission measurements would require extremely thin samples at the sulfur energy range.

Other boundary conditions that significantly affect XANES measurements are shortly mentioned in the following:

Spectra of solid and solution samples of the same compound are generally considerably different. The intensity of the major spectral features is smaller in the solid, due to reduced intrinsic symmetry. But then solids exhibit post-edge structures that are not present in solution, because of multiple scattering effects arising from long range order in the solids [44]. For particulate samples, spectra may be dramatically different for different particle sizes, an effect very similar to self-absorption and appearing in fluorescence as well as transmission measurements [45]. Spectra of compounds in solution may be strongly dependent on pH [44].

Further factors affecting the spectra are complex formation [61], [42], change in symmetry [19], [34], hydration [15], degree of covalency [67], size of band gap in semiconductors [30], strength of hydrogen bonding, solvent interaction, and the effect of a fluctuating dielectric field [25].

2.3. Data analysis methods

Spectra of natural samples usually contain partly overlapping spectral features of different species. To evaluate the sample composition and obtain a chemical speciation and reliable (relative) quantification of the occurring species, deconvolution of the spectral features of the contributing compounds is necessary. Basically, three different methods can be applied, each having certain advantages and disadvantages and each yielding specific and partly mutually adaptable information: principle component analysis (PCA), peak fitting, and linear combination fitting (LCF) [71]. Each of these methods will be introduced in the sections below.

Prior to analysis, spectra need to be energetically calibrated and normalized. Energy calibration is essential to correctly specify the chemical shift(s) of a sample and is normally performed

directly at the beamline with standard substances before the measurements. It has to be checked repeatedly during the experiments and often has to be refined later in the spectra, since energy drifts may occur over a certain period of time. These drifts are for example due to heat load to the monochromator or stepper motor hysteresis.

Normalization standardizes the spectra to remove variations due to sample thickness and concentration, sample preparation, experimental mode, detector type, and further boundary conditions, such as fill gases. Then, spectra from the same sample should be identical and differences in the spectra can be assigned to different sample compositions. Usually, a linear function is regressed to the pre-edge region and a linear or quadratic function is regressed to the post-edge region. These two functions are extrapolated to the absorption edge and their difference is set to one, while the pre-edge line (also referred to as baseline) is subtracted from the whole spectrum. It is essential, that the spectrum covers an energy range sufficient for normalization: 200 to 30 eV before the edge, so that the regression is not affected by the rising edge and 50 to 1000 eV above the edge, to exclude the near edge region from the fit. The normalized spectra then consist of a pre-edge region along zero, a step height of one and a post-edge region that roughly oscillates around one (at least the EXAFS region would oscillate around one). Serious problems can arise when trying to normalize particularly noisy spectra, especially when the noise level is close to the height of the edge-step. Then, pre- and post-edge regression may intersect in the normalization range, yielding extremely overestimated or sometimes negative absorption peaks.

For all analysis methods, spectra of standard respectively reference substances are required, at least for comparison. Standards ought to be chosen in a way, that they are likely to be compounds of the samples. It is best to have a huge database of reference spectra, to find those substances, that represent the measured samples best. ID-21 of ESRF provides a database of several sulfur reference spectra [24]. Unfortunately, little information on boundary conditions during measurement is given. Generally, standards should be measured in an environment as similar as possible to that of the actual samples, i.e. if the samples are solid / in solution the standards should be measured solid / in solution. The same applies to concentration, particle size, etc., because these conditions have a serious impact on the spectral features, as described in the sections above.

2.3.1. PCA - Principal component analysis

Principal component analysis provides insight on the minimal number of unique components present in a given set of samples. The whole dataset of measured sample spectra is regarded as one matrix. The aim is then to find an orthonormal basis of this matrix. The number of vectors of this orthonormal basis is identical to the number of unique components present in the set of samples, and the basis vectors are called principal components. Subsequent target transformation can yield those standards, that most likely represent species in the samples. It is therefore commonly combined with linear combination fitting. A detailed description of PCA is given in [35] and its application to XANES data in [52] and [6].

It is a precondition, that the dataset is factor analyzable, i.e. that it can be modeled as a linear sum of product terms. This is usually valid for XANES data that are meaningfully related, as the sample absorption at each energy is the sum of absorption of all its components (see equation 2.1). In essence, PCA uses singular value decomposition (SVD) from linear algebra to find an orthonormal basis of the measured dataset of sample spectra. SVD states that any $m \times n$ matrix

\mathbf{D} , whose number of rows is greater than or equal to its number of columns, can be written as the product of an $m \times n$ orthogonal matrix \mathbf{E} , an $n \times n$ diagonal matrix \mathbf{V} with positive or zero elements, and the transpose of an $n \times n$ orthogonal matrix \mathbf{w} : $\mathbf{D} = \mathbf{E} \cdot \mathbf{V} \cdot \mathbf{w}^t$. Then, the columns of \mathbf{E} are the eigenvectors and the diagonal elements of \mathbf{V} are the corresponding eigenvalues of \mathbf{D} . In PCA, \mathbf{D} is the data input matrix, composed of a set of measured spectra, with each spectrum being a column (or vector) of \mathbf{D} . To a first approximation the resulting eigenvectors are the orthonormal basis of the sample spectra. Usually, several eigenvalues are zero, meaning that the eigenvectors corresponding to these eigenvalues are not an important part of the orthonormal basis set construction. It is then necessary to separate the significant eigenvectors, which are those vectors that are minimally required to regenerate the data matrix: the orthonormal basis set. These significant eigenvectors are called the principal components of the dataset and are chosen by means of their eigenvalues. In addition to those eigenvectors with eigenvalues equal to zero, the vectors with the smallest eigenvalues are discarded, as these most certainly represent noise in the data. Hence, the quality of PCA is dependent on signal-to-noise ratio of the measured spectra. Ideally, the number of principal components is equal to the number of chemical compounds present in the dataset and therefore the maximal number of standards needed to model the samples. The maximal number of eigenvectors is equal to the number of sample spectra (This would imply that all measured spectra are linearly independent and no chemical compound is comprised in two spectra, e.g. a set of measured standards). However, the gained eigenvectors are purely mathematical solutions without any physical or chemical meaning. The first eigenvector is a vector along the greatest variation in some aspect of the dataset and is essentially the average of all sample data. The second eigenvector then represents the highest remaining variation and so on.

By target transformation, the principal components can be related to measured standards. In the procedure, it is determined, whether a chosen standard spectrum can be represented in the same mathematical space as is defined by the principal components. This way, those standard spectra can be identified, that most likely represent the dataset. One great advantage of this method is the fact that suspected standards can be evaluated individually without further knowledge of other species present in the sample.

2.3.2. Peak fitting

The spectrum of any sample is the weighted sum of all individual contributions from all sulfur species within the sample, cp. equation 2.1. Spectral deconvolution in terms of peak fitting benefits from the fact that the sulfur white line and absorption edge exhibit a large chemical shift dependent on oxidation state (respectively index), meaning that the occurring different species are well separated in energy. Therefore, the energy positions of the white line peaks can be used to identify the oxidation states, while the peak areas can be transformed into the percentage of the particular sulfur species present in the sample. Assuming that each group of compounds of one oxidation state produces a single peak (no pre- or post-edge features), it is possible to decompose the sample spectrum with a series of peak and step functions to account for the various white lines and respective absorption edges. This assumption is usually valid for soil samples, especially if the oxidized fraction is significantly larger than the reduced fraction, as post-edge features of the oxidized fraction are not within the fitting range, while post-edge features of the reduced fraction are negligible compared to the intense white line peaks of the

oxidized sulfur fraction. Pre-edge peaks usually do not occur in soil species. However, it should be kept in mind, that sulfoxide to sulfate white lines may be superposed with post-edge features of sulfur species of lower oxidation states.

Technically, a pure spectroscopic absorption line is Lorentzian, but the instrumental contribution is Gaussian and often dominates [14]. Additionally, line broadening due to heterogeneous samples also convolves a Gaussian onto the natural absorption line. Thus, pure Gaussian or a mixture of Gaussian and Lorentzian lineshapes are used in peak fitting by different researchers, e.g. [22], [79], [37], while arctangent functions are generally used to account for the absorption edges. In principle, each sulfur species should have its own arctangent, but this often complicates fitting (in terms of too many fitting parameters) and it is therefore a common approach to only use two arctangent functions, one for reduced sulfur species and one for oxidized sulfur species [22], [79], [72]. Manceau et al. [37] recently evaluated this approach and found out that meaningful and correct fits are obtained with only two arctangent step functions, as long as these are positioned correctly. The first step function should be positioned close to the Gaussians for reduced sulfur species, otherwise the sulfoxide fraction is easily overestimated.

As mentioned in the previous section, the peak area for a given species at a given concentration is dependent on oxidation state. This correlation was reported and analyzed on model compounds by several researchers [22], [76], [54], [43], [46], [37], as displayed in figure 2.11. The obtained calibration curves give scaling factors that account for the change in absorption cross section due to oxidation state. These scaling factors can be applied to the fitted peak areas to calculate the actual ratios of the different sulfur fractions. Obviously, the reported calibration curves vary dramatically, by roughly a factor of five. Manceau et al. [37] pointed out that the Prietzel-, Waldo- and Orthous-curve are measured in fluorescence mode and are therefore most certainly affected by self-absorption (the others are measured in TEY). Therefore, they propose to use a generic curve, in terms of the average of the three steepest curves, for data analysis. This approach seems reasonable, as the more intense peaks of oxidized species are generally more affected by self-absorption than those of reduced species, which would result in lower slopes of the calibration curves; meaning that the steepest curves are most likely the correct ones. Using a lower slope results in comparatively overestimated oxidized fractions and underestimated reduced fractions.

For the actual fitting, peak positions and FWHM can be extracted from measured standards, standard databases as provided by ESRF, or other publications (e.g. [48], [72]). However,

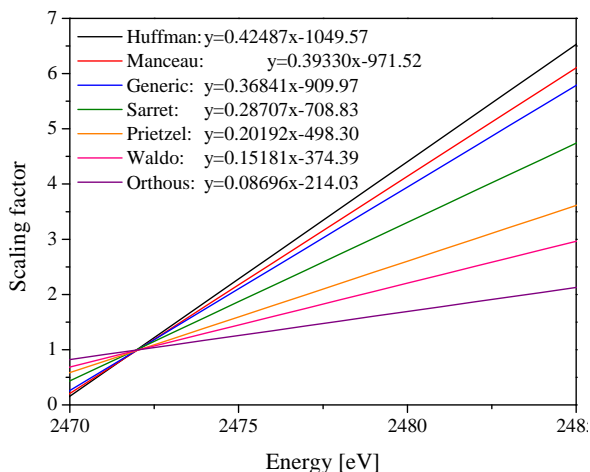


Figure 2.11.: Calibration curves to calculate sulfur fractions from fitted peak areas. The obtained scaling factors account for the change in absorption cross section do to oxidation state. The generic curve is the average of the Huffman-, Manceau-, and Sarret-curve. The scaling factors are normalized to one at the K-edge energy of elemental sulfur, 2472 eV. Diagram according to [37].

peak positions for a certain oxidation state always cover a certain range [72] and, in natural samples, usually several moieties of one oxidation state are responsible for an absorption peak. Furthermore, a standard may contain more atomic scale order than the same component in a (soil) sample, yielding a broadening of the spectral features in the sample in comparison to the standard spectrum [71]. This can be accounted for, if peak positions and FWHM are allowed to float in a certain range, or even two peaks may represent one sulfur fraction. The latter especially applies to organic sulfides, covering a range of 1 eV, cp. figure 2.10.

2.3.3. LCF - Linear combination fitting

The underlying principle of linear combination fitting, as for the other analysis methods, is the additive nature of the absorption coefficient. Therefore, it is possible to model the spectrum of a given sample with the spectra of (appropriate) model compounds or standards, respectively. By linear combination fitting, scaling factors are calculated, that, when applied to the chosen standards, yield the best representation of the measured sample spectrum. These scaling factors represent the weighted fraction of the specific sulfur compound present in the sample. Obviously, the validity of LCF strongly depends on the choice of standards used in the fit. The fitting result of some standard of a certain oxidation state does not imply explicit quantification of that precise compound, but rather of the total amount of possibly several moieties of that oxidation state. By interchanging model compounds with the same oxidation state, fitting results can be improved.

2.4. μ -XRF - X-ray fluorescence microscopy

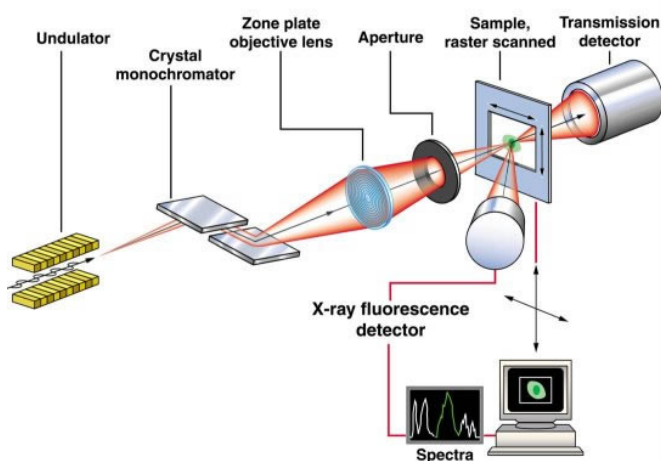


Figure 2.12.: Scheme of a typical x-ray (fluorescence) microscope, taken from http://www.aps.anl.gov/Xray_Science_Division/Xray_Microscopy_and_Imaging.

A typical layout of an x-ray microscope is shown in figure 2.12. For x-ray fluorescence microscopy capable of elemental mapping, the microscope is equipped with an energy dispersive fluorescence detector. The sample is raster-scanned through the focal spot of the x-ray beam and the full fluorescence spectrum is recorded at each scan position. As the energy of the emitted fluorescence photons is characteristic for specific elements (cp. section 2.1) and the number of emitted photons is proportional to the quantity of material present at this spot in the sample, the sample composition (restricted to the measured elements) can be obtained. Spectra need to be calibrated by standards and usually NIST

standards are used. Typically, spatial resolutions of several 100 nm are obtained, while the penetration depth is dependent on the applied incident x-ray energy and the attenuation lengths of the sample material. A detailed description of this method is for example given in [7].

2.5. Beamlines used for experiments

Experiments were performed at several synchrotrons and beamlines. Pure spectroscopy (XANES) experiments were performed at BL8, SLRI (Synchrotron Light Research Institute) in Thailand, KMC-1, BESSY II (Berliner Elektronenspeicherring-Gesellschaft fuer Synchrotronstrahlung), Germany and at X15B, NSLS I (National Synchrotron Light Source), USA. Spectromicroscopy measurements were performed at 2-ID-B, APS (Advanced Photon Source), USA, and ID-21, ESRF (European Synchrotron Radiation Facility), France. X-ray fluorescence measurements were performed at 2-ID-E, APS, USA.

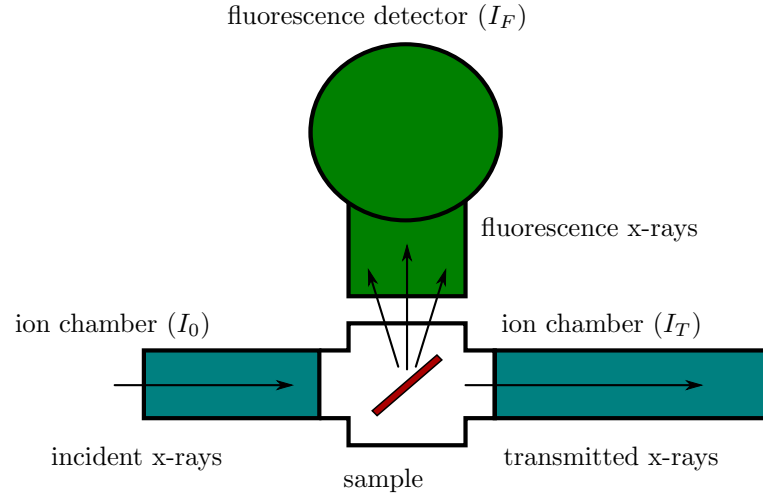
2.5.1. Spectroscopy beamlines

2.5.1.1. SLRI - beamline BL8

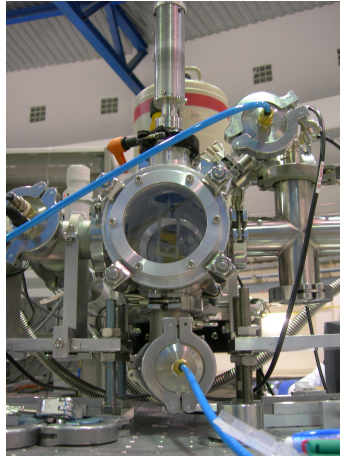
Beamline BL8 at SLRI is a bending magnet beamline, operated at an intermediate photon energy range of 1.25 to 10 keV. The energy resolution is 1×10^{-4} to 3×10^{-4} , the flux at the sample is 10^8 to $10^{10} \frac{\text{photon}}{\text{s}}$ at 100 mA ring current, and the beam size on the sample is $10 \text{ mm} \times 1 \text{ mm}$. The sample can be rotated around the vertical axis and is put at 45° to the incident beam and fluorescence detector for fluorescence measurements, as illustrated in figure 2.13(a). Several monochromator crystals are available, while Si(111) is usually used for sulfur measurements. The endstation is equipped with different detectors, which are an ion chamber for transmission measurements, a Lytle detector, that can be put in front of the sample chamber window, and a 13-element Germanium detector for fluorescence measurements. For sulfur XANES in diluted systems, the 13-element Germanium detector is used. For experiments with soft x-rays, the sample chamber is purged with Helium. A detailed description of BL8 can be found elsewhere [28], [27].

2.5.1.2. BESSY II - beamline KMC-1

Beamline KMC-1 at BESSY II is a bending magnet beamline that covers an energy range of 1.7 to 12 keV. The energy resolution is 10^{-3} at 4 keV, the flux at the sample is 10^{10} to $10^{12} \frac{\text{photon}}{\text{s}}$ at 300 mA ring current, and the beam size on the sample is $0.6 \text{ mm} \times 0.4 \text{ mm}$. The sample can be rotated around the vertical axis and moved along the beam or perpendicular to it. For fluorescence measurements, the sample is put roughly perpendicular to the beam, while the fluorescence detector is positioned at 45° to the beam and the sample, and 45° to the horizontal plane, as shown in figure 2.14. The monochromator is equipped with three sets of crystals, which are exchangeable in situ. For sulfur XANES measurements, usually Si(111) is applied. For XANES measurements, a single element Germanium fluorescence detector is available and it is possible to measure the sample current for total electron yield measurements. Transmission measurements are not possible. The sample chamber is under high vacuum conditions (10^{-8} mbar), and the samples are transferred to it using a standard Omicron system. A detailed description of the beamline can be found elsewhere [56].



(a) Schematic layout of BL8 endstation, according to [27], cp. figure 2.7



(b) Sample chamber of BL8

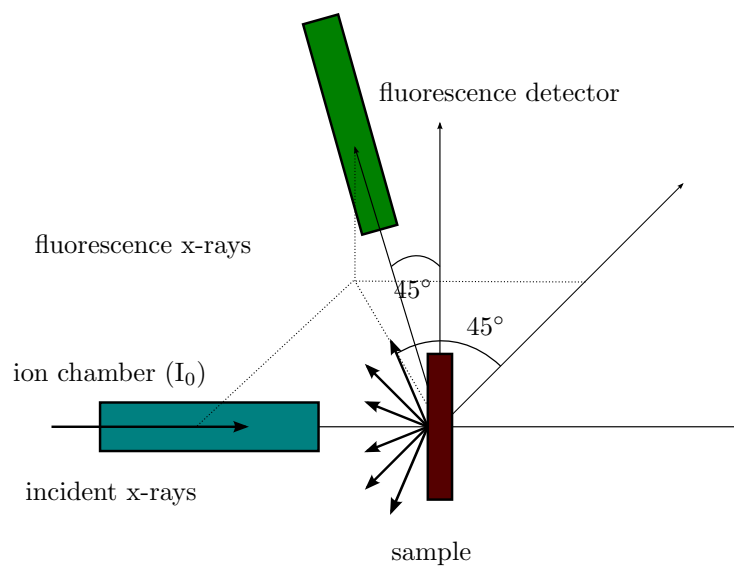


(c) Overview, BL8 endstation

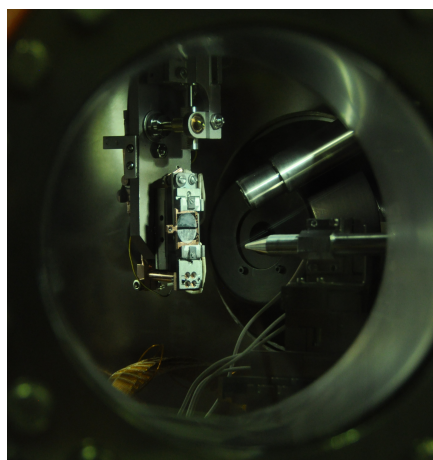
Figure 2.13.: Layout of beamline BL8 at SLRI.

2.5.1.3. NSLS - beamline X15B

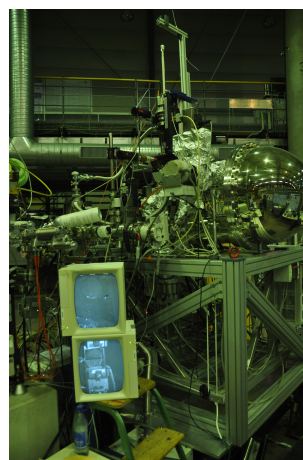
Beamline X15B at NSLS is a bending magnet beamline, operating at an energy range of 1.2 to 8 keV. The energy resolution is 2×10^{-4} , the flux at the sample is $10^{12} \frac{\text{photon}}{\text{s}}$ at 250 mA ring current and 4 keV, and the beam size on the sample is $1 \text{ mm} \times 1 \text{ mm}$. Several monochromator crystals are available, while Si(111) is usually applied for sulfur XANES measurements. The schematic layout corresponds to figure 2.7(c) and the sample can be rotated around the vertical axes. The endstation is equipped with an ion chamber for transmission measurements and a single-element Germanium fluorescence detector. For fluorescence measurements, the sample is positioned roughly at 45° to the incident beam and fluorescence detector, respectively. For soft x-ray measurements, the sample chamber is purged with Helium. A detailed description can be found in [33].



(a) Schematic layout of KMC-1 endstation



(b) Sample chamber of KMC-1



(c) Overview, KMC-1 endstation

Figure 2.14.: Layout of beamline KMC-1 at BESSY II.

2.5.2. Spectromicroscopy and fluorescence beamlines

2.5.2.1. APS - beamline 2-ID-B

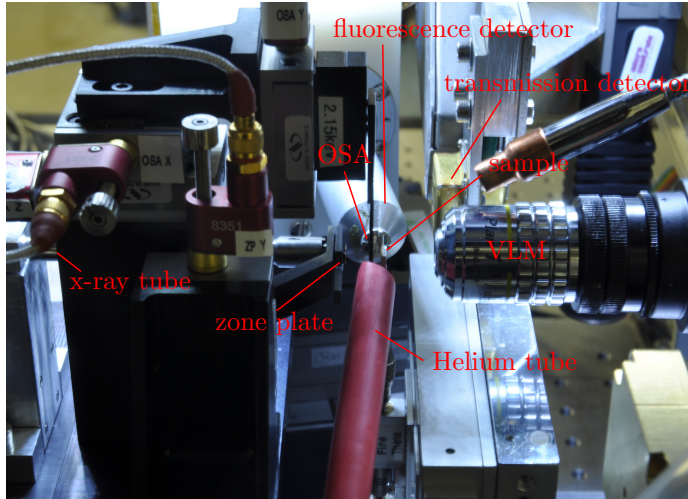


Figure 2.15.: Layout of beamline 2-ID-B.

the beam. The sample can be rotated around the vertical axes and is positioned at 15° to the beam during measurements. All experiments are performed under Helium flow. A detailed description of the beamline can for example be found in [38] and [39].

2.5.2.2. APS - beamline 2-ID-E

Beamline 2-ID-E is a hard x-ray microprobe for fluorescence mapping. The principal layout of beamline 2-ID-E corresponds to figure 2.12. It operates at an undulator source in the hard x-ray range of 7 to 10.5 keV (and 11 to 17 keV). The energy resolution is 1.4×10^{-4} , the flux at the sample is $5 \times 10^9 \frac{\text{photon}}{\text{s}}$ at 10 keV, and the beam size on the sample is $500 \text{ nm} \times 300 \text{ nm}$ (when fully focused). The beamline is equipped with two Silicon drift detectors (single element and 4-element), a Vortex detector, and ionization chambers. A more detailed description can be found in [70].

2.5.2.3. ESRF - beamline ID21

The principal layout of beamline ID21 corresponds to figure 2.12, while figure ?? shows an image of the actual realization and geometry within the sample chamber. ID21 is dedicated to x-ray imaging and spectromicroscopy (μ -XRF and μ -XANES), operating at an undulator source in an energy range of 2 to 7 keV. The energy resolution is 1.4×10^{-4} , the flux at the sample is 10^9 to $10^{10} \frac{\text{photon}}{\text{s}}$, and the beam size on the sample is $350 \text{ nm} \times 700 \text{ nm}$ (when fully focused). The beamline is equipped with an 7-element HpGe fluorescence detector, positioned 90° to the incident x-ray beam, and a photodiode for transmission measurements. The sample chamber is usually operated under vacuum (10^{-4} to 10^{-6} mbar). A detailed description can be found elsewhere [5], [66].

The principal layout of beamline 2-ID-B at APS corresponds to figure 2.12, while figure 2.15 is a photo of the actual realization. The scanning x-ray microscope is operated at an undulator source in an energy range of 1 to 4 keV. The energy resolution is 5×10^{-4} , the flux at the sample is $10^9 \frac{\text{photon}}{\text{s}}$ at 2.5 keV, and the beam size on the sample is $40 \text{ nm} \times 40 \text{ nm}$ (when fully focused). The sample can be positioned with the aid of a visible light microscope, which can be interchanged with a transmission detector (CCD) for measurements. A single-element Germanium fluorescence detector is positioned 80° to

3. Spectroscopy Experiments

Total sulfur concentration in the evaluated soil samples is in the range of 100 to 2500 ppm, cp. table 3.3, and therefore quite low. As mentioned in the previous chapter, sulfur samples for transmission experiments would furthermore have to be extremely thin and neither transmission nor electron yield measurements are feasible at all used beamlines. Thus, all spectroscopy measurements were performed in fluorescence mode.

All measured spectra are calibrated on the basis of the CaSO_4 white line and normalized as described in section 2.3. The sulfate peak is set to 2482.5 eV. Calcium sulfate was chosen for energy calibration, because it is the most abundant sulfate mineral in soils. At least two spectra for each sample were measured to check for possible beam damage, which never occurred, though. Furthermore, at BESSY II and NSLS, those beamlines with rather small spot sizes, spectra at at least two different spots on the sample were taken to account for possible sample inhomogeneities. This means, that at least three measurements were conducted at BESSY II and NSLS, e.g. two measurements at spot a and one measurement at spot b. Depending on the signal-to-noise ratio, possibly more spectra were taken. When neither beam damage nor sample inhomogeneities were detected, all spectra of one sample are averaged. For SLRI measurements, the spectra of all 13 detector signals were first examined individually and then averaged.

In several spectra of heterogeneous samples, vertical dashed lines are included, that each represent an averaged white line position of a specific oxidation state. This allows for a better orientation and ad hoc assignment. As described in section 2.2.3, the energy range for organic sulfides is quite large. Several authors distinguish between e.g. heterocyclic and exocyclic sulfides [37], although this approach does not work for all organic sulfides, as Cystine for example shows one peak in the virtually heterocyclic and one peak in the exocyclic energy range. However, in this study, the crucial differentiation is between inorganic and organic sulfide species. Since both species cover rather wide but well separated energy ranges, often these ranges rather than one averaged position for each species is marked. In doing so, the outer boundaries are represented by dashed lines, while the line separating both regions is dotted.

3.1. Sample Preparation

Sample preparation for spectroscopy experiments is straightforward and identical for all beamlines and groups of samples (standards, debris components, and soils) with respect to the main aspects. Dry and finely ground powders are applied homogeneously on sulfur free tape which is mounted on the sample holder. The used tapes are Kapton tape (Lanmar Inc.) and carbon tape (supplied by BESSY II), whereby carbon tape was only used at BESSY II. Representative images of samples and sample holders for each beamline are shown in figure 3.1. At SLRI and NSLS, sample frames are cut from plastic or cardboard sheet, respectively. One, respectively

several pieces of Kapton tape are placed on one side of the frames and the sample is applied on the sticky window areas. At BESSY II, a piece of double-faced adhesive carbon tape is glued on Cu Omicron sample holders and the samples are applied on top. The carbon tape is 1 to 2 mm thick and therefore inhibits fluorescence signals from the sample holder. In detail, sample preparation varies for each group of samples corresponding to its properties (humidity, concentration, grain size) and will be addressed in the following sections.

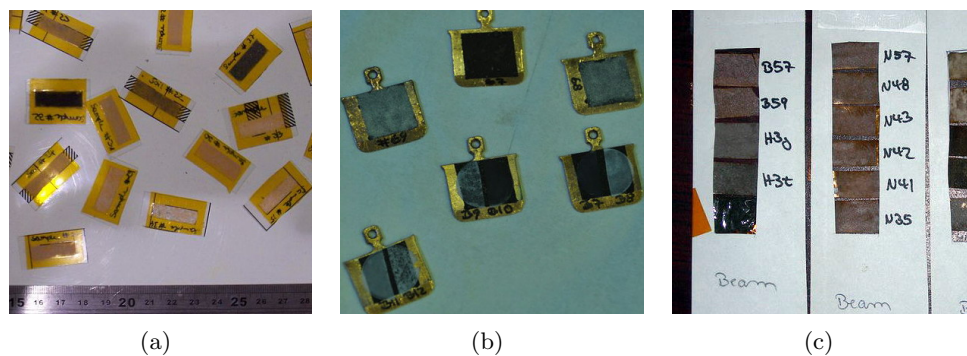


Figure 3.1.: Sample holders and sample carrying tape at (a) SLRI, (b) BESSY II and (c) NSLS.

3.2. Standards

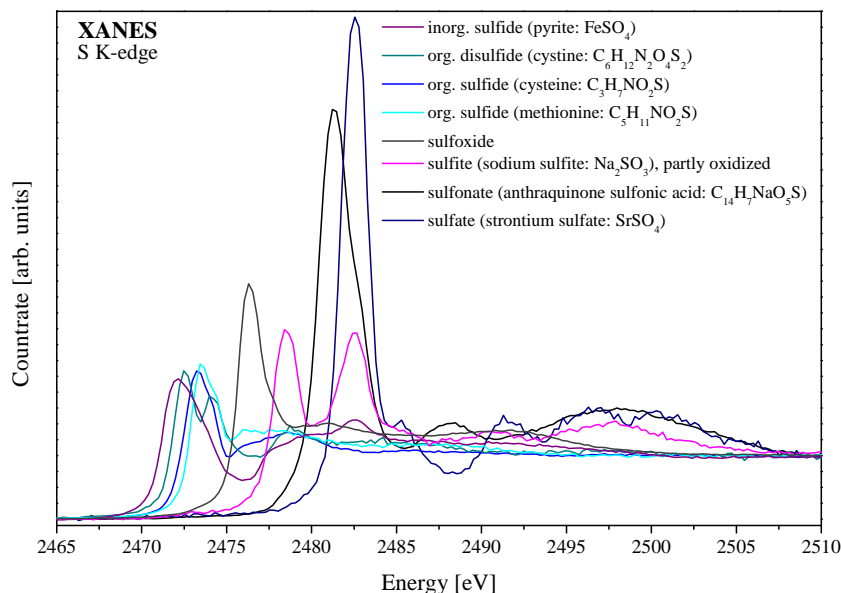


Figure 3.2.: Sulfur XANES spectra of diluted standards of different oxidation states; spectra taken at KMC-1 at BESSY II.

Spectra of standard substances of different sulfur oxidation states were taken (fig. 3.2), as well as spectra of different sulfur standard compounds in the same oxidation state (fig. 3.3). A list of all measured standards can be found in the Appendix. Model compounds that cover the whole range of possible oxidation states were chosen. The used standards are also typically abundant in soils, either in the organic or mineral soil fraction. Further standards represent abundant species in building rubble and war debris.

Spectra are shown in the energy range 2460 eV to 2510 eV, to include the whole normalization range for each sulfur species. All spectra in figures 3.2 to 3.4 were recorded at KMC-1 at BESSY II with a step size of 0.25 eV and a dwell time of 1 s. Depending on the signal to noise ratio, each spectrum was recorded at least twice and at least at two different positions on the sample. As described in section 2.2.3, white line positions vary in energy with oxidation state of the sulfur compound, ranging from ~ 2470 eV to 2482.5 eV. Qualitatively, the rise in peak height with increasing oxidation state can also be seen.

Figure 3.3 illustrates the differences in pre- and post-edge features and FWHM for substances with the same oxidation state, namely sulfates. The measured standard spectra are needed for peak fitting procedures as reference for peak positions and FWHM, as well as for deconvolution via linear combination fitting. The standard substances were used as they were purchased, but diluted to approximately the same concentrations that were found within the soil samples (tab. 3.3). Thus, any concentration dependent effects like self absorption, exemplarily shown for three standards in fig. 3.4, were prevented. In order to receive a composition as similar as possible to the real soils, clean and pure quartz sand (Merck) was used for the dilution. These mixtures were finely ground in a mortar and then applied on tape.

To exclude any influence by the described preparation methods, spectra of the sand used for dilution (fig. 3.5(a)) as well as of the used tapes (fig. 3.5(b)) were taken. The spectra in figure 3.5(a) and that of carbon tape in figure 3.5(b) were taken at KMC-1 at BESSY II, with a step size of 0.25 eV and 1 s dwell time. Kapton tape was measured at BL8 at SLRI

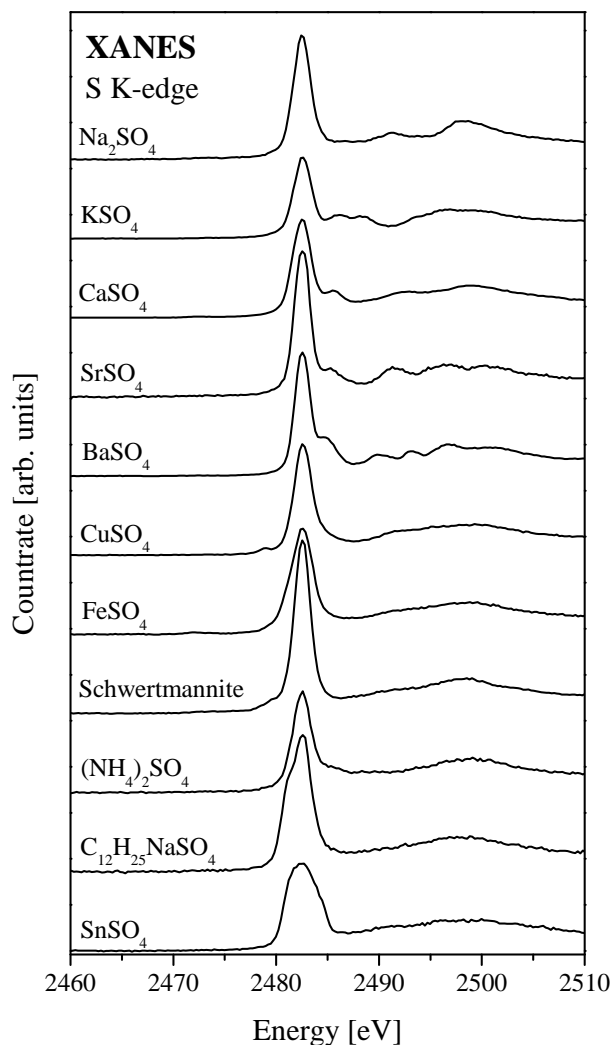


Figure 3.3.: Sulfur XANES spectra of diluted standards: various sulfates with different pre- and post-edge features; spectra taken at KMC-1 at BESSY II.

with a step size of 0.25 eV and a dwell time of 10 s. The spectra of the tapes in figure 3.5(b) cannot be normalized; they only show minimal traces of sulfur and can therefore be regarded as sulfur free. The visible sulfate traces may even originate in precipitation of sulfate bearing aerosols from building materials, that are known to be pervasive in buildings. Vertical lines in figure 3.5(a) represent averaged peak positions of the different sulfur species. Figure 3.5(a) also includes the spectrum of a fingerprint on carbon tape of the experimenter, to show how sensitive sample preparation for these XANES experiments actually is. The fingerprint yields a detailed spectrum of different sulfur oxidation states very similar to soil spectra. This is true for the general shape of the spectra, implying a similar distribution of oxidation states, as well as for signal strength, implying a similar sulfur concentration (compared to horizon c1, for instance). The sand, however, yields a very noisy spectrum, indicating very low sulfur concentration. The peak height results from normalization errors typical for very noisy spectra with only traces of sulfur, cp. section 2.3. To emphasize the low sulfur concentration within the sand used for dilution, its total fluorescence signal was compared to one of the very lowly concentrated soil samples - horizon c1 (0.06 weight-%). The result is shown in figure 3.6. Si obviously originates from sand, Fe and Cu from the sample holder, all other elements are typical in soils.

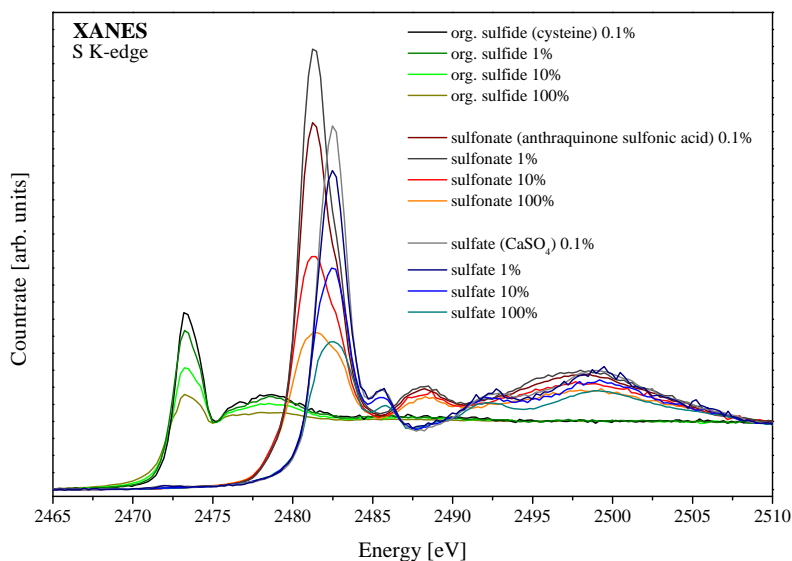


Figure 3.4.: Concentration effects on sulfur XANES spectra of standards of different oxidation states; spectra taken at KMC-1 at BESSY II; concentrations are given in weight-% standard substance to sand used for dilution.

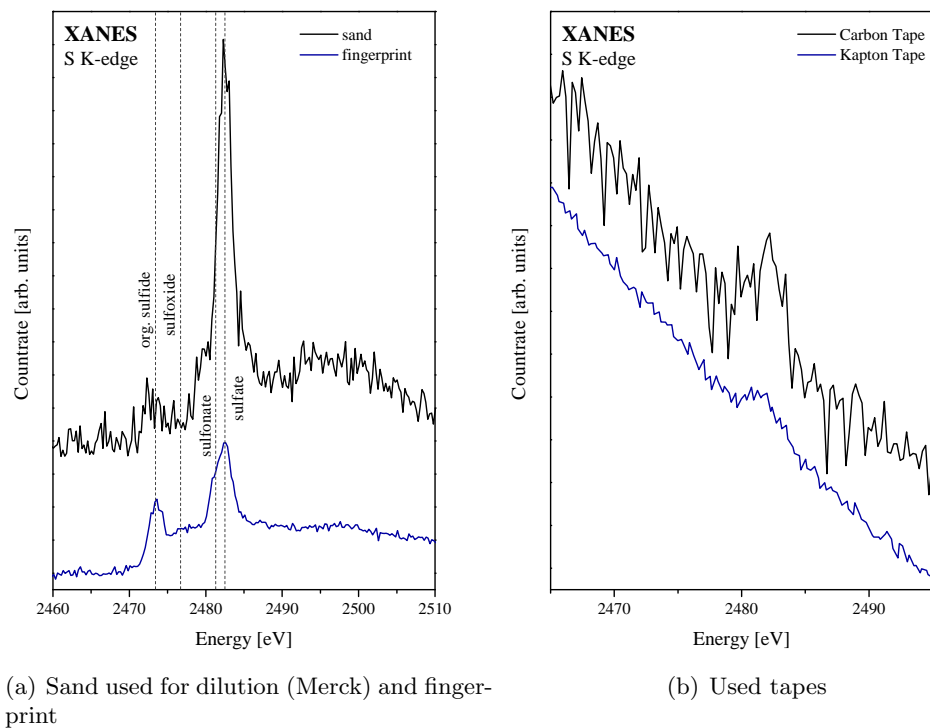
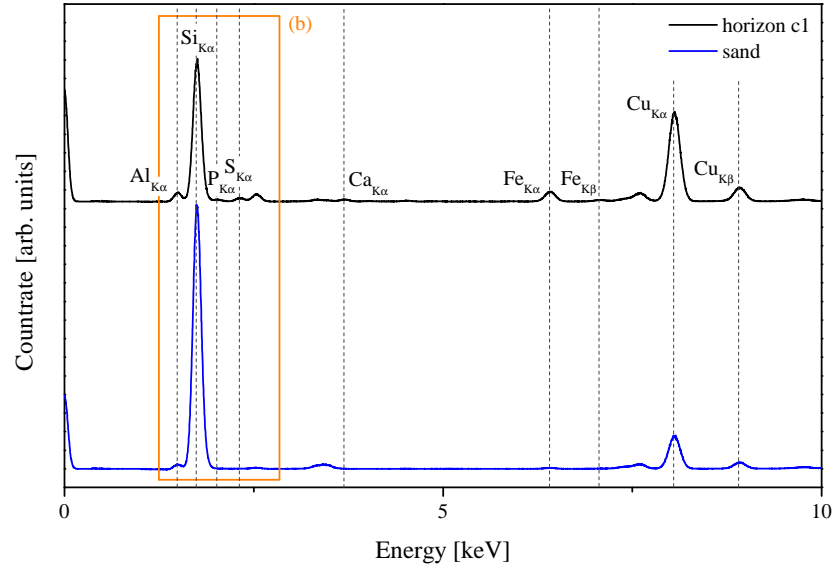
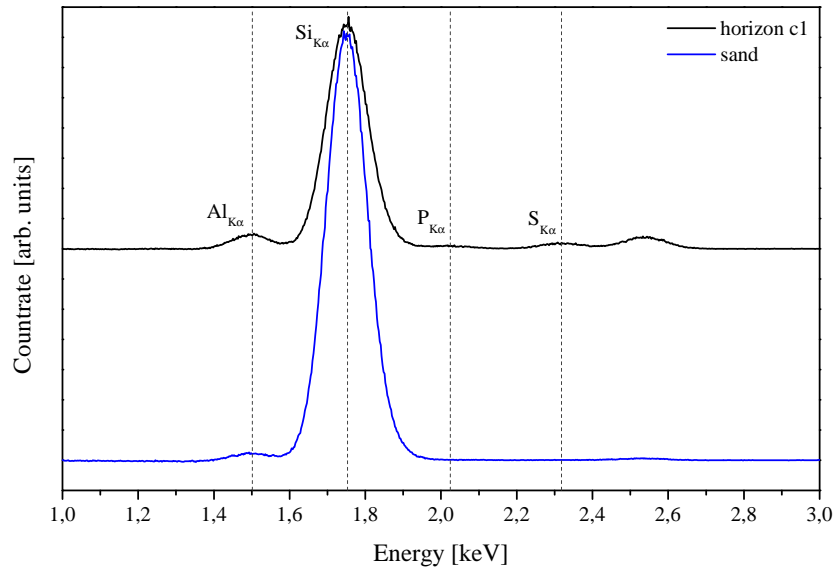


Figure 3.5.: Sulfur XANES spectra of used sample preparation equipment; spectra taken at beamline KMC-1 at BESSY II and BL8 at SLRI (Kapton Tape). The sand used for dilution yields a very noisy spectrum; the peak height results from normalization errors as described in section 2.3. The fingerprint on carbon tape yields a spectrum very similar to soil spectra. The tapes show only traces of sulfur and are regarded as sulfur free.



(a) Total fluorescence spectrum of the sand used for dilution in comparison to horizon c1, both on carbon tape; Fe and Cu from sample holder spectra measured at KMC-1 at BESSY II. A zoom into the area marked by the orange box can be found in figure (b).



(b) Zoom into region of interest

Figure 3.6.: Total sulfur content of the sand used for dilution in comparison to horizon c1 (0.06 weight-%); spectra measured at KMC-1 at BESSY II.

3.3. Consistency of data taken at different synchrotrons

Spectroscopy data were taken at three different beamlines (and synchrotrons): BL8 at SLRI, KMC-1 at BESSY II, and X15B at NSLS. These beamlines differ significantly in setup, sample stage, and conditions as well as further parameters, as described in section 2.5.1. Additionally, measurement parameters were selected differently. Dwell time and number of repetitions were adjusted with respect to beamline performance and available beamtime. Most importantly, the energy ranges for the spectra were set differently. During the first beamtimes at SLRI, only a very narrow energy range was measured: 2465 to 2495 eV and a step size of 0.25 eV. This is more or less enough for peak fitting, but it normally does not allow for a proper normalization of the spectra, cp. section 2.3. BESSY II spectra were recorded from 2450 to 2530 eV, with 0.25 eV step size, covering the whole normalization range for all sulfur species. NSLS spectra were measured over an extended range from 2400 to 2600 eV with different step sizes. Only the range from 2460 to 2520 eV was measured with 0.25 eV, comparable to BESSY II measurements. To evaluate the normalization performed on the short SLRI spectra and to prove the overall consistency of data taken at different beamlines under different conditions, several spectra were recorded at at least two beamlines. Beamline parameters are summarized in table 3.1. The spectra are shown in figures 3.7 to 3.10, starting with homogeneous samples, i.e. standards, and ending with heterogeneous samples, i.e. soils.

spot size	flux [ph/sec]	detector type	energy resolution [$\Delta E/E$]	step size [eV]
BL8 AT SLRI:				
$10 \times 2 \text{ mm}^2$	$\sim 3 \times 10^9$	13-element Ge fluorescence	2×10^{-4}	0.25
KMC-1 AT BESSY II:				
$0.6 \times 0.4 \text{ mm}^2$	$\sim 3 \times 10^{10}$	Ge fluorescence	2×10^{-4}	0.25
X15B AT NSLS:				
$1 \times 1 \text{ mm}^2$	$\sim 1 \times 10^{12}$	Ge fluorescence	2×10^{-4}	0.25

Table 3.1.: Spectroscopy beamline parameters.

In the following, all measurements of one sample are plotted on top of each other in one diagram covering the BESSY II measurement range: the full normalization range for all sulfur species. SLRI spectra are always printed black, BESSY II spectra blue and NSLS spectra red. First, all spectra are normalized as well as possible. This especially applies to SLRI spectra, as the full normalization range was not recorded. Therefore, e.g. the first global minimum after the sulfate peak was used for normalization. A comparison between these SLRI and the BESSY II or NSLS spectra gives the error induced by bad normalization. Afterwards, BESSY II or NSLS spectra were normalized in the same bad way as the SLRI spectra, to achieve the best overlap. These newly normalized spectra are called BESSY II #2 or NSLS #2 and are plotted bright blue

or bright red, respectively. A comparison between these newly normalized BESSY II or NSLS spectra and the corresponding SLRI spectra shows the actual consistency of measurements at different beamlines. To compare only BESSY II and NSLS measurements, both spectra are normalized and plotted on top of each other in one diagram. As the spot size at BESSY II and NSLS is quite small, spectra were taken at at least two different positions on the sample to account for possible sample inhomogeneities.

3.3.1. Standards

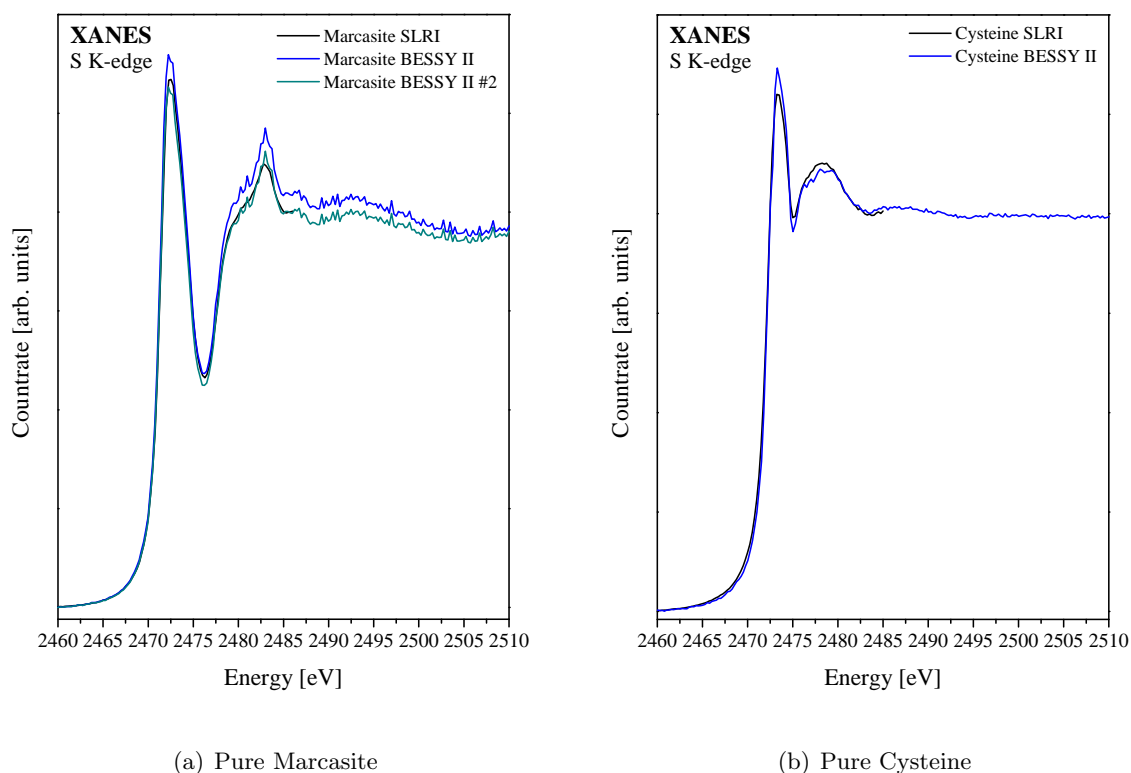
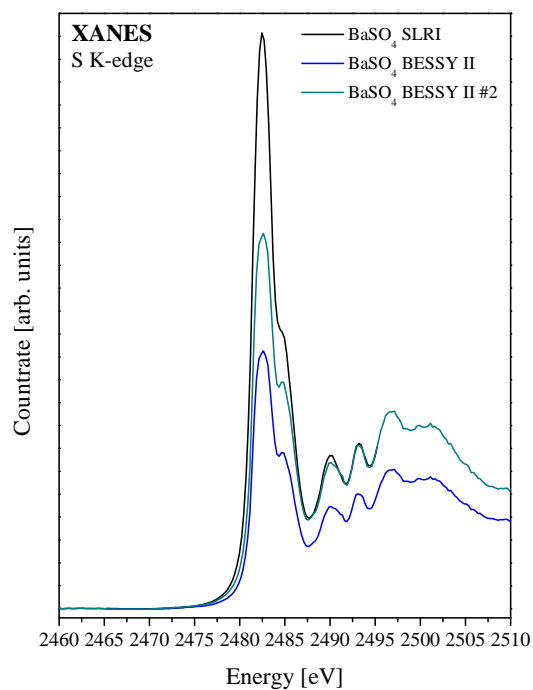
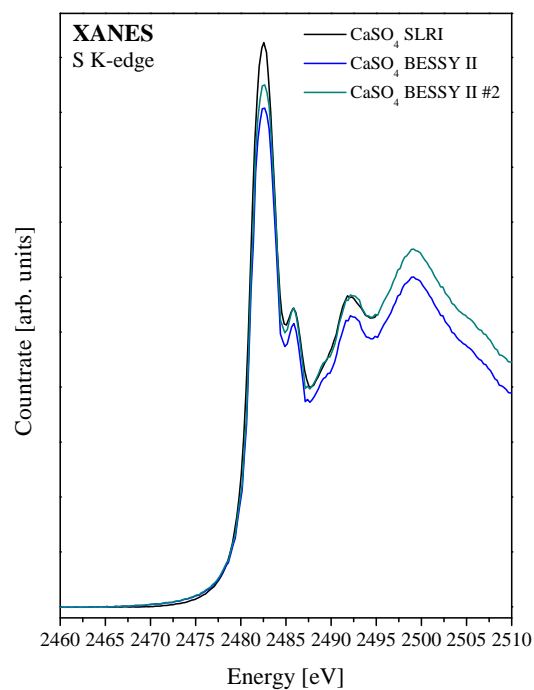
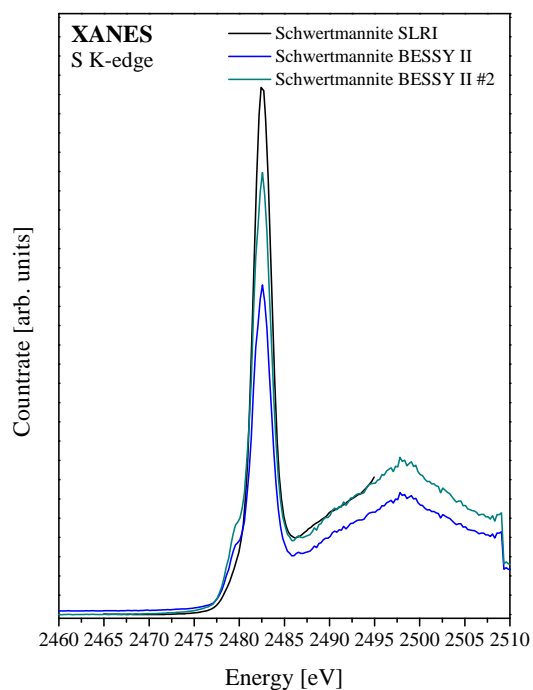
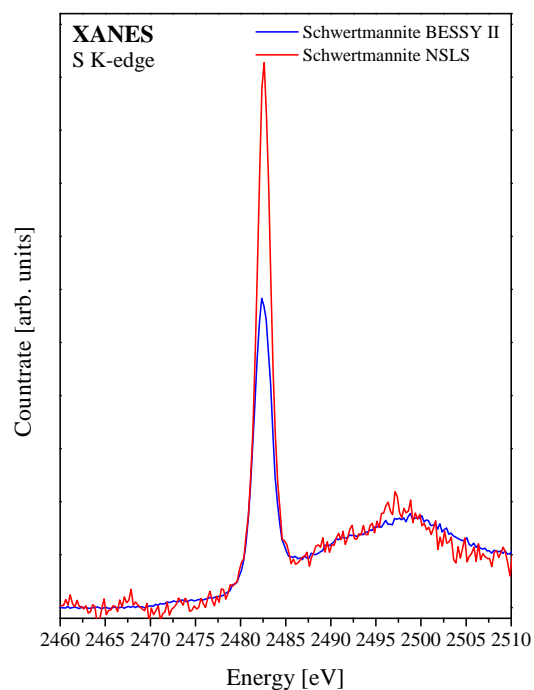


Figure 3.7.: Comparison of sulfur XANES spectra of pure inorganic and organic sulfide standards taken at BL8 at SLRI and at KMC-1 at BESSY II.

To compare SLRI and BESSY II data, two sulfides and three sulfates were chosen. Standards were used purely, as they were purchased, finely ground in a mortar and applied on Kapton tape for SLRI measurements or carbon tape at BESSY II. Dwell times were 1 s at both beamlines and each spectrum was recorded twice. The corresponding spectra are shown in figures 3.7(a) to 3.7(e). After the second normalization of the BESSY II spectra, all plots show good consistency, for Cysteine, a second normalization was not even necessary. In Marcasite, even the degree of oxidation (amount of substance oxidized to sulfate), observable on the basis of the sulfate peak, is identical. The remaining differences in peak height of the white lines are concentration de-

(c) Pure BaSO₄(d) Pure CaSO₄

(e) Pure Schwertmannite



(f) Diluted Schwertmannite

Figure 3.7.: Comparison of sulfur XANES spectra of pure sulfate standards taken at BL8 at SLRI and at KMC-1 at BESSY II, diluted sulfate standard measured at KMC-1 at BESSY II and at X15B at NSLS.

pendent. For comparison see figure 3.4. As all standards are used purely, self-absorption effects are certain to occur. The applied preparation method does not guarantee uniform and reproducibly thick films, and different tapes were used at both beamlines, most certainly yielding different sample concentrations for both measurements. However, the variance in peak height of the white line due to different sample concentrations is negligible with respect to judgment of the consistency of the measurements performed at different beamlines. Standard spectra used for data analysis were taken from standards diluted with quartz sand. To minimize self-absorption effects the sulfur concentrations in those standards were chosen similarly to those within the analyzed soils.

The Schwertmannite spectrum measured at BESSY II, shows a shoulder at the low energy side of the sulfate white line, that will be discussed in section 3.5.1.

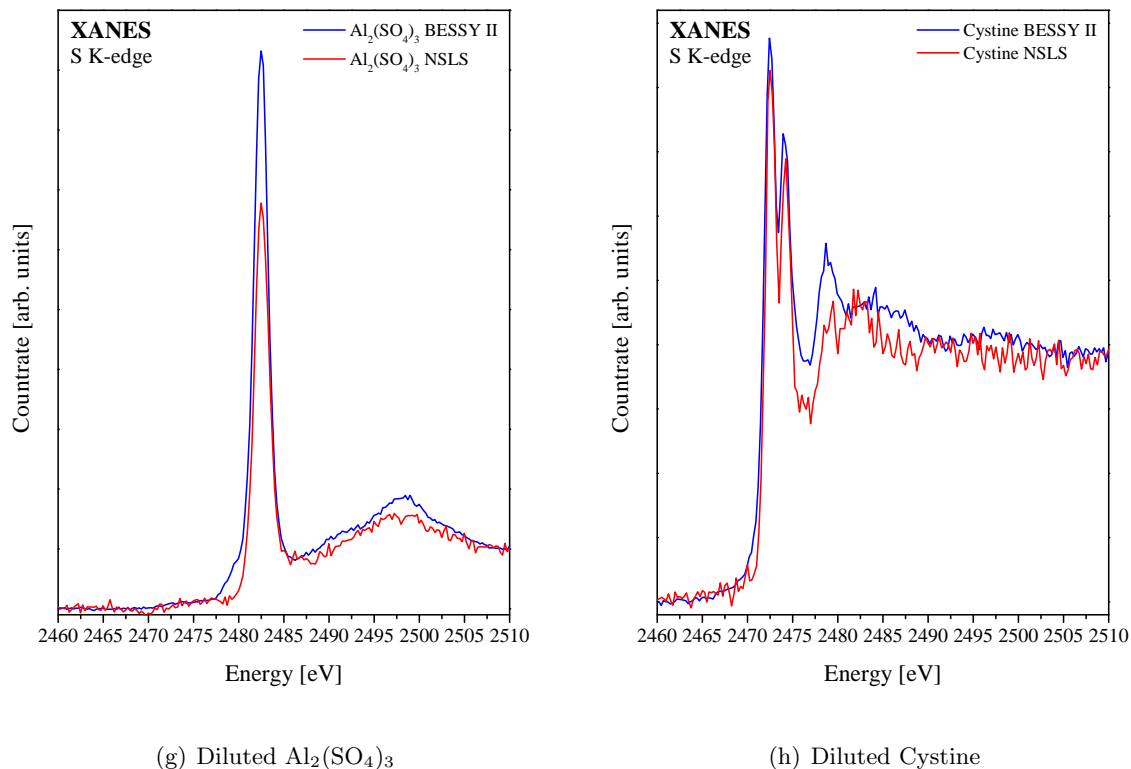


Figure 3.7.: Comparison of sulfur XANES spectra of diluted sulfate and sulfide standard taken at KMC-1 at BESSY II and at X15B at NSLS.

To compare BESSY II and NSLS data, two sulfates and one sulfide were chosen. In this case, standards were used as they were purchased, but diluted with quartz sand (as described in section 3.2) by a factor of 1:1000 in weight-%. Beamline X15B at NSLS was very sensitive to high concentrations of quartz sand, resulting in very noisy spectra and prevalent broad peaks that could not be explained by absorption. Exemplary spectra are shown in figure 3.8. In hindsight, this is easily understood reconsidering Bragg's Law:

$$n\lambda = 2d \sin \theta$$

and

$$\lambda = \frac{hc}{E}$$

Quartz crystals possess different d spacings, depending on lattice plane. Quartz (100) yields the strongest diffraction peak with $d = 3.342 \text{ \AA}$. As described in section 2.5.1, all samples at X15B at NSLS were positioned at 45° to the beam and detector, respectively. Assuming a maximal error of 5° in the positioning of the sample, $2d \sin \theta$ yields an energy range of roughly 2430 to 2890 eV for the occurrence of Bragg peaks, while the energy range of the sulfur XANES measurements covers 2400 to 2600 eV (with focus on 2460 to 2530 eV). The overlap and therefore the possible occurrence of Bragg peaks in the spectra is obvious. This problem can be accounted for by usage of other diluents or detuning of the sample.

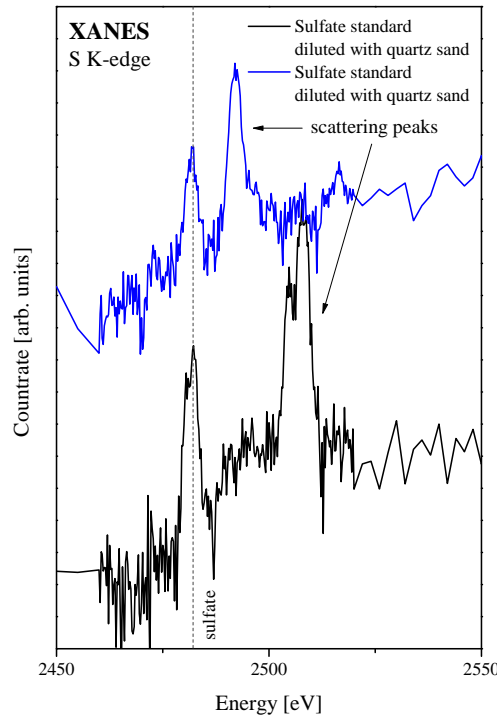


Figure 3.8.: Sulfur XANES spectra of diluted sulfate standard taken at X15B at NSLS. Silicon Bragg peaks occur at 2492 and 2508 eV, respectively.

Except for the signal to noise ratio and previously addressed differences in the peak height of the white line, the data show good consistency. The Aluminum sulfate spectrum measured at BESSY II shows a similar feature at the low energy side of the white line, as observed in Schwertmannite, cp. section 3.5.1.

3.3.2. Debris Components

Samples of debris components were finely ground and without further treatment applied to either Kapton or carbon tape. Details to all reference samples are given in table 3.2.

To compare SLRI and BESSY II data on the basis of debris components, the coal dc6 was chosen (fig. 3.9(a)). At SLRI, the spectrum was recorded twice, with a dwell time of 10 s, at BESSY II three times with a dwell time of 1 s. Vertical lines in the diagrams represent average peak positions for each sulfur species from sulfoxides to sulfates. For sulfides, the whole range for inorganic respectively organic sulfides is given. The dashed lines mark the beginning of the inorganic sulfide and the end of the organic sulfide range; the dotted line represents the border between both ranges. After the second normalization of the BESSY II spectrum, both measurements are identical, except for signal to noise ratio.

To compare BESSY II and NSLS data, the clay brick dc16 was chosen (fig. 3.9(b)). At BESSY II, the spectrum was recorded three times with a dwell time of 1 s, at NSLS twice with a dwell time of 5 s. Except for a small difference in the peak height of the white line, addressed in the previous section, both spectra are identical.

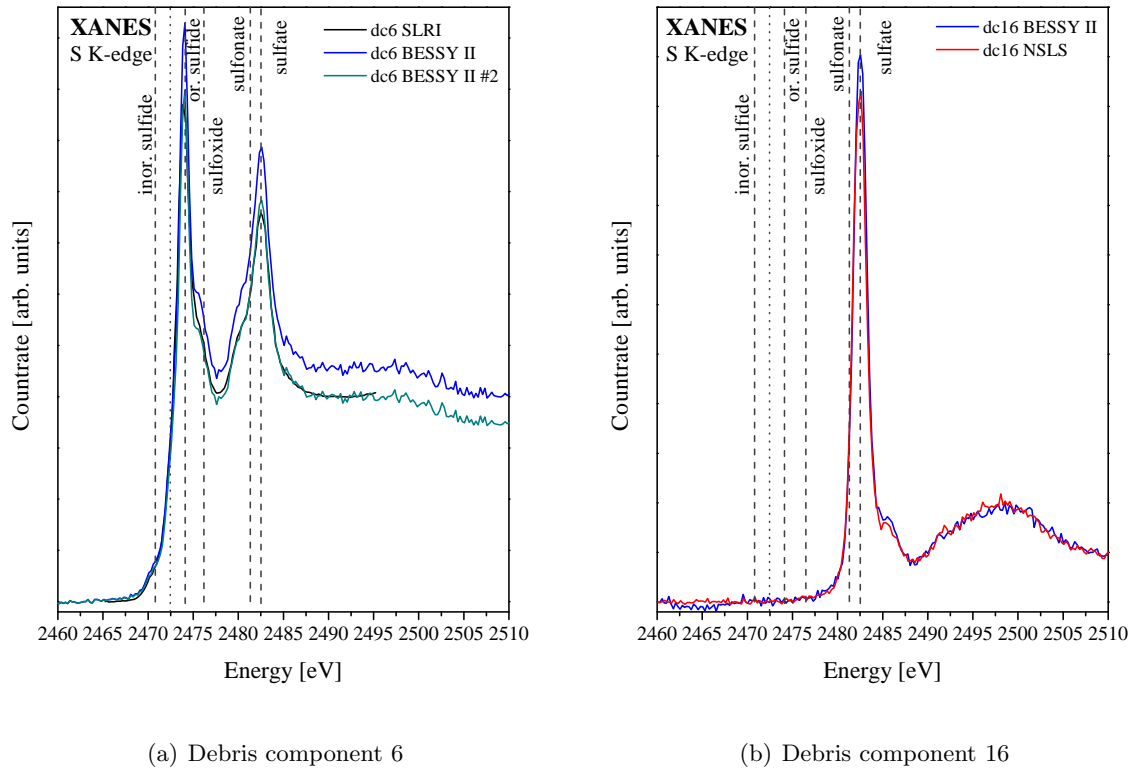


Figure 3.9.: Comparison of sulfur XANES spectra of debris components taken at BL8 at SLRI, at KMC-1 at BESSY II and at X15B at NSLS.

3.3.3. Soils

To compare SLRI, BESSY II and NSLS data on the basis of soils, one of the soil profiles laid out at the Teufelsberg, profile g, was used. For details of the samples see table 3.3. Soil samples were dried and finely ground and spread on Kapton or carbon tape. Details of soil sample preparation are given in section 3.5. The corresponding spectra are shown in figures 3.10(a) to 3.10(f). Spectra at SLRI were measured twice with a dwell time of 5 s, at BESSY II three to five times, depending on signal to noise ratio, with a dwell time of 1 s, and at NSLS twice with a dwell time of 5 s.

Spectra of the uppermost horizons with high fractions of many sulfur species, shown in figures 3.10(a) and 3.10(b), display well agreement of SLRI and BESSY II data after the second normalization. Remaining differences are due to inherent inhomogeneities of the samples.

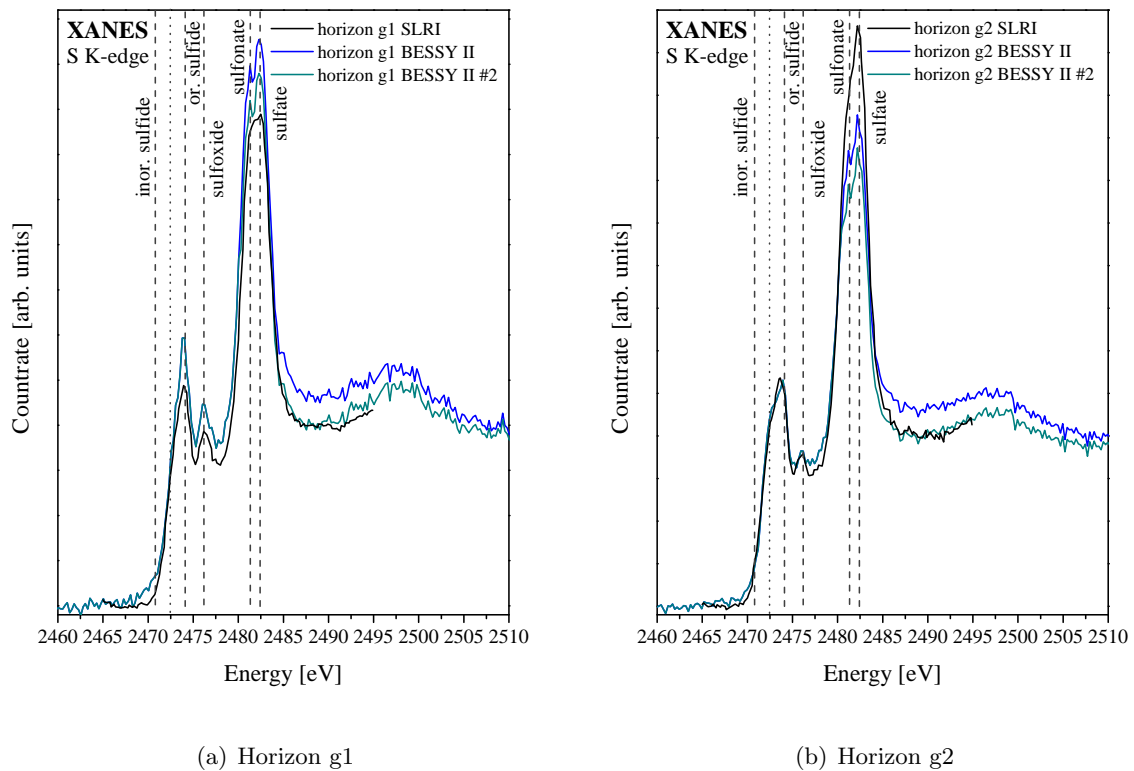
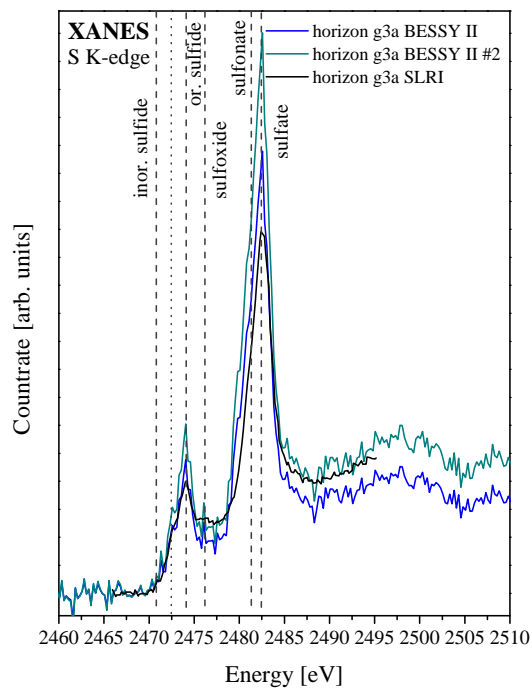
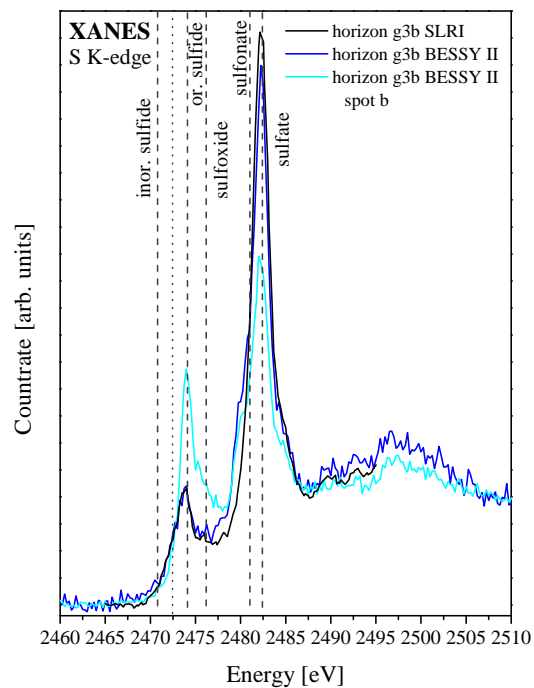


Figure 3.10.: Sulfur XANES spectra of soil horizons measured at BL8 at SLRI and at KMC-1 at BESSY II.

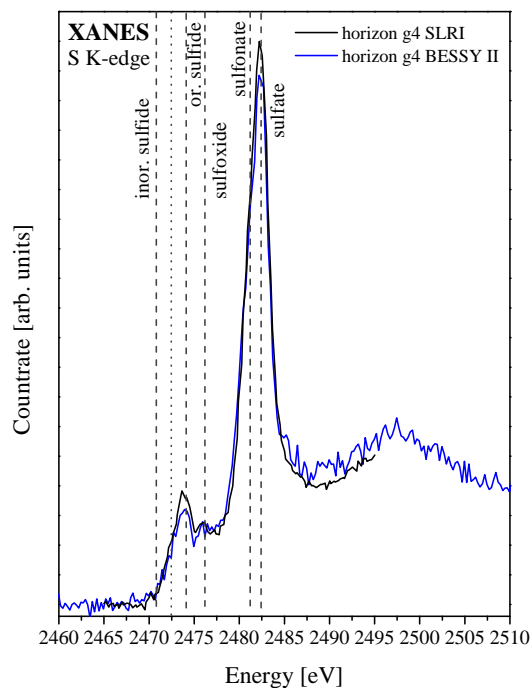
Figures 3.10(c) and 3.10(d) show very noisy spectra of two samples of the same horizon, due to the fact that this horizon has a very low concentration of sulfur of 0.01 weight – %. The consistency of SLRI and BESSY II data is nevertheless quite good, for horizon g3b a second normalization was not even necessary. Differences can be explained by inherent sample inhomogeneities. Such heterogeneities can be observed in figure 3.10(d), in which two spectra taken at BESSY II are shown, representing two different spots on the same sample. The difference in



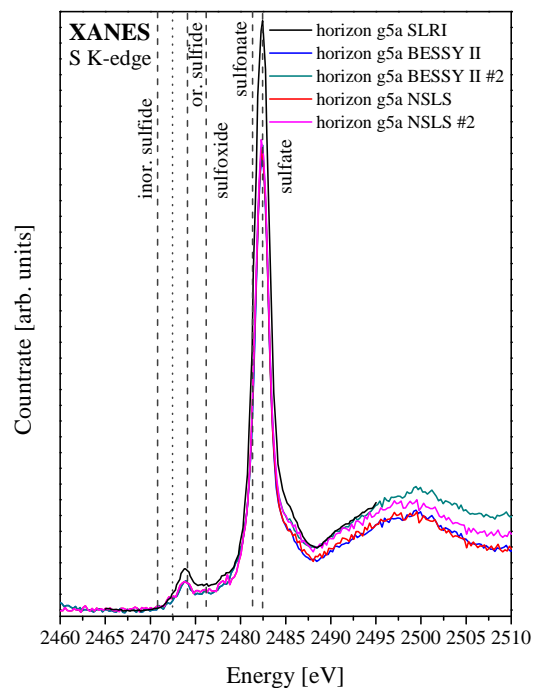
(c) Horizon g3a



(d) Horizon g3b



(e) Horizon g4



(f) Horizon g5a

Figure 3.10.: Sulfur XANES spectra of soil horizons taken at BL8 at SLRI, at KMC-1 at BESSY II and at X15B at NSLS.

sulfur speciation is considerable, one spot (spot b) showing a much stronger contribution from reduced sulfur species than the other, whereupon spot b seems not to be representative for the whole sample. A further discussion of sample respectively soil heterogeneities is given in section 3.5.

Spectra in figures 3.10(e) and 3.10(f) are dominated by sulfates. For figure 3.10(e), a second normalization was not possible because of bad signal to noise ratio within the BESSY II data, but it was not explicitly necessary. The datasets show good agreement. Horizon g5a, displayed in figure 3.10(f), was measured at all three beamlines. BESSY II and NSLS spectra are completely identical and both yield good agreement with SLRI data after a second normalization.

Summarizing, it can be stated that signal to noise ratio is always best in SLRI measurements, which is certainly due to the 13 element detector and dwell times of 10 s. Additionally, BL8 at SLRI gives the best average of each sample. Because of the large spot size it is least sensitive to sample heterogeneities. The performed normalization of SLRI data is fairly good. The errors induced by wrong normalization are not bigger than sample inhomogeneities. However, for spectra comprising high fractions of various oxidation states (e.g. figures 3.10(a) and 3.10(b)), higher oxidation states (sulfonates and sulfates) are more affected by normalization errors than lower oxidation states (sulfides and sulfoxides). The sulfonate and sulfate peaks become too low.

The consistency of data taken at the three different beamlines is best for medium concentrated samples, such as war debris and soil horizons with a sulfur concentration ranging from 0.04 weight – % in horizon g1 to ~ 1 weight – % in coals. Otherwise spectra are very sensitive to either self absorption induced by small variances in sulfur concentration or noise effects.

3.4. Reference samples

A variety of reference samples was measured for different purposes. They can be used as - somewhat extended - reference or standard spectra in linear combination fitting. Moreover, they provide an overview of the sulfur pool within the rubble dumps. Most reference samples are debris components or building rubble, respectively, found within the soil profiles at the Teufelsberg. These samples are listed and characterized in table 3.2. Debris components (dc) 1 to 7 were measured at SLRI, dc8 to dc23 were measured at BESSY II. Some coals were added to this lot, to account for more reduced sulfur species. They were also measured at SLRI. The samples were finely ground and applied to Kapton or carbon tape as described above. At SLRI, the spectra of debris components were measured twice with a dwell time of 10 s, at BESSY II three times with a dwell time of 1 s at two different positions on the sample. Coals were recorded twice with a dwell time of 1 s.

The debris components vary strongly in total sulfur concentration, by more than one order of magnitude between the highest and lowest concentration. Total sulfur concentration was determined during elemental analysis (CHNS analysis) by the working group of Prof. Dr. Wessolek.

The spectra of the reference samples are shown in figures 3.11(a) to 3.11(c). Vertical lines in the diagrams are identical to the description in section 3.3.2. The anthropogenic sulfur pool is clearly dominated by sulfates. Most measured debris components are solely comprised of sulfates or mainly sulfates and little sulfur species of lower oxidation states, i.e. sulfides and sulfoxides. But even similar materials vary significantly in sulfur speciation. Eleven clay bricks were measured, yielding pure sulfates (e.g. dc3) or sulfates and reduced sulfur species (e.g. dc1). Within the pure sulfates, there are some with clear CaSO_4 signature (e.g. dc12) and some without (e.g. dc10). CaSO_4 can be distinguished from other sulfates by its characteristic post-edge features: a shoulder at the high energy side of the white line and two shape resonances at higher energies, [26], [68], cp. figure 3.3. Just a few components, pyrolyzed material and coals are dominated by reduced sulfur species and contain little sulfates. In this context, pyrolyzed material means any organic material that was exposed to fire. This may be for example ashes from home side fireplaces, gutted roof trusses or coals.

sample no	component	total S [weight %]	sample no	component	total S [weight %]
dc1	clay brick		dc13	(light gray) finery	0.020
dc2	clay brick		dc14	ocher clay brick	0.097
dc3	clay brick		dc15	ocher clay brick	0.061
dc4	clay brick		dc16	ocher clay brick	0.051
dc5	gypsum, clay brick, finery		dc17	black crystalline material	0.285
dc6	coal		dc18	finery	0.210
dc7	finery		dc19	mortar	0.055
dc8	red clay brick	0.015	dc20	paving stone	0.128
dc9	red clay brick	0.021	dc21	pyrolized material	0.298
dc10	natural colored clay brick	0.068	dc22	asphalt on gravel	0.140
dc11	pyrolized (coalified) material	0.664	dc23	paving stone	0.159
dc12	ocher clay brick	0.073			

Table 3.2.: Summary of measured reference compounds.

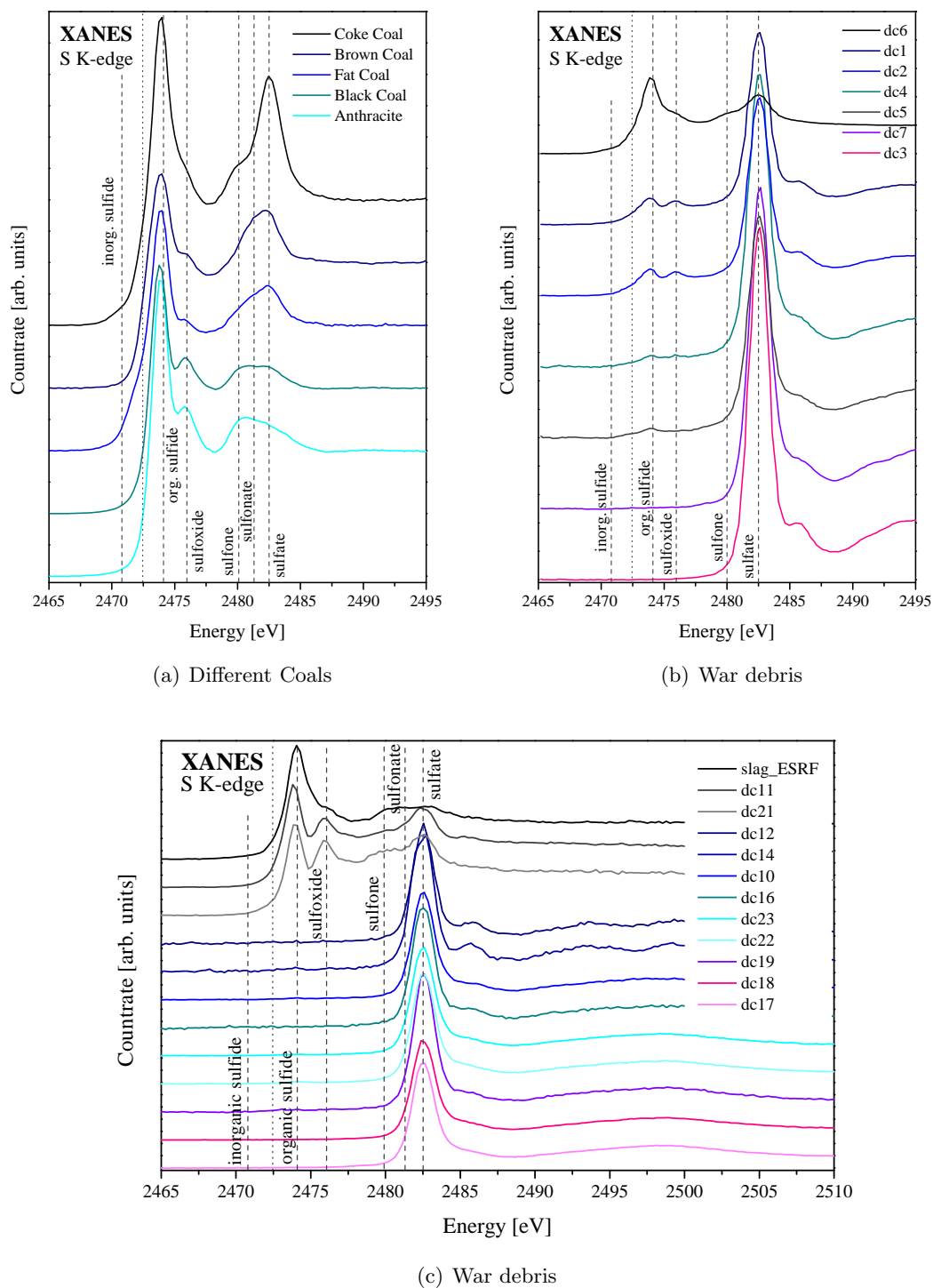


Figure 3.11.: Sulfur XANES spectra of reference samples: coals, war debris, building rubble; spectra taken at beamline KMC-1 at BESSY II and BL8 at SLRI.

3.5. Soil samples

Soil samples were taken at two sites, Teufelsberg and Schulgarten. Teufelsberg is the actual sampling site, samples from Schulgarten were mainly taken for evaluation of the sample preparation procedures. The sampling at both sites, the pedological analysis, as well as sample preparation outside of the synchrotrons (e.g. drying, sieving, grinding) was conducted by Dr. Beate Mekiffer from the working group of Prof. Dr. Wessolek.

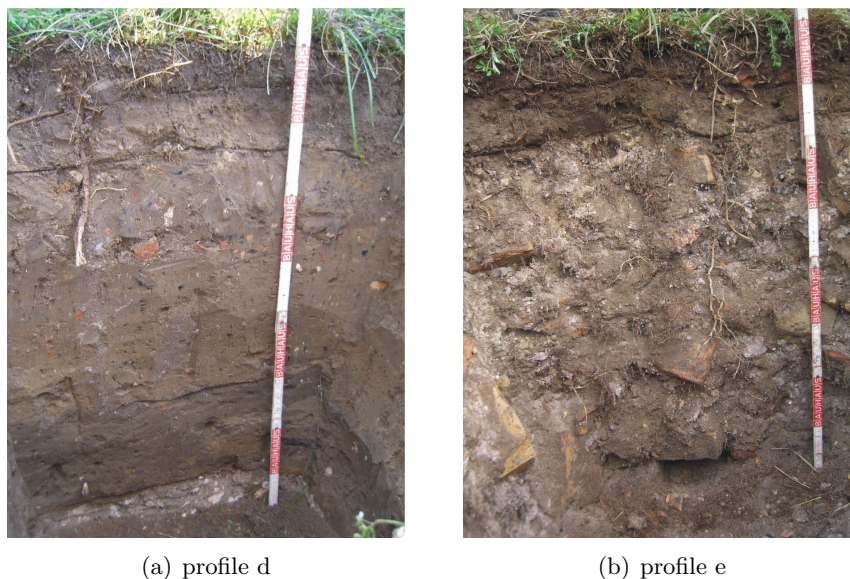


Figure 3.12.: Two of the six soil profiles laid out along the slope of the Teufelsberg, the biggest dump for building rubble from WWII in Berlin. Horizons in these soil profiles d and e are marked with lines, that were scratched into the soil with a shovel.

Samples from Teufelsberg were prepared in two ways, a main procedure and a second, slightly different procedure for comparison.

First, six different soil profiles (a to f) were laid out on the western side of the hill, which bears a slope of 10 %. The soil types are "Pararendzina from building rubble" and "Kolluvisol" in German taxonomy or "urbic Technosol (calcaric)" and "Anthrosol" in WRB (World Reference Base for Soil Resources) [9], [17]. They comprise mainly unweathered anthropogenic parent material, such as bricks, mortar, finery, slags, combined with quartz, few clay and technogenic organic material and, depending on the horizon, humus. The mean annual temperature of this site is 9.2°C and it receives a total annual precipitation of 578 mm. Nowadays this site is a recreational area with a vegetation of bushes and herbage. Profiles a to f run from top to bottom of the hill and are further characterized in table 3.3. The soils are well aerated and show minor microbial activity. Therefore, they do not provide reducing conditions. The horizons were marked as they were found in the field, see figure 3.12, and representative samples from each horizon were taken with a shovel. For the XANES measurements, the soil horizons were classified, dried, sieved, and subsequently the fraction of soil skeleton and total amount of sulfur (weight %) was determined. Determination of total sulfur concentration was conducted during

elemental analysis (CHNS analysis) by the working group of Prof. Dr. Wessolek. Then, the soil skeleton was milled to grain sizes below 2 mm and admixed in the original weight ratio to the fine earth fraction. This mixture was thereupon finish-ground. Using this sample preparation, the following measurements yield information on the overall sulfur pool present in the different soil profiles.

Later on, an additional soil profile (profile g) was laid out at the backslope of the Teufelsberg. Representative samples of each horizon were taken, dried and sieved. From two horizons different lots (buckets) were taken to look at the representativeness of the sampling. From this profile only the fine earth fraction was finely ground and used for XANES analysis. This preparation method only includes the most available sulfur pool within the whole horizon.

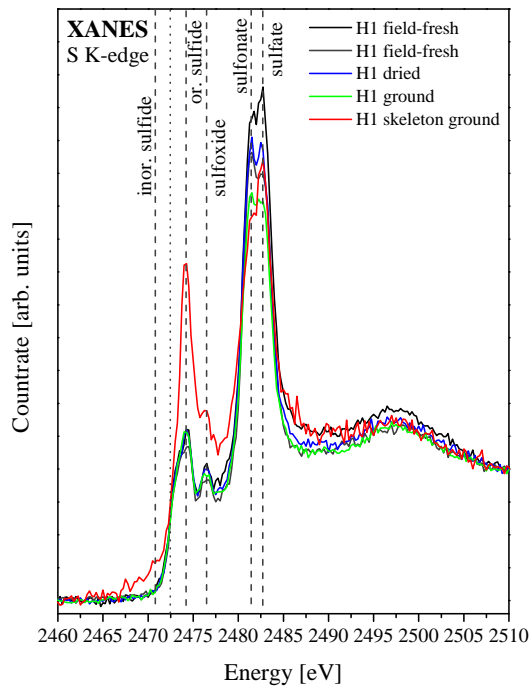
To ensure that these preparation procedures do not introduce additional sulfur into the samples nor alter the sulfur speciation, the procedures were examined on the basis of another, better available soil profile in the Schulgarten.

3.5.1. Schulgarten

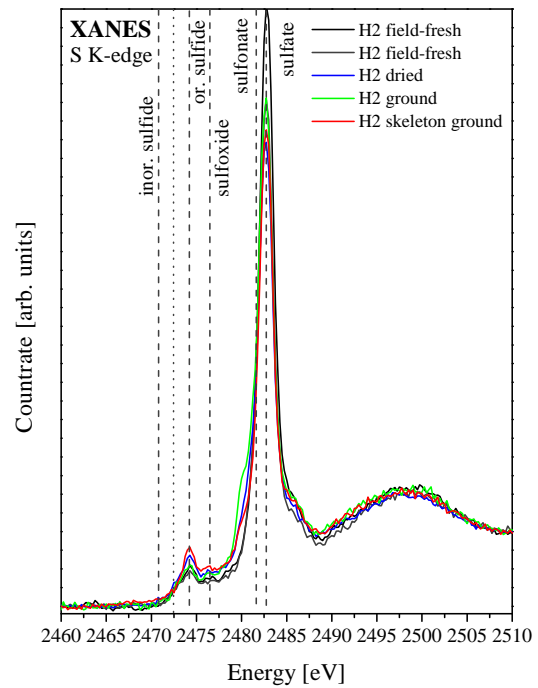
The Schulgarten profile consists of six horizons, horizon H1 to H6, named from top to bottom. Samples were taken as described above and afterward, samples of each preparation step were taken. First, so called field fresh, moist samples of each horizon were taken. Then the remaining portion was dried and sieved. Dried samples of the fine earth fraction as well as the soil skeleton, as far as there was a significant amount within the horizon, were taken. Last, the fine earth fraction and the soil skeleton were finely ground.

For XANES measurements, the field fresh samples of each horizon were packed in 4 μm thick ultralene membranes and sealed with Kapton tape. The dried samples were spread on carbon tape for measurements at BESSY II or on Kapton tape for measurements at NSLS. Spectra at KMC-1 at BESSY II were taken with a step size of 0.25 eV and a dwell time of 1 s. Spectra at X15B at NSLS were taken with a step size of 0.25 eV and a dwell time of 5 s. At both beamlines several spectra were taken at at least two different positions on the sample, depending on signal to noise ratio. Figures 3.13(a) to 3.13(e) show the influence of drying and grinding for each horizon. All spectra for one horizon are plotted on top of each other, to accentuate the differences in the spectra of the sample preparation steps. Vertical lines in the diagrams are to be interpreted in the same way described at the beginning of this chapter. The overall amount of sulfur within horizons 4 and 6 was too low to obtain evaluable measurements.

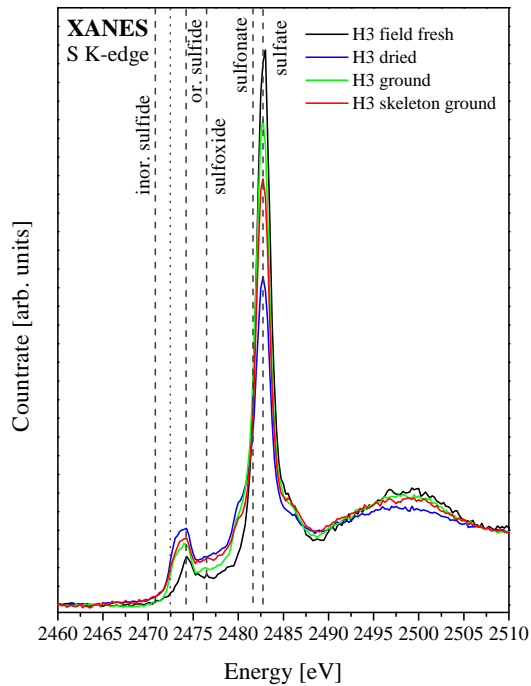
Horizon H1 (fig. 3.13(a)), an Ah horizon, was measured completely at KMC-1, but a field fresh sample was also measured at X15B. Except for the spectrum of finely ground soil skeleton, all spectra are identical. The small differences, mainly pronounced in the sulfonate and sulfate peaks, are on the one hand due to inherent sample, that is soil inhomogeneities. Different fractions of the horizon were measured for each preparation step. On the other hand, the grain sizes in each spectrum differ significantly depending on the sample preparation step: the field fresh and dried samples are not finely ground and therefore bear very different grain sizes and inhomogeneous sample thickness. This is especially true for the moist samples, which are packed in membranes. Varying sample thickness can yield varying sulfur concentration and higher oxidation states (sulfonates and sulfates) are more sensitive to small variations in concentration, as can exemplarily be seen in figure 3.4.



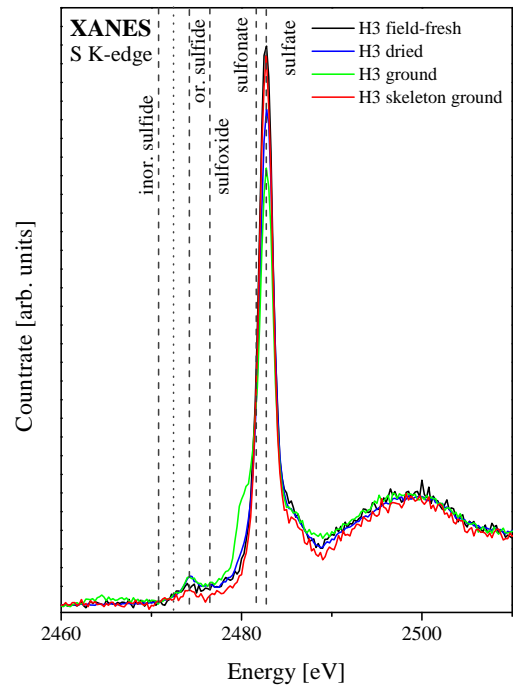
(a) horizon H1 (Ah horizon), measured at BESSY II KMC-1, second field-fresh spectrum measured at NSLS, X15B



(b) horizon H2 (yC horizon), measured at BESSY II KMC-1, second field-fresh spectrum measured at NSLS, X15B

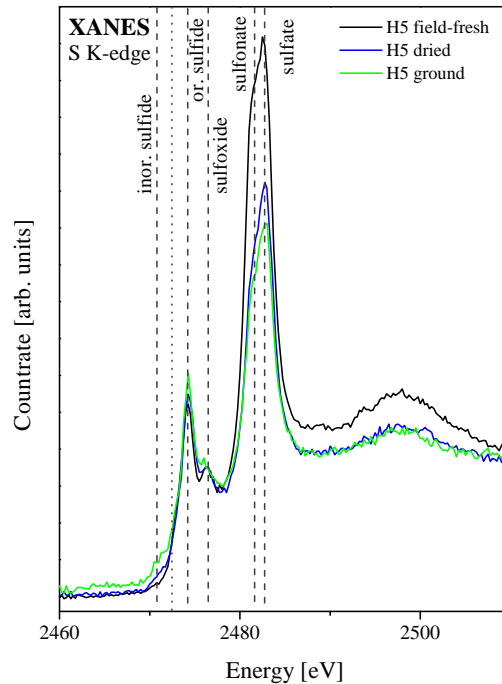


(c) horizon H3 (yC horizon), measured at BESSY II KMC-1



(d) horizon H3 (yC horizon), measured at NSLS, X15B

Figure 3.13.: Sulfur XANES spectra of sample preparation steps, samples taken from Schulgarten, Berlin.



(e) horizon H5 (yC horizon), measured at NSLS, X15B

Figure 3.13.: Sulfur XANES spectra of sample preparation steps, samples taken from Schulgarten, Berlin.

The deviating spectrum of the finely ground soil skeleton can also be explained by inherent inhomogeneities. Just a very small amount of substance is needed for measurements, and therefore only a few grains of the skeleton are used. It may easily happen, that the choice is not representative for the whole horizon. Apparently, some pyrolyzed material was caught in this case.

Horizon H2 (fig. 3.13(b)), a yC horizon, was measured completely at KMC-1 and a field fresh sample was also measured at X15B. All spectra are identical. The slight differences are caused by sample inhomogeneities, as described for horizon H1.

Horizon H3 (fig. 3.13(c) and 3.13(d)), a yC horizon, was measured entirely at KMC-1 and at X15B. Horizon H5 (fig. 3.13(e)), a yC horizon, was measured completely at X15B. This horizon does not comprise a significant amount of soil skeleton, as it consists mainly of quartz sand. However, the results with respect to sample preparation steps from horizons H3 and H5 are the same as for horizon H2.

In many of the BESSY II spectra of sulfate dominated dried and fine ground samples, as well as in the H3 ground spectrum measured at NSLS, a similar shoulder at the low energy side of the sulfate white line, as already observed in BESSY II data of Schwertmannite and Aluminum sulfate, can be observed. The energy position of this shoulder is about 2480 eV, which would correspond to sulfone species. However, a reduction of sulfate to sulfone caused by beam damage is not likely, as this shoulder is already observed in the first spectrum taken and does not grow

with longer exposition to the beam. Furthermore, it occurs mainly in BESSY II data (never in SLRI data), the only beamline where the sample is electrically contacted. Therefore, produced free electrons will rather be discharged than reduce sulfate. A reduction by sample preparation is also unlikely as those processes would rather lead to oxidation (and the shoulder would be observable in all spectra). Figueiredo et al. [15] reported on the effect of oxygen sharing on the white line of sulfate minerals. They observed similar shoulders if the sulfate minerals were not fully hydrated, due to changes in the crystal structure. Possibly, the energy input by the x-ray beam in combination with high vacuum conditions at BESSY II can cause a dehydration of the sulfate minerals.

3.5.2. Teufelsberg

Figures 3.14(a) to 3.14(f) display the sulfur XANES spectra of all horizons within the six different soil profiles a to f, laid out during the first sampling operation. Each of the six diagrams comprises the spectra of all horizons of one profile, displayed from top to bottom as they were found in the field. Only the last spectrum in profile b does not represent a full horizon but a nugget, comprising a certain amount of pyrolyzed material, that was found within the last horizon. The total amount of sulfur within the samples varies from 100 to 2500 ppm, causing differences in the quality of the fluorescence spectra. Basically, the spectra of the least concentrated soil horizons, horizon b2 and f3 to f5, are affected, showing pronounced noise. All spectra are measured twice at SLRI with a dwell time of 10 s or 20 s, depending on signal to noise ratio. Vertical lines in the spectra indicate different sulfur species, as described previously.

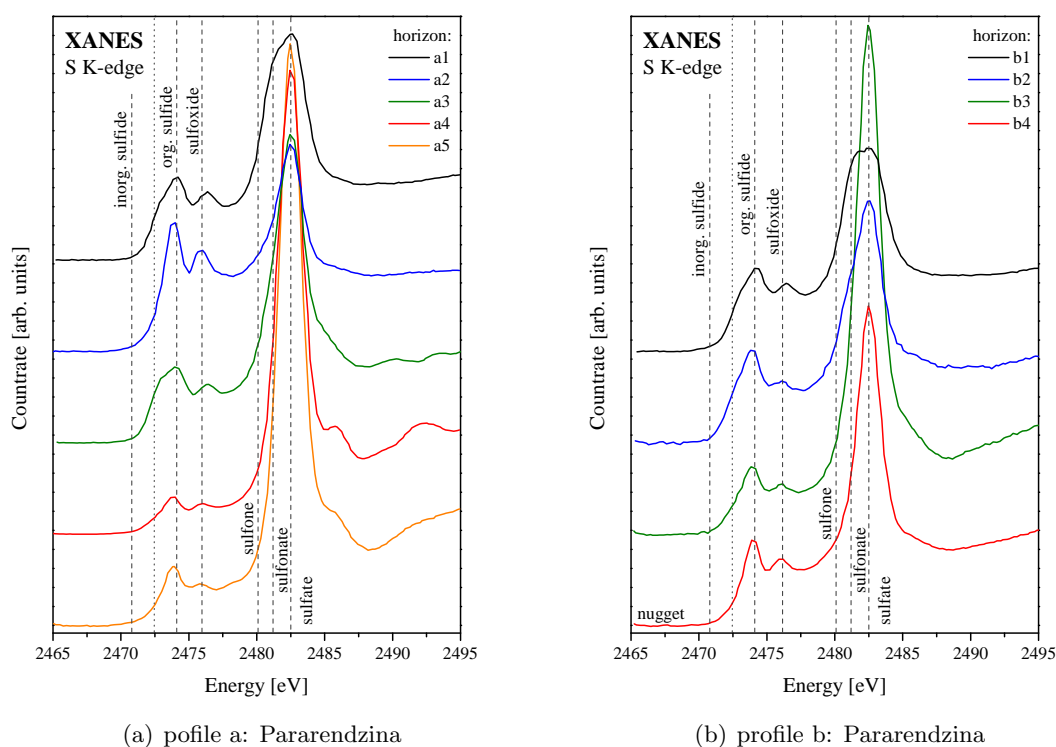
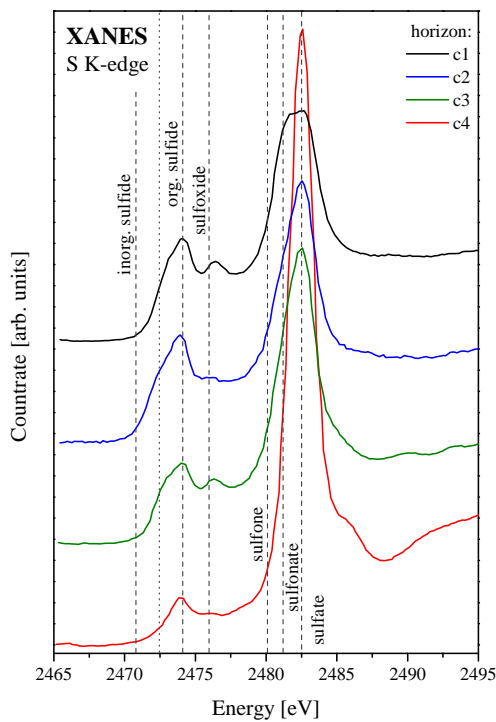
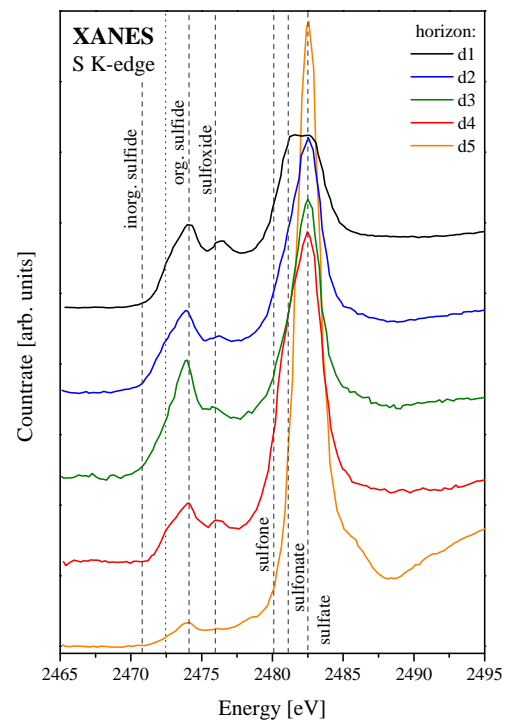


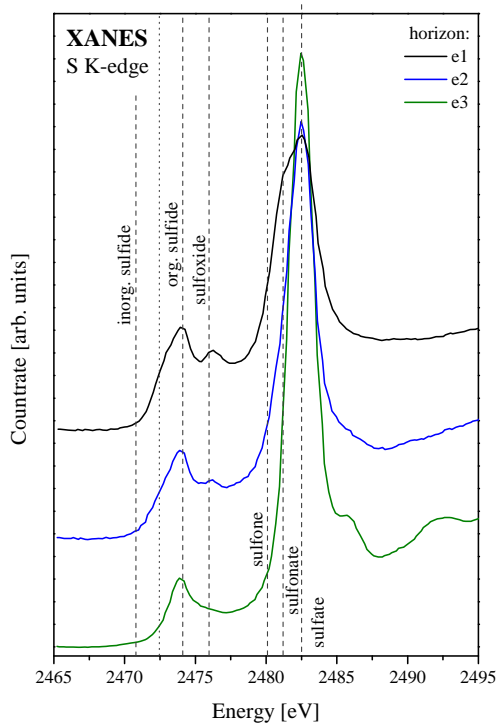
Figure 3.14.: Sulfur XANES spectra of soil profiles a - b of the Teufelsberg, horizons displayed from top to bottom as found in the field; spectra taken at BL8 at SLRI.



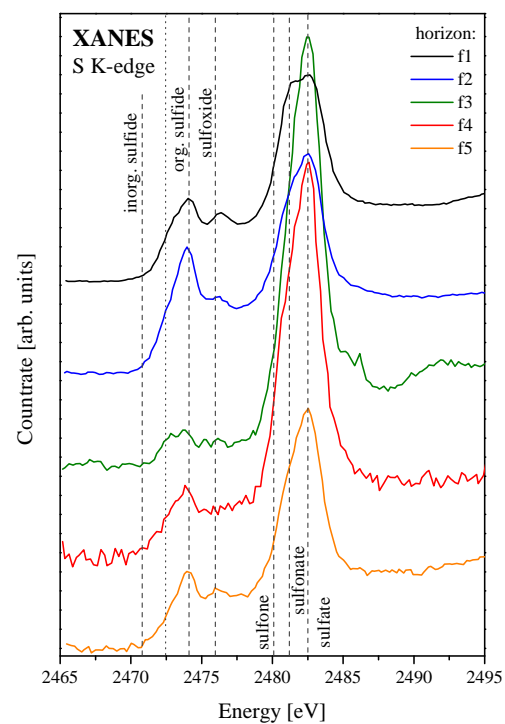
(c) profile c: Pararendzina



(d) profile d: Kolluvisol above Pararendzina



(e) profile e: Pararendzina



(f) profile f: Kolluvisol

Figure 3.14.: Sulfur XANES spectra of soil profiles c - f of the Teufelsberg, horizons displayed from top to bottom as found in the field; spectra taken at BL8 at SLRI.

Name	Soil Type	Depth [cm]	Horizon	Root penetration	pH	Humus	Total S [weight %]	Total C	Total N	Debris components
Profile a, Pararendzina										
a1	mS	0 - 10	Ah	strong	5.5	1.5 - 3	0.06	3.3	0.26	gravel, finery, clay brick, slag
a2	mSgs	10 - 24	jC ₁	medium	6.0	0.6 - 0.9	0.11	2.8	0.06	gravel, finery, clay brick, chamotte
a3	mSgs	24 - 31	yC ₂	medium	6.0	1.5 - 3	0.10	2.9	0.20	finery, clay brick, slag
a4	mSfs	31 - 58	yC ₃	low	5.5	1.5 - 3	0.16	3.0	0.15	finery, clay brick, slag
a5	mSgs	58 - 81	yC ₄	-	7.0	0.6 - 0.9	0.06	1.8	0.03	finery, clay brick, slag
Profile b, Pararendzina										
b1	mSfs	0 - 9	Ah	strong	5.3	1.5 - 3	0.05	2.6	0.22	gravel, finery
b2	mSgs	9 - 36	jC ₁	medium	6.0	0.6 - 0.9	0.01	0.8	0.04	gravel, finery, clay brick, slag
b3	mSfs	36 - 74	yC ₂	low	6.0	1.5 - 3	0.06	1.8	0.06	finery, clay brick, slag
b4	-	42 - 51	(nugget)		6.0	0.3 - 0.6	0.08	1.1	0.03	gravel, finery, slag
Profile c, Pararendzina										
c1	mS	0 - 10	Ah	strong	5.5	1.5 - 3	0.06	2.6	0.22	gravel, clay brick, slag
c2	mSgs	10 - 25	jC ₁	strong	5.5	1.5 - 3	0.03	1.0	0.04	gravel, finery, slag
c3	mSfs	25 - 30	jC ₂	medium	5.5	1.5 - 3	0.08	2.5	0.18	gravel, finery, clay brick
c4	mSgs	30 - 81	yC ₃	-	7.0	0.6 - 0.9	0.09	2.0	0.04	finery, clay brick, slag
Profile d, Kolluvisol above Pararendzina										
d1	mSfs	0 - 5	Ah	strong	5.5	1.5 - 3	0.04	2.8	0.52	gravel, finery, clay brick
d2	mS	5 - 13	M ₁	strong	6.5	0.6 - 0.9	0.03	1.3	0.06	gravel, finery, clay brick
d3	mSgs	13 - 52	M ₂	low	7.0	0.6 - 3	0.02	0.4	0.01	finery, clay brick
d4	mSfs	52 - 70	M ₃	-	7.0	1.5 - 3	0.02	1.4	0.06	gravel, finery, slag
d5	mSfs+gs	70 - 77	IIyC ₁	-	7.5	0.6 - 0.9	0.06	1.7	0.02	finery, clay brick, slag

Name	Soil Type	Depth [cm]	Horizon	Root penetration	pH	Humus	Total S [weight %]	Total C	Total N	Debris components
Profile e, Pararendzina										
e1	mSfs	0 - 6	Ah	strong	5.5	1.5 - 3	0.06	2.8	0.21	gravel, finery, clay brick
e2	mS	6 - 16	jC ₁	medium	6.0	1.5 - 3	0.04	2.0	0.07	gravel, finery, clay brick
e3	mSgs	16 - 82	yC ₂	-	7.0	0	0.25	4.2	0.05	finery, clay brick, slag
Profile f, Kolluvisol										
f1	mSfs+gs	0 - 7	Ah	strong	5.5	1.5 - 3	0.05	2.2	0.18	gravel, clay brick, slag
f2	mSfs+gs	7 - 23	M ₁	medium	6.0	0.6 - 0.9	0.03	1.1	0.06	gravel, gypsum
f3	mSgs	23 - 57	M ₂	-	5.5	0.3 - 0.6	0.01	0.2	0.01	gravel, finery
f4	mS	57 - 64	M ₃	-	5.5	0.3 - 0.6	0.01	0.4	1.26	gravel, finery
f5	mS	64 - 80	M ₄	-	6.0	0	0.01	0.5	0.02	finery, tarboard
Profile g, backslope										
g1		0 - 10					0.04	2.1	0.17	
g2		10 - 25					0.04	1.5	0.14	
g3a		25 - 75					0.01	0.8	0.03	
g3b		25 - 75					0.01	0.8	0.03	
g4		70 - 90					0.01	0.8	0.34	
g5a		90 - 120					0.05	2.0	0.36	
g5b		90 - 120					0.05	2.0	0.36	
g5c		90 - 120					0.06	2.0	0.36	
g5d		90 - 120					0.05	2.0	0.36	

Table 3.3.: Short characterization of the investigated soil samples.

Obviously, the sulfide content within all profiles diminishes from top to bottom, while the sulfate content rises. Sulfoxide and sulfonate seem to vanish. This can be expected, because the humus fraction and therefore the fraction of organic material diminish from top to bottom. Slight exceptions are profile d, a Kolluvisol above Pararendzina, and profile f, a Kolluvisol. As described in chapter 1, a Kolluvisol is typical on hillside toes, developing from erosion of higher terrain, and is characterized by transferred humous soil fractions within all horizons. This can also easily be read in the spectra, by means of not diminishing sulfide and sulfonate peaks, especially in figure 3.14(f). In figure 3.14(d), the rise in sulfonate fraction in horizon d4 indicates the transition from Kolluvisol to Pararendzina (which should obviously start with an Ah horizon).

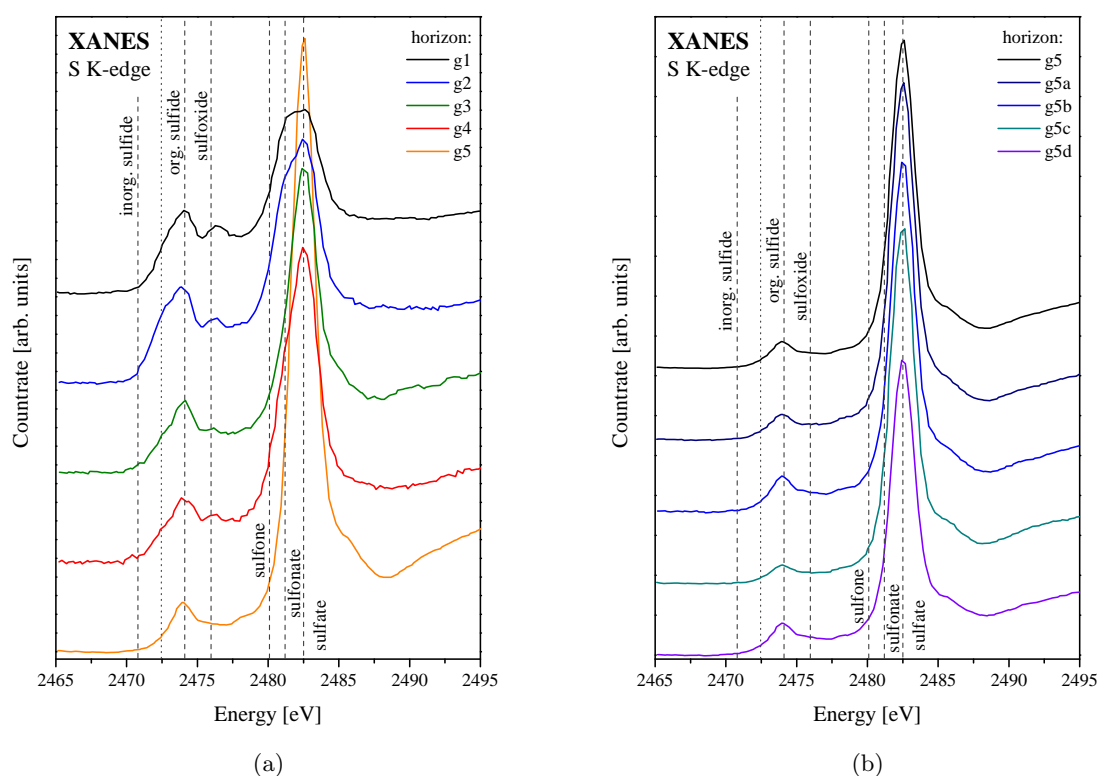


Figure 3.15.: Sulfur XANES spectra of soil profile g of the Teufelsberg, horizons displayed from top to bottom as found in the field; four different samplings of horizon g5 and average; spectra taken at BL8 at SLRI.

Differences in sulfate speciation can also be seen in the spectra: horizons a4 and e3 show the signature of pure CaSO_4 , while other spectra also dominated by sulfates, as horizons a5 or d5, show a minor CaSO_4 fraction. In these horizons, also fractions of Na_2SO_4 , MgSO_4 , FeSO_4 or $\text{Al}_2(\text{SO}_4)_3$ are most certainly present. Nevertheless, a fraction of CaSO_4 is usually identifiable.

Figures 3.15 show the spectra of profile g, laid out during the second sampling operation on the backslope of the Teufelsberg, as described in section 3.5. Figure 3.15(a) comprises the spectra of each horizon, displayed from top to bottom as found in the field. Thereby, horizon g3 represents

the average of two samples (two buckets taken during sampling) and horizon g5 represents the average of four samples taken from the same horizon. For horizon g5, all four samples and the average are shown in figure 3.15(b), demonstrating good representativeness of the sampling, as the spectra g5a to g5d show only minor variances.

Profile g was laid out close to profile d and the substantial similarity is obvious. Section 3.5.1 already showed that the soil skeleton normally shows the same sulfur speciation as the fine earth fraction.

3.5.3. Peak fitting

Peakfits were performed on each spectrum using the software ATHENA [49]. An example is given in figure 3.16. Gaussian and Lorentzian lineshapes as well as several mixtures of both were tried on all spectra measured at SLRI: the soil horizons as well as standards and debris components. It turned out that pure Gaussian lineshapes are best suited to fit the spectra. Therefore, several Gaussian shaped peaks were fitted into the spectra, each representing a white line of the different occurring sulfur oxidation states. Two arctangent functions were chosen to represent the edge steps, one for the reduced and one for the oxidized sulfur species. As already mentioned in section 2.3, each sulfur species should principally have its own arctangent function, but this approach (only two arctangents each as a sum of several contributions) does not significantly influence the fitting results but yields fits that are much more stable. The different sulfur species can then be identified by comparison of the peak positions with the white line energies of standard spectra, either taken within the framework of this work or from literature. The following assignment according to Vairavamurthy [72] was chosen (table 3.4). It was converted to an energy calibration that sets the sulfate white line peak to 2482.5 eV.

sulfur species	energy range [eV]
inorganic sulfide	2469.8 - 2472.4
organic sulfide	2472.5 - 2475.0
sulfoxide	2476.1 ± 0.3
sulfone	2479.7 ± 0.4
sulfonate	2481.0 ± 0.3
sulfate	2482.5 ± 0.3

Table 3.4.: Peak assignment for the occurring sulfur species by means of white line energy.

FWHM was only loosely constrained during the fits and varies between 0.6 and 0.9 eV. For the post-edge feature, even wider FWHMs were allowed. In the sulfide energy range, two peaks were fitted, to account for the wide energy range and the variety of possibly contributing sulfide moieties.

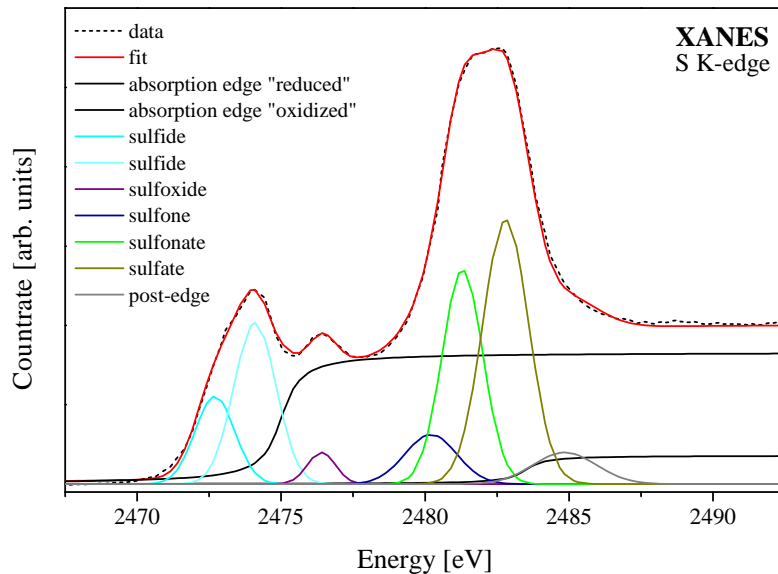


Figure 3.16.: Exemplary fit. Several Gaussians represent the white line of the different occurring sulfur species, one Gaussian accounts for post-edge features. Two Gaussians were used in the sulfide energy range to account for the different contributing sulfide moieties. Two arctangent functions each represent a sum of several single absorption steps. The low-energy one accounts for the two sulfide steps, while the second represents the sum of all steps belonging to oxidized sulfur species (sulfoxide to sulfate).

The proportion of each occurring sulfur species in each spectrum respectively horizon is then calculated by comparing the respective peak area with the sum of all peak areas within this spectrum. Peaks at energies above 2483 eV are not taken into account, because these are post-edge features. As the absorption cross section linearly increases with the sulfur oxidation state, the fitted peak areas need to be corrected by scaling factors, as described in section 2.3. It was chosen to utilize the generic curve proposed by Manceau et al. [37]. The results of this analysis are shown in figures 3.17(a) to 3.17(f), giving the proportion of the contributing sulfur species of each horizon in each soil profile (they always sum up to 100 %). Each line of horizontal bars represents the composition of one horizon, arranged analogically to the spectra in figures 3.14(a) to 3.14(f).

From these plots it is evident, that the sulfate content rises from top to bottom within each soil profile, while the sulfide content declines. Exceptions are the nugget b4 in profile b and the Kolluvisol profile f. Several horizons possibly comprise inorganic sulfides, having peak energies of the lower sulfide peak between 2472.3 and 2472.6 eV (the border being 2472.5 eV). However, inorganic sulfides are not evident, as energy calibration of the spectra as well as peak positions within the fits each comprise an error of roughly 0.1 eV. Furthermore, those horizons possibly containing inorganic sulfides do not yield a meaningful pattern. Sulfoxide is more or less equally distributed throughout all horizons, slightly diminishing from top to bottom, but its fraction is relatively small. For some of the deepest horizons (in profiles c, d, e) and the very noisy spectra of the Kolluvisol in profile f, sulfoxide is missing completely. Sulfone is equally distributed throughout all horizons, but its fraction is also quite low. The distributions of both, sulfoxide

and sulfone do not give a meaningful pattern. Furthermore, sulfone is not typically abundant in soil organic matter. This fact together with small amounts of this species may indicate that it is not really abundant in the samples but results from fitting errors (post-edge features of species with lower oxidation state or features arising from interactions of manifold sulfur species and moieties, generally common in multi component analysis). For sulfoxide, the same may be true, although e.g. methionine sulfoxide, a result of the oxidation of sulfur in methionine, occurs in body tissues. In living cells, it is continuously reduced to methionine. Therefore, methionine sulfoxide may be abundant in decaying organisms and therefore in humus. Sulfonate vanishes in the deepest horizons of all profiles except for profile f, and is correlated to the humus content and root penetration. It is evenly abundant in all Kolluvisol horizons, as Kolluvisol by definition is enriched in humus. Sulfonate is also abundant in all upper horizons and diminishes with humus content and root penetration from top to bottom. In profile d, its rise in horizon d4 possibly indicates the transition from Kolluvisol to Pararendzina, as Pararendzina should start with an horizon rich of humus, an Ah topsoil. This horizon is followed by the typical spectrum of a lower C horizon d5.

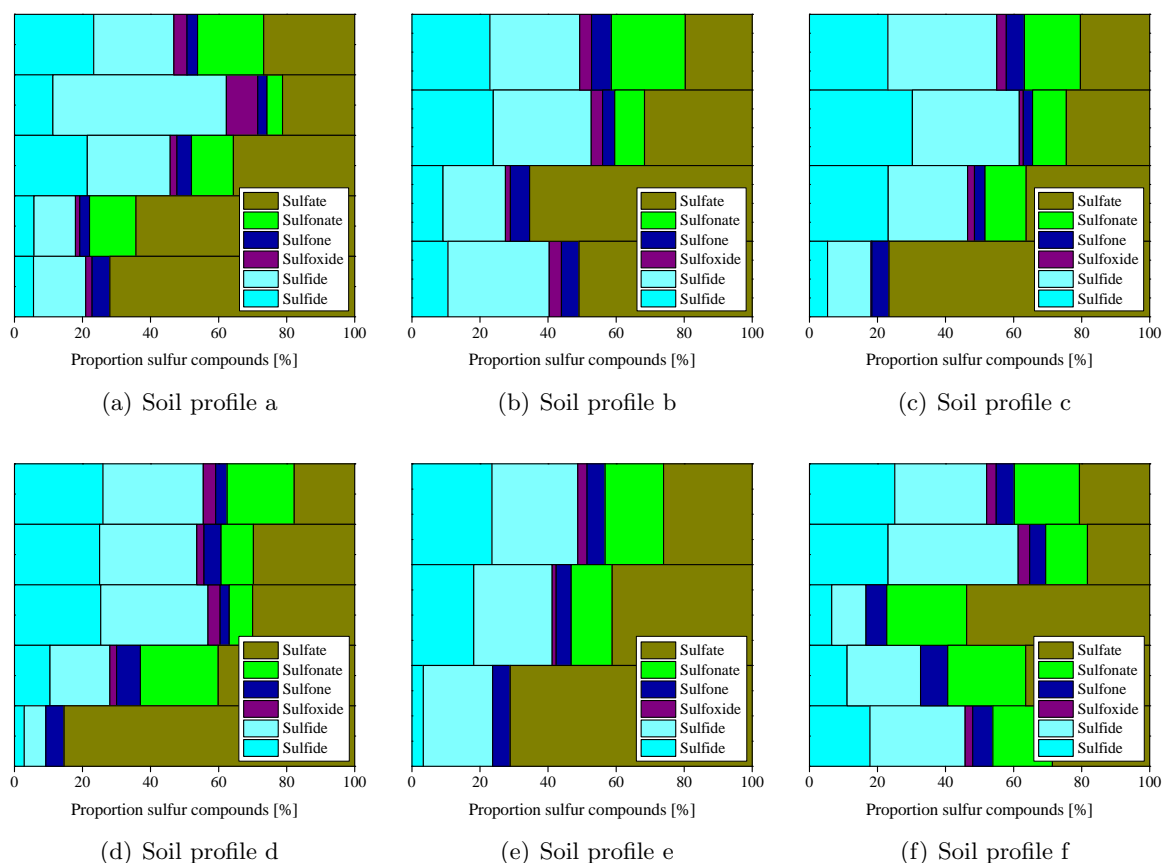


Figure 3.17.: Proportions of sulfur species within each horizon of the soil profiles. Diagrams a to f correspond to soil profiles a to f (table 3.3) and therefore to the spectra in figures 3.14(a) to 3.14(f). Each horizontal bar diagram within diagrams a to f represents the proportions of sulfur species of one horizon displayed from top to bottom as they were found in the field (in analogy to figure 3.14)

3.5.4. PCA

The software SIXPACK [77] was used to do the principal component analysis. As described in section 2.3, a dataset for PCA should fulfill several conditions: sufficient number of single spectra, "adequate" signal-to-noise ratio of each spectrum, consistent energy range and all spectra need to be normalized. Therefore, two separate datasets were chosen: spectra of all Teufelsberg horizons measured at SLRI and spectra of those Teufelsberg horizons measured at BESSY II plus debris components measured at BESSY II.

In principal component analysis, from the matrix of all measured spectra, a set of eigenvectors and corresponding eigenvalues is calculated, aiming to find an orthonormal basis. Obviously, the set of basis vectors should be much smaller than the number of measured spectra (however, the number of spectra are the maximum number of basis vectors), as the spectra are certainly not all linearly independent. Eigenvalues equal to zero obviously imply that the respective eigenvector is not part of the orthonormal basis. Uncertainties arise from noise in the spectra. Small eigenvalues indicate that the respective eigenvector is originating from noise and should therefore also be eliminated from the basis set. The difficulty is then to decide which eigenvector (with a rather small eigenvalue) only represents noise in the data and which represents a small but still significant feature in the spectra. This can be identified best by trying to reconstruct all measured spectra with a different number of eigenvectors. The minimal number of eigenvectors required to reconstruct all spectra are the principal components.

3.5.4.1. SLRI dataset

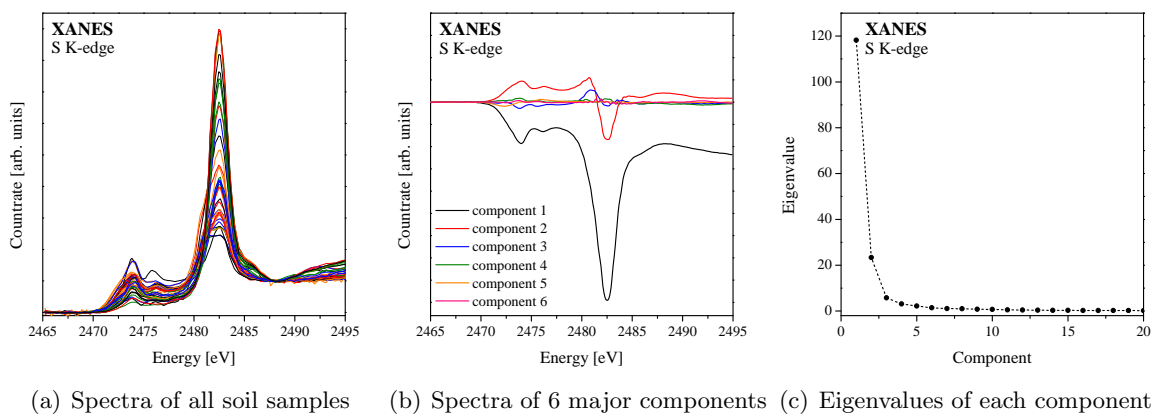


Figure 3.18.: Summary of PCA for all soil samples.

Figures 3.18 to 3.23 represent the principal component analysis performed on the first dataset, the spectra of all Teufelsberg horizons measured at SLRI. The very noisy spectra of horizons f3 to f5 were excluded from the analysis. Spectra were normalized as well as possible as described in section 3.3. Figure 3.18 shows the whole dataset of all measured soil spectra, as well as the spectra of the first six components, (the principal components) and a plot of the eigenvalues of each component. From these diagrams it is not obvious, why the first six components were

chosen to be the principal components of the soils, as only the eigenvalues of the first two components are significantly larger than the rest.

This becomes clear when considering reconstruction of the measured spectra. With all principal components it must be possible to reconstruct each of the measured spectra except for some noise in the data. Figures 3.19 to 3.23 show the reconstruction of measured spectra from different horizon samples with a different number of components. In each plot (a) only the first two components are used for reconstruction, in plots (b) the first four and in plots (c) the first six components are used. Five representative horizons are chosen to clarify the choice of the principal components.

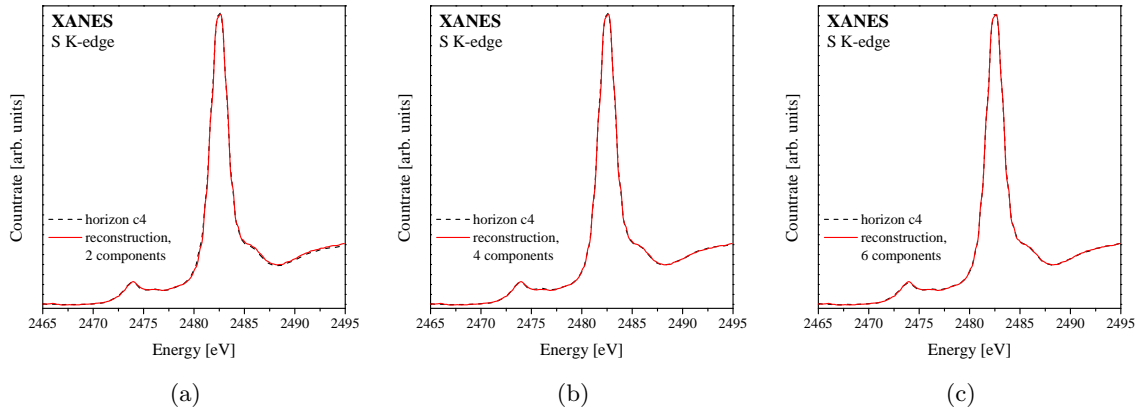


Figure 3.19.: Reconstruction of horizon c4 with different number of components.

For horizon c4 (figure 3.19), a perfect fit is already reached with the first two components. It only improves minimally with four components and does not change anymore when switching from four to six components.

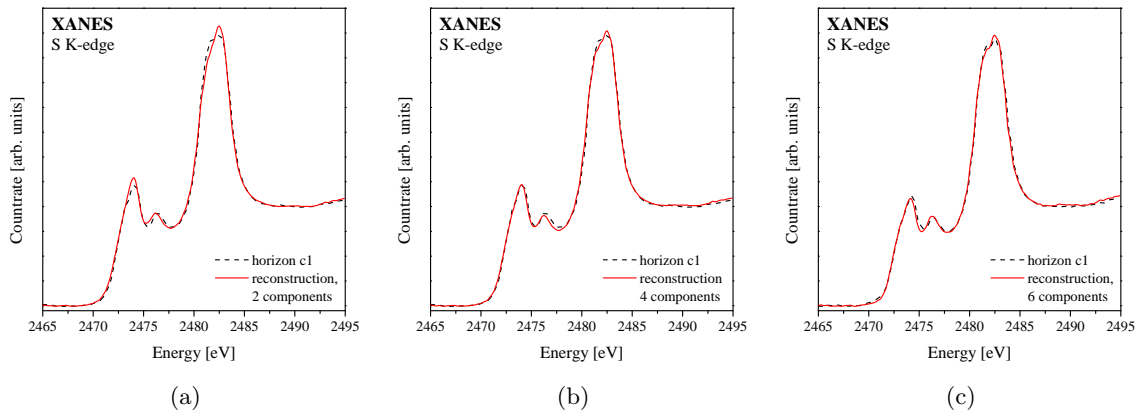


Figure 3.20.: Reconstruction of horizon c1 with different number of components.

However, the fitting results are completely different for other horizons. For horizon c1 (figure 3.20), the fit using only the first two components is already quite good, but some discrepancies can be observed in the energy ranges and respective peaks of sulfide, sulfoxide and sulfonate. When using four components, the fit improves significantly at the sulfide and sulfonate peaks and gets almost perfect with six components.

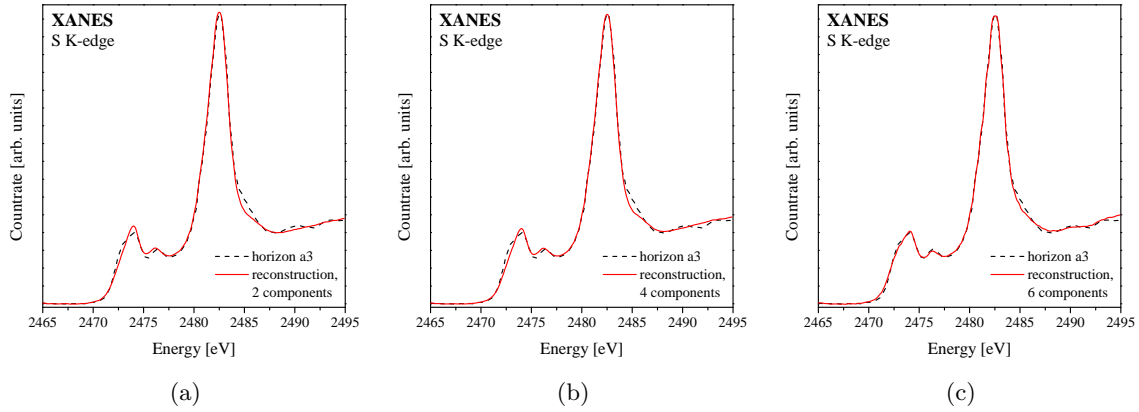


Figure 3.21.: Reconstruction of horizon a3 with different number of components.

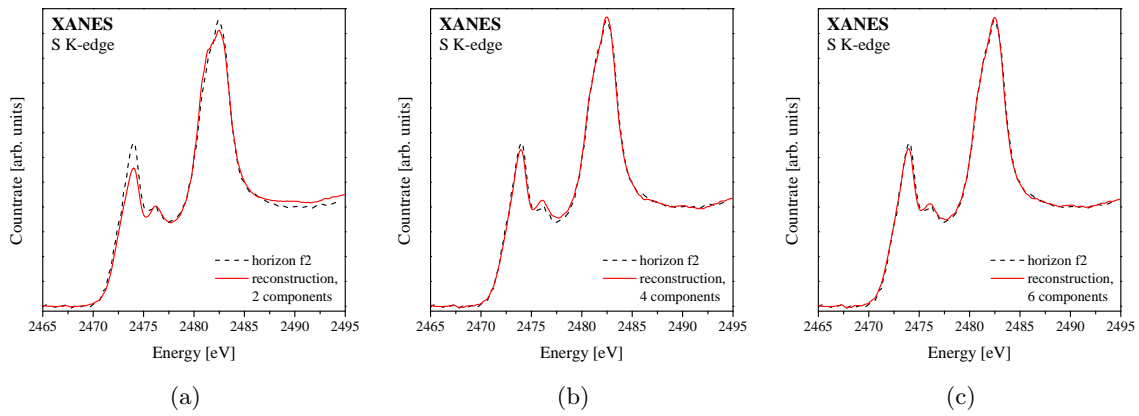


Figure 3.22.: Reconstruction of horizon f2 with different number of components.

For horizon a3 (figure 3.21), the first fit with two components is slightly worse than the fit for horizon c1, revealing discrepancies in the energy ranges of sulfide and sulfoxide and in the post-edge region. A fit with four components does not yield any improvements, only with six components the fit becomes good.

For horizon f2 (figure 3.22), the first fit using two components is much worse than the ones conducted for the other horizons, with large errors in the sulfide, sulfate and post-edge regions and a minor error in the sulfonate region. A reconstruction with four components is already very good, yielding only slight discrepancies in the sulfide and sulfoxide regions and a reconstruction with six components is perfect.

For horizon a2 (figure 3.23), a reconstruction using only the first two components is quite bad with large errors in all energy ranges. The fit improves significantly using four components, with some discrepancies in the sulfide and sulfoxide region. Especially a feature of a very reduced sulfur species seems to be missing, which can, to a much lesser extent, already be observed in horizon a3. With six components, this fit also becomes perfect.

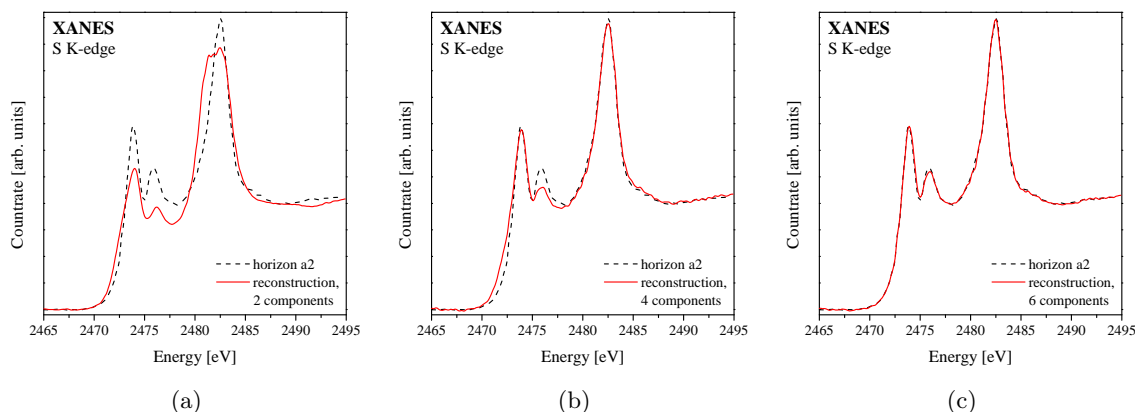


Figure 3.23.: Reconstruction of horizon a2 with different number of components.

It can be concluded that the real number of principal components in this dataset is six. By using six components for reconstruction, all significant variances in all horizons can be reproduced. This is also in good agreement with the results obtained from the peak fitting analysis, where a maximum of six Gaussians at different energies, corresponding to six different sulfur oxidation states could be fitted to the data.

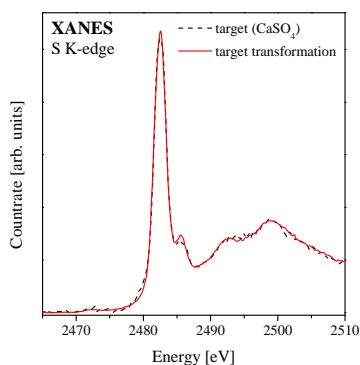


Figure 3.24.: Exemplary target transformation of CaSO_4 (with BESSY II dataset), chi-square = 1.

Using target transformation, it can be tried to find those spectra, that really represent the measured data, as a linear combination. Target transformation can be applied on all measured standard spectra, to find those that represent the data best. These are different sulfur oxidation states, different species of the same oxidation state and also different concentrations. Those candidates yielding the best results can then be used in linear combination analysis. Essentially, target transformation is identical to the reconstruction of sample spectra with the obtained eigenvectors discussed above. In target transformation, standard spectra are tried to construct with the previously obtained principal components. If the construction of the chosen standard with the principal components yields a good fit, the standard is likely to be comprised in the samples. To put it more mathematically: It is determined whether a chosen standard spectrum can be expressed in the same mathematical space as is defined by

the principal components, c.p. section 2.3.

All considered spectra are listed in the Appendix in table A.1. The spectra are either own

measurements or taken from ESRF database. For own data, the concentration of the specific sulfur compound in weight-% (in relation to sand used for dilution) is given. The spectra are normalized as described in section 2.1 and calibrated in energy on the basis of the CaSO_4 white line at 2482.5 eV. For ESRF data, the sulfur concentration is not given in the database. As the spectra are calibrated differently (different experimenters used different systems), the spectra are recalibrated in energy on the basis of the CaSO_4 white line at 2482.5 eV. ESRF data was also normalized. Especially spectra of organic sulfur compounds and several mineral sulfides were taken from ESRF database, to complete the set of standards accessible to target transformation and linear combination fitting. Primarily, compounds typically abundant in soils were chosen, but then the dataset was expanded to compounds possibly abundant in debris, such as heavy metal sulfides or compounds occurring in decarbonized material (e.g. coals, charcoal). The result of target transformation respectively goodness of fit for each compound is judged by means of chi-square values [77], [36]. An example is given in figure 3.24. Good results are obtained for most sulfates, yielding chi-square values up to 14, but mostly in the range of 1 to 7. For CaSO_4 , several concentrations were tried, yielding the best result for the lowest concentration and getting worse with rising concentration. Moreover, CaSO_4 gives the best result of all considered compounds. Several organic sulfides typical to soils (methionine, cysteine, cystine) and elemental sulfur also yield good results, but all other sulfur compounds do not yield good results. This will further be discussed in section 3.5.5.

3.5.4.2. BESSY II dataset

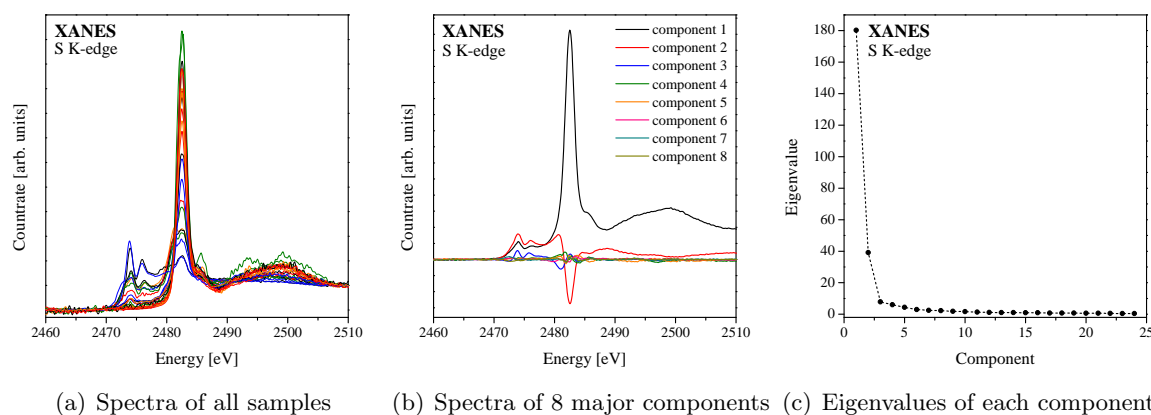


Figure 3.25.: Summary of PCA for all soil samples.

Figures 3.25 to 3.31 represent the principal component analysis performed on the second dataset, the spectra of those Teufelsberg horizons and debris components measured at Bessy II. Figure 3.25 shows the whole dataset of all measured sample spectra, as well as the spectra of the first eight components (the principal components), and a plot of the eigenvalues of each component. In the following, the reconstruction of representative samples with a different number of components is shown, to demonstrate the choice of eight principal components for this dataset. Generally, reconstructions with two, four, six, and eight components are shown. For some sam-

ples, reconstructions with a different number of components are added, if important changes occurred during the respective reconstruction.

For sample dc17 (figure 3.26), the first fit using only the first two components is already almost perfect, with only slight deviations in the sulfide and post-edge range. With four components, the reconstruction becomes perfect and does not change anymore when switching to six and eight components.

For sample dc14 (figure 3.27), which is also a pure sulfate, but showing more detailed post-edge structure compared to dc17, a fit with the first two components is already quite good, but it shows distinct discrepancies in the post-edge region. The fit improves significantly using four components and gets perfect with five components. It does not change anymore when using six or eight components.

For horizon c1 (figure 3.28), the first fit using only the first two components is already quite good, with small errors in the sulfoxide to sulfonate energy range. The fit improves significantly using four components and becomes perfect with six components. Switching to eight components does not yield any improvements.

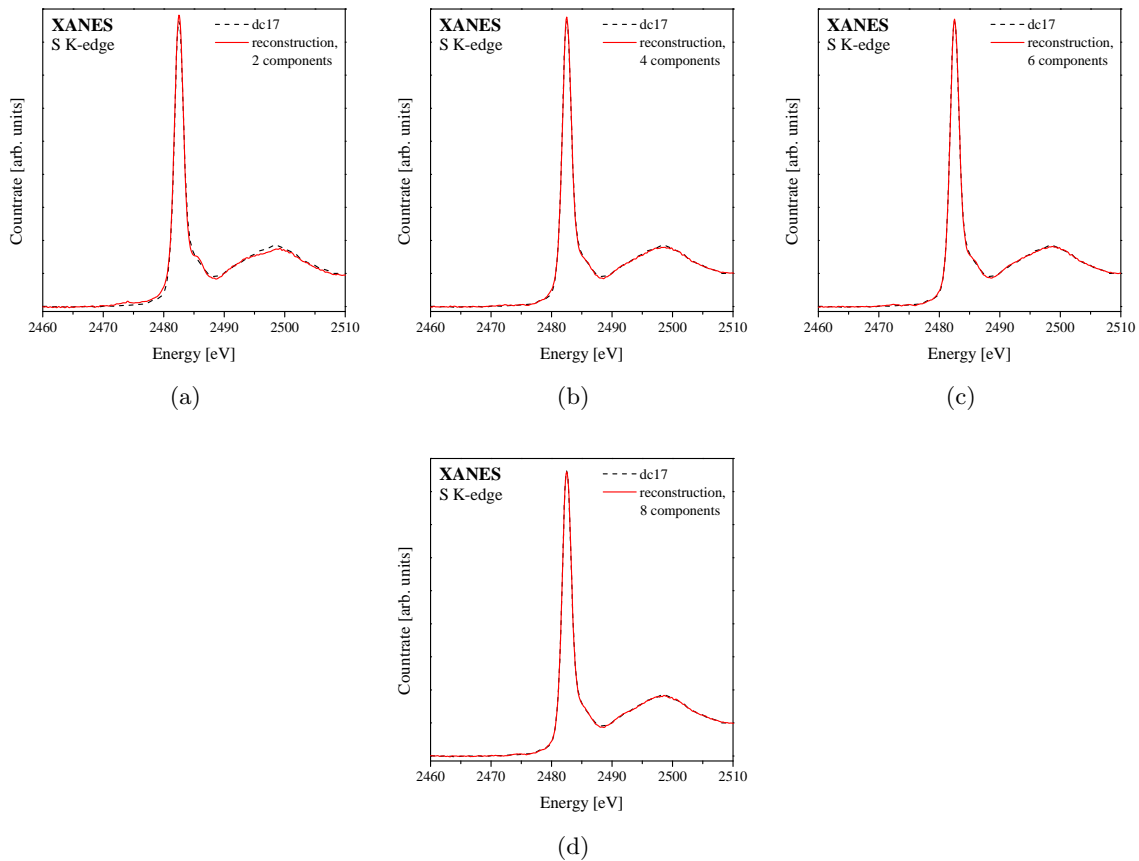


Figure 3.26.: Reconstruction of sample dc17 (black crystalline material) with different number of components.

For the pyrolyzed material dc11 (figure 3.29), a reconstruction with only two components yields a very bad fit. It improves dramatically with three components, with only small deviations in the sulfone energy range. The fit further improves insignificantly when switching to four and six components and only gets perfect with eight components.

The results are similar for pyrolyzed material sample dc21 (figure 3.30). The first two components yield a rather bad fit, that dramatically improves using three components. The reconstruction does not improve with four components, as it still shows small discrepancies in the sulfoxide to sulfone energy region. Six components yield a very good fit and the reconstruction gets perfect using eight components.

For horizon g2 (figure 3.31), a reconstruction with two components yields a moderate fit, with deviations in the sulfide to sulfonate energy range. With three components, the fit improves in the upper sulfide as well as sulfoxide to sulfonate energy range, but gets slightly worse in the sulfate range. Using four and six components does not yield any improvements. The reconstruction becomes almost perfect using seven components with only slight deviations in the sulfide energy range, where a feature of a very reduced sulfide species still seems to be missing. The fit gets perfect with eight components.

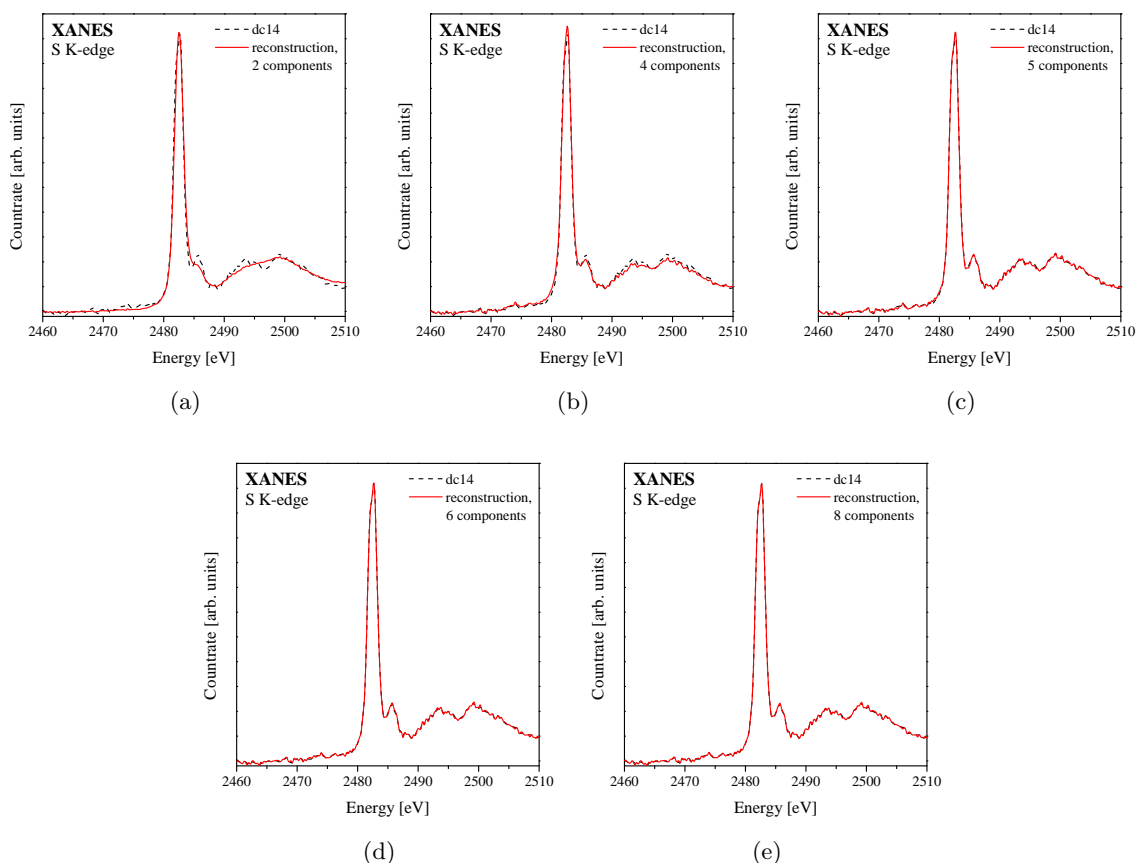


Figure 3.27.: Reconstruction of sample dc14 (ocher clay brick) with different number of components.

It can be concluded that the minimal number of principal components in this dataset is eight. It is only possible to perfectly reconstruct all variances in all spectra when eight components are used. This result is somewhat surprising, since the dataset is very similar to the SLRI dataset and therefore an identical result could be assumed. The BESSY II dataset comprises a subset of the SLRI dataset, in terms of several horizons and additionally several debris spectra. However, the debris components are the parent material of the measured horizons and can therefore be regarded as incorporated in those spectra.

However, the measured and analyzed energy range of the spectra is considerably larger for the BESSY II dataset than for the SLRI data, covering the whole post-edge region. This results in more features that need to be reconstructed in the fits. Moreover, pure debris components certainly comprise other (higher) concentrations for certain sulfur species than soil horizons incorporating small amounts of that parent material.

Target transformation was performed on the basis of the eight major components of this dataset and the standard spectra listed in table A.1. The results are very similar to those obtained for the SLRI dataset. Most sulfates and some organic sulfides yield good fits, while all other sulfur compounds do not. Again, for CaSO_4 , the chi-square value gets worse with rising concentration and CaSO_4 generally gives the best results.

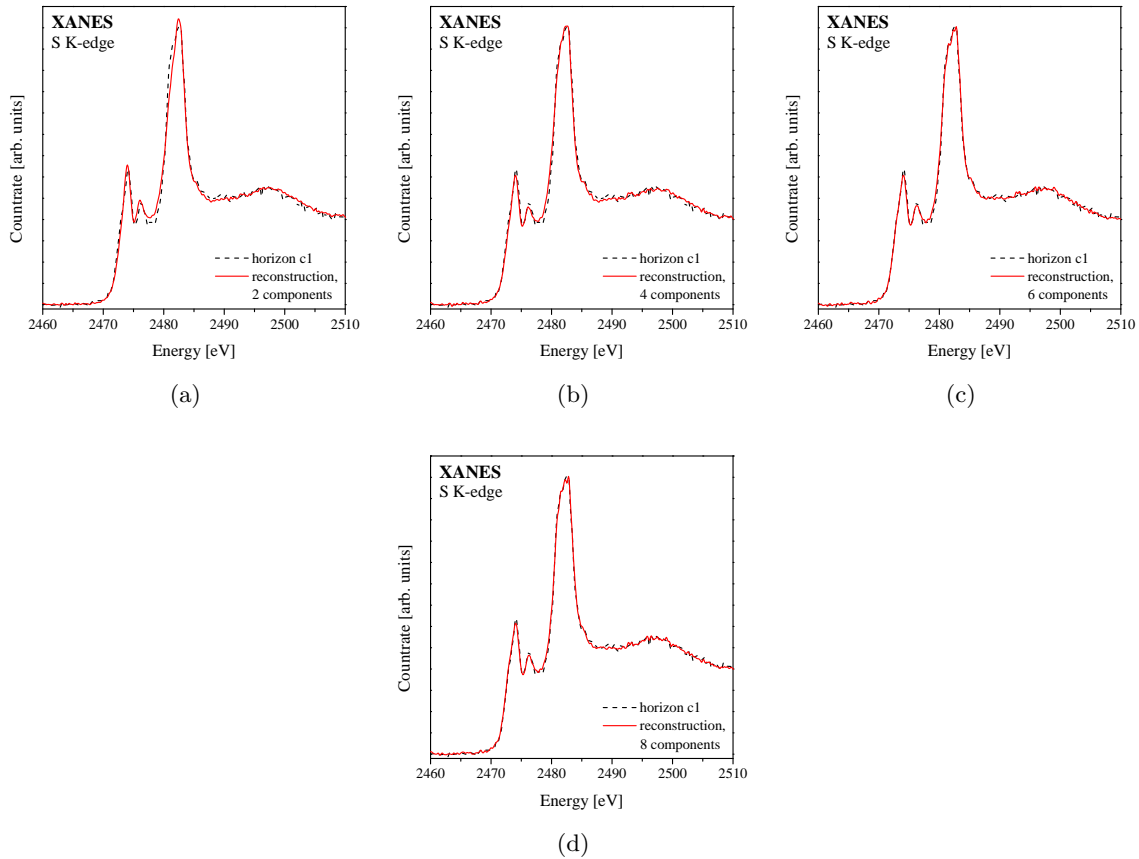


Figure 3.28.: Reconstruction of horizon c1 with different number of components.

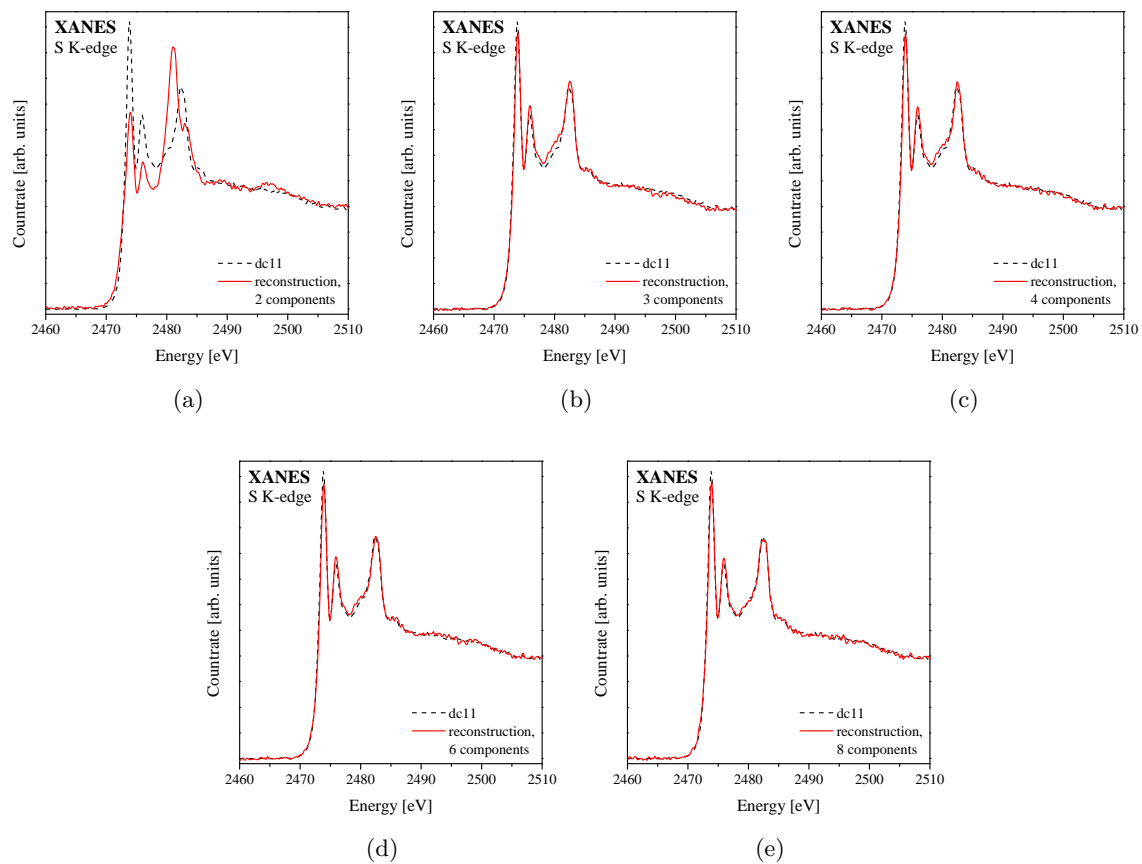


Figure 3.29.: Reconstruction of sample dc11 (pyrolyzed material) with different number of components.

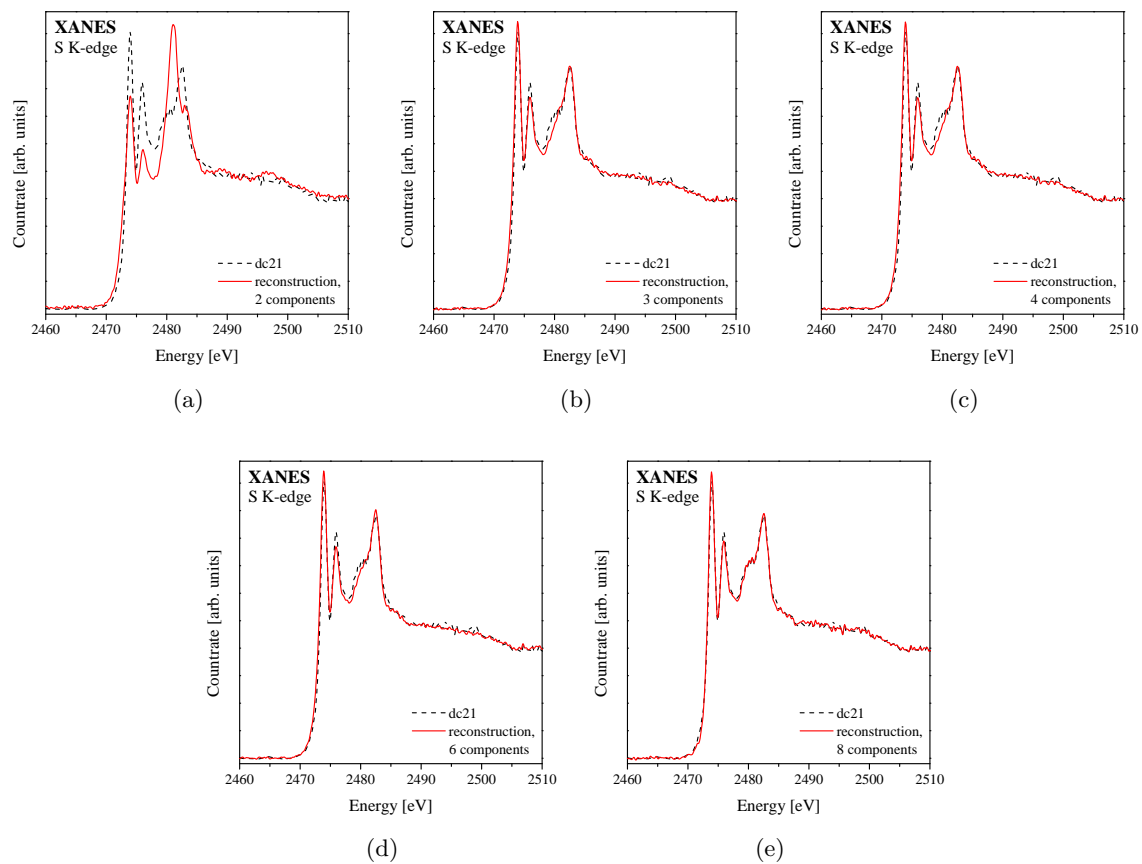


Figure 3.30.: Reconstruction of sample dc21 (pyrolyzed material) with different number of components.

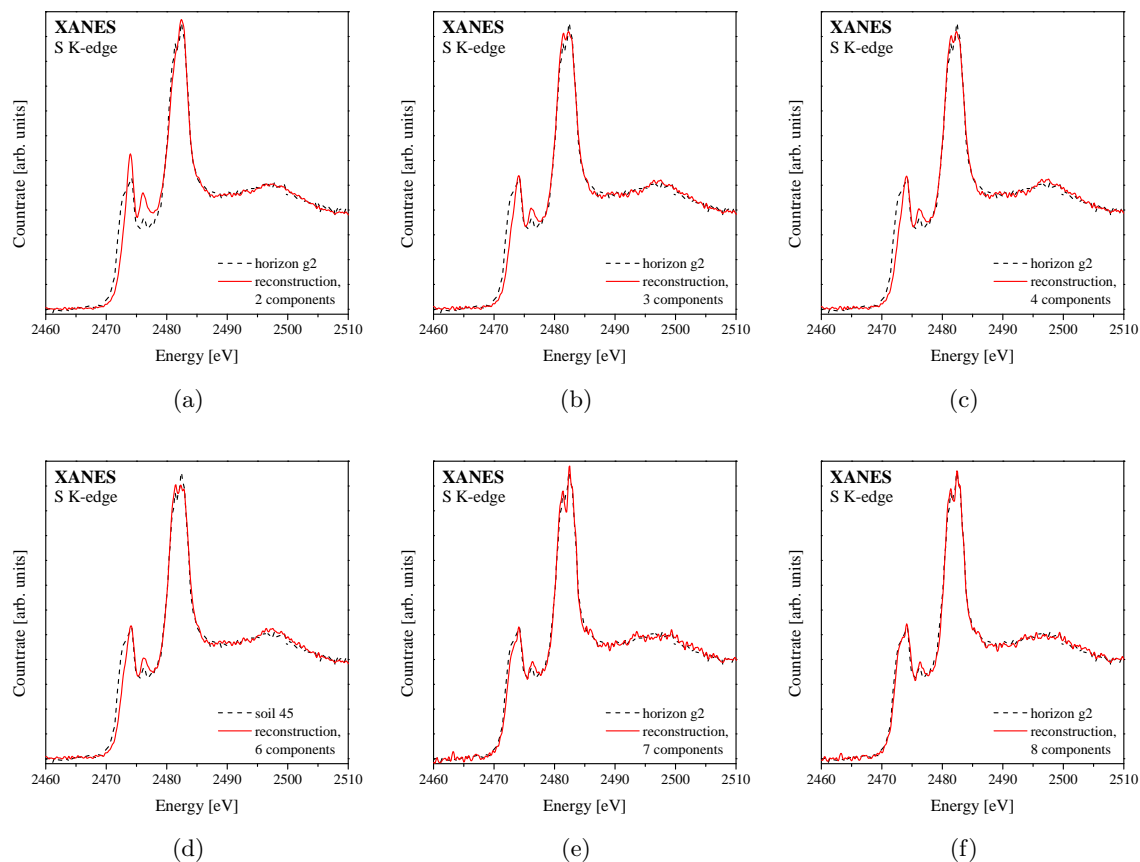


Figure 3.31.: Reconstruction of horizon g2 with different number of components.

3.5.5. LCF

The basics of linear combination fitting are given in section 2.3. To evaluate the potential, applicability and boundaries of this method, it was initially tried on a series of prepared mixtures of different sulfur compounds and soil and debris samples. Afterward, it was applied on several samples of soil horizons, that have already been analyzed by peak fitting. The used standard spectra are given in table A.1. LCF of the prepared mixtures was performed using the software packages SIXPACK and ATHENA, both giving identical results. For the soil samples only SIXPACK was used, just because it was considered to be more user-friendly.

3.5.5.1. LCF of prepared mixtures

The prepared mixtures can be classified by the complexity of their spectral features and divided up into different categories: standards of identical or similar oxidation states, standards of different oxidation states, different debris components, and debris components and soil samples. All mixtures were prepared by ratios of 1:1 in weight-%, all used standards were diluted with pure quartz sand by 1:1000. Dilution as well as mixing was done using milligram scales. A list

of prepared mixtures is given in table 3.5. All mixtures were measured at KMC-1 at BESSY II with 0.25 eV step size and 1 s dwell time, as described at the beginning of this chapter.

no	components
1	Cysteine, Pyrite
2	Pyrite, Marcasite
3	CaSO ₄ , Al ₂ (SO ₄) ₃
4	CaSO ₄ , BaSO ₄
5	CaSO ₄ , CuSO ₄
6	CaSO ₄ , Al ₂ (SO ₄) ₃ , FeSO ₄
7	MgSO ₄ , (NH ₄) ₂ SO ₄ , CaSO ₄ , BaSO ₄ , CuSO ₄ , FeSO ₄ , Na ₂ SO ₄ , Al ₂ (SO ₄) ₃
8	Cysteine, CaSO ₄ , Anthraquinone sulfonic acid
9	dc8, dc11, dc18
10	dc11, dc12, dc18
11	dc11, horizon g1
12	dc12, horizon g1

Table 3.5.: List of prepared mixtures, each mixed by ratio 1:1 in weight-%.

Since a quantitative analysis of XAS data always yields ratios in atom-%, the ratios of the prepared mixtures need to be converted. For the used standards, this can easily be done by their molar mass and number of sulfur atoms. All relevant data is given in table 3.6. For soil and debris components, the conversion is done by their total sulfur concentration in weight-%, given in tables 3.2 and 3.3. The results of linear combination fitting of all mixtures are given in figures 3.32 to 3.43. In each diagram, the measured data, the fit obtained from linear combination fitting, and the compounds present in the specific mixture are plotted on top of each other. In this way, the goodness of the fit can easily be judged qualitatively. For some fits an additional linear function was introduced, which can adjust slight normalization errors. The ratios obtained from linear combination fitting are generally given within each diagram, the actual values are given in the captions. For some mixtures, for which LCF did not yield satisfactory fits, a second diagram is plotted, in which a fit is constructed from the actual values.

Mixtures one and two, displayed in figures 3.32 and 3.33, are both mixtures of two diluted sulfide standards. Cysteine and Pyrite in mixture one (figure 3.32) are separated by a chemical shift of 1.2 eV and LCF yields a perfect fit, which gives the actual ratios of this mixture. Marcasite and Pyrite in mixture two (figure 3.33) are only separated by 0.3 eV. Both substances are partly oxidized, but Marcasite to a much bigger extend. LCF yields a significant deviation from the real values. However, a constructed fit using the actual ratios yields a very good result, except for the sulfate peak.

Mixtures three to seven, shown in figures 3.34 to 3.38, are comprised of a different number of diluted sulfate standards. Therefore, the compounds do not exhibit any chemical shift and can only be distinguished by their pre- and post-edge features and the shape of the white line.

Mixture three (figure 3.34) consists of CaSO_4 , with distinct and specific post-edge features, and $\text{Al}_2(\text{SO}_4)_3$, without characteristic features. LCF gives a good result, close to the actual values. Mixture four (figure 3.35) comprises CaSO_4 and BaSO_4 , both with characteristic post-edge features. For this mixture LCF also yields a good result.

Mixture five (figure 3.36) consists of CaSO_4 and CuSO_4 , whereat the latter exhibits a characteristic, although small pre-edge peak, but no characteristic post-edge features. Here, LCF yields a very unsatisfying result: pure CaSO_4 . However, a constructed fit using the actual ratios shows a good result. The deviation in the height of the white line is increased, but the fit is significantly improved in the post-edge region.

Mixture six (figure 3.37) comprises three sulfates, CaSO_4 , FeSO_4 , and $\text{Al}_2(\text{SO}_4)_3$. The spectral shape of FeSO_4 and $\text{Al}_2(\text{SO}_4)_3$ is very similar, without any characteristic pre- and post-edge features. Therefore, both are completely interchangeable in LCF analysis. But even assuming that either FeSO_4 or $\text{Al}_2(\text{SO}_4)_3$ could represent the sum of both, LCF gives a bad result. The fit constructed from the actual values, on the other hand, shows similar deviations to that obtained from LCF.

chemical name	formula	family	molar mass [g/mol]
aluminum sulfate	$\text{Al}_2(\text{SO}_4)_3$	sulfate	342.15
ammonium sulfate	$(\text{NH}_4)_2\text{SO}_4$	sulfate	132.14
anthraquinone sulfonic acid	$\text{C}_{14}\text{H}_7\text{NaO}_5\text{S}$	sulfonate	310.20
barium sulfate	BaSO_4	sulfate	233.39
calcium sulfate	CaSO_4	sulfate	136.11
copper sulfate	CuSO_4	sulfate	159.61
cysteine	$\text{C}_3\text{H}_7\text{NO}_2\text{S}$	sulfide	121.16
dimethylsulfone (methylsulfonylmethane)	$\text{C}_2\text{H}_6\text{O}_2\text{S}$	sulfone	94.13
iron sulfate	FeSO_4	sulfate	151.91
magnesium sulfate	MgSO_4	sulfate	120.37
marcasite	FeS_2	sulfide	119.98
pyrite	FeS_2	sulfide	119.98
sodium sulfate	Na_2SO_4	sulfate	124.04

Table 3.6.: Summary of substances used for mixtures.

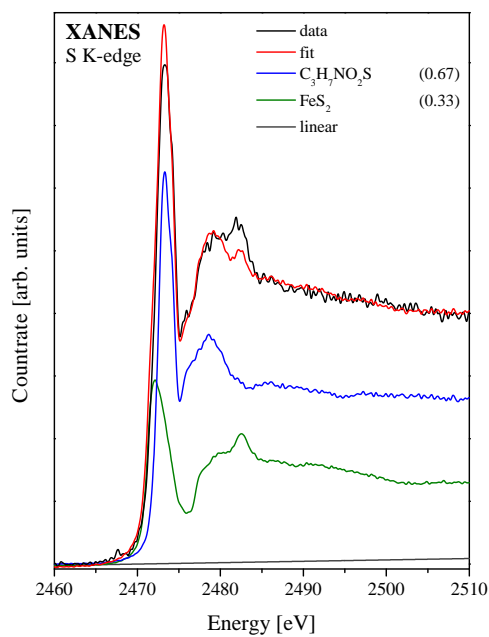
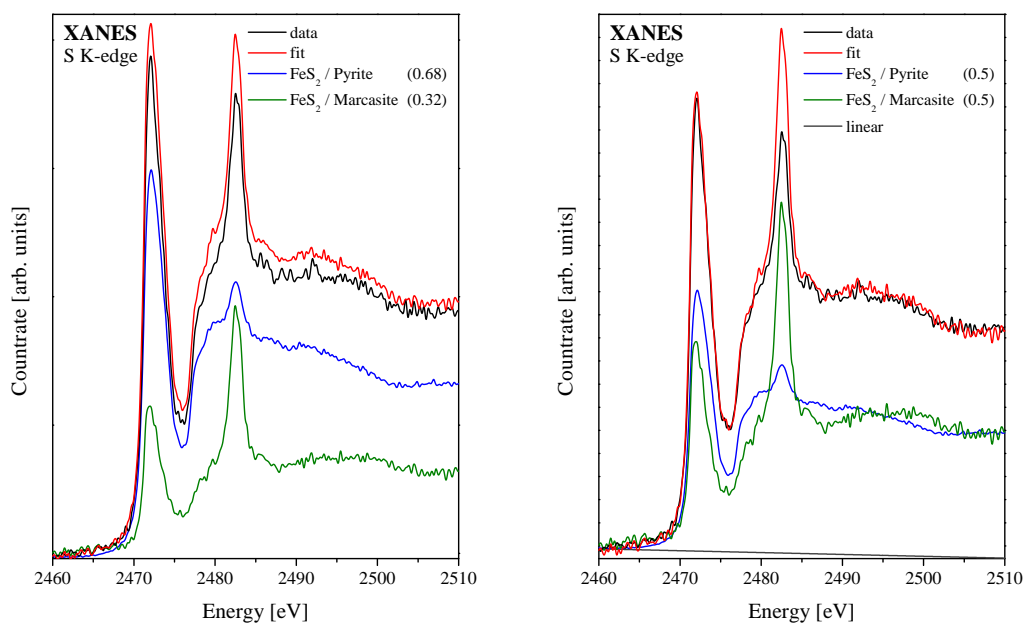


Figure 3.32.: Mixture 1: Cysteine (0.67), Pyrite (0.33)



(a) LCF

(b) constructed with actual ratios

Figure 3.33.: Mixture 2: Pyrite (0.5), Marcasite (0.5).

Mixture 7 (figure 3.38) comprises eight different sulfates, some with and some without characteristic pre- and / or post-edge features. Obviously, this system is over-determined. By LCF, different, equally good fits can be obtained, with varying ratios of the different compounds, simply depending on their succession in the data input mask (of SIXPACK). A constructed fit using the actual ratios naturally also yields a good result.

Mixture eight, displayed in figure 3.39, consists of three sulfur standards of different oxidation states: Cysteine, an organic sulfide, Anthraquinone sulfonic acid, a sulfonate, and CaSO_4 , a sulfate. The compounds are well separated in energy by at least 1.2 eV. The fit obtained from LCF represents the data almost perfectly and the obtained ratios are quite close to the actual ones.

Mixtures nine and ten, shown in figures 3.40 and 3.41, comprise different debris components. For both mixtures, LCF yields perfect fits, except for the emerging shoulder in mixture nine, which has already been discussed in section 3.3. The resulting ratios, however, significantly deviate from the actual values.

Mixture 11 (figure 3.42) consists of debris component dc11, and soil horizon g1. LCF yields very good results, in terms of a good fit and output of the exact ratios.

Mixture 12 (figure 3.43) comprises clay brick dc 12 and horizon g1. LCF yields a good fit, but ratios deviating from the actual ones. A constructed fit using the actual ratios also reproduces the data nicely, yielding an improved fit in the sulfide energy range, but increased deviation for the sulfate peak. The pronounced sulfoxide peak, however, cannot be fitted. Its origin is unclear.

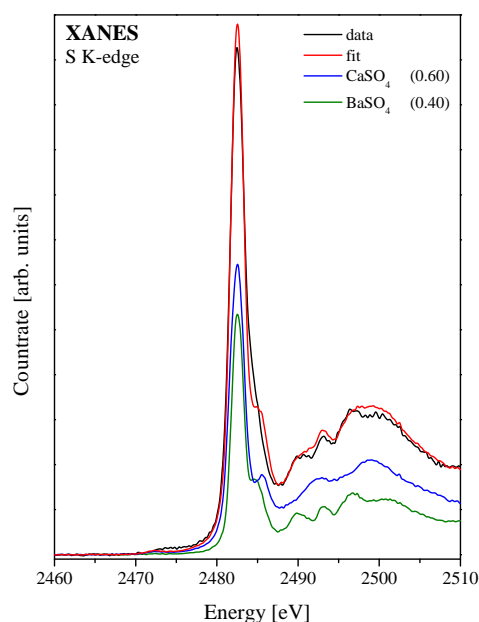
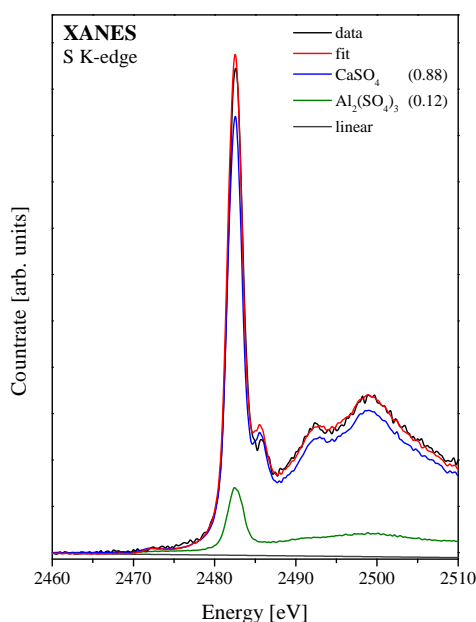


Figure 3.34.: Mixture 3: CaSO_4 (0.91), $\text{Al}_2(\text{SO}_4)_3$ (0.09). **Figure 3.35.:** Mixture 4: CaSO_4 (0.59), BaSO_4 (0.41).

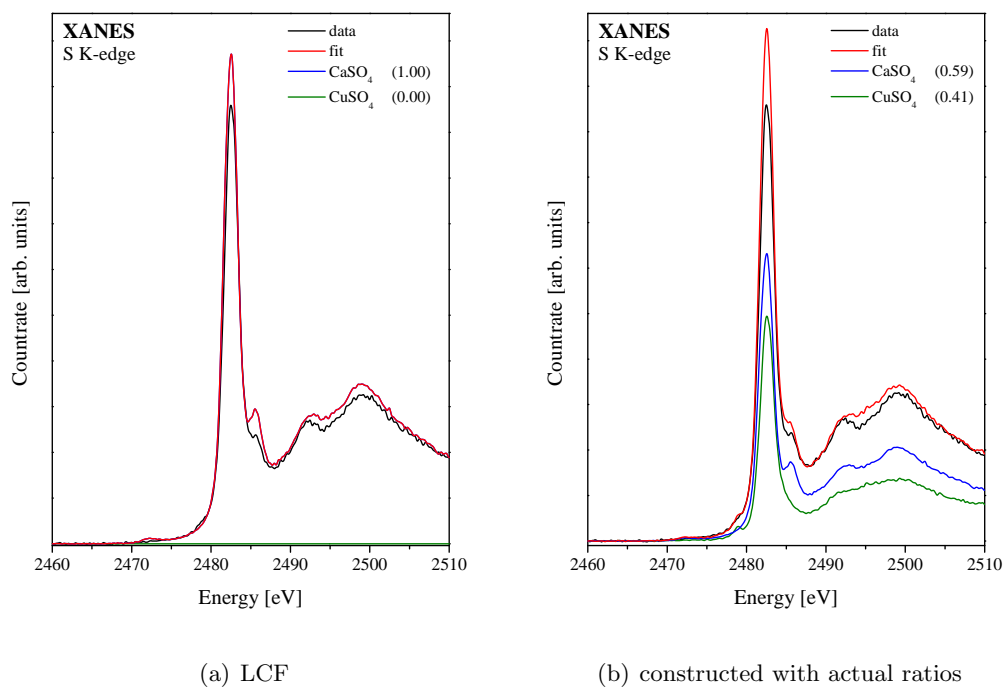


Figure 3.36.: Mixture 5: CaSO_4 (0.59), CuSO_4 (0.41).

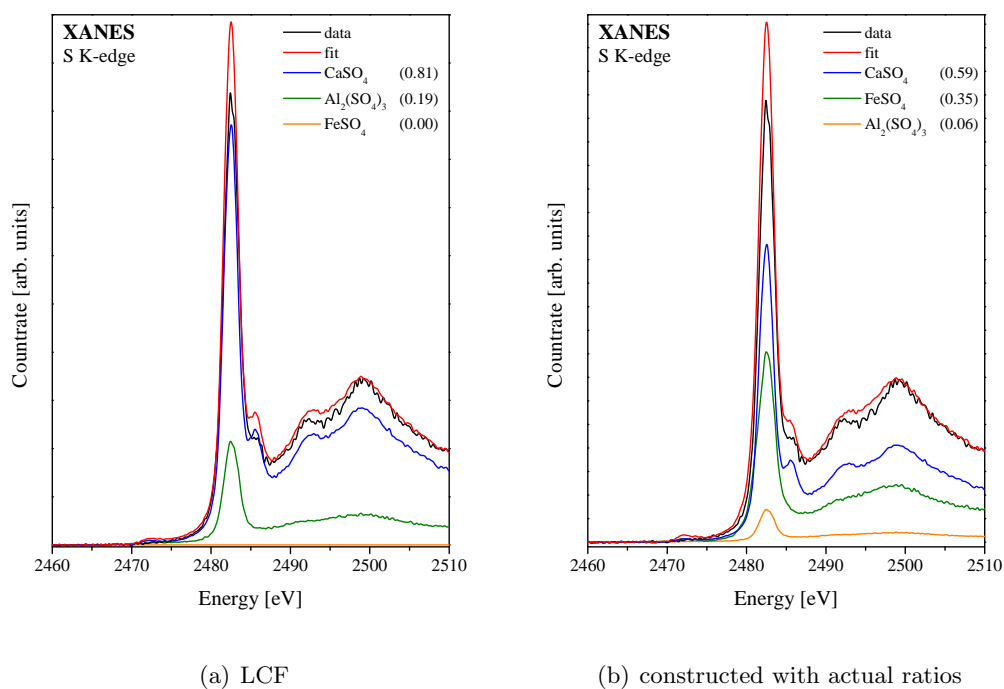


Figure 3.37.: Mixture 6: CaSO_4 (0.59), FeSO_4 (0.35), $\text{Al}_2(\text{SO}_4)_3$ (0.06).

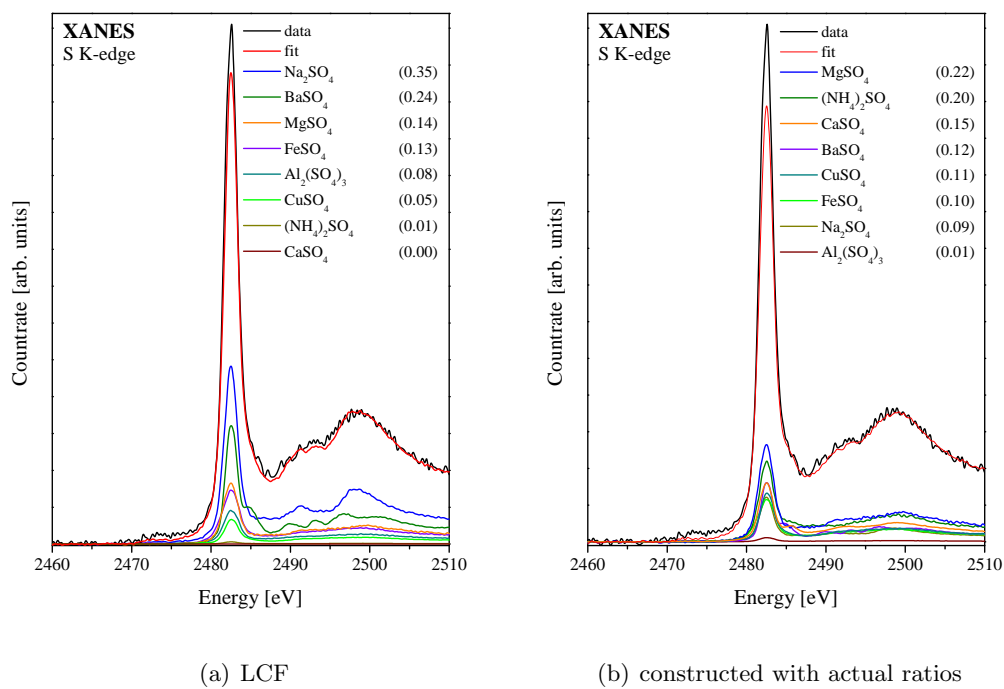


Figure 3.38.: Mixture 7: MgSO_4 (0.22), $(\text{NH}_4)_2\text{SO}_4$ (0.20), CaSO_4 (0.15), BaSO_4 (0.12), CuSO_4 (0.11), FeSO_4 (0.10), Na_2SO_4 (0.09), $\text{Al}_2(\text{SO}_4)_3$ (0.01).

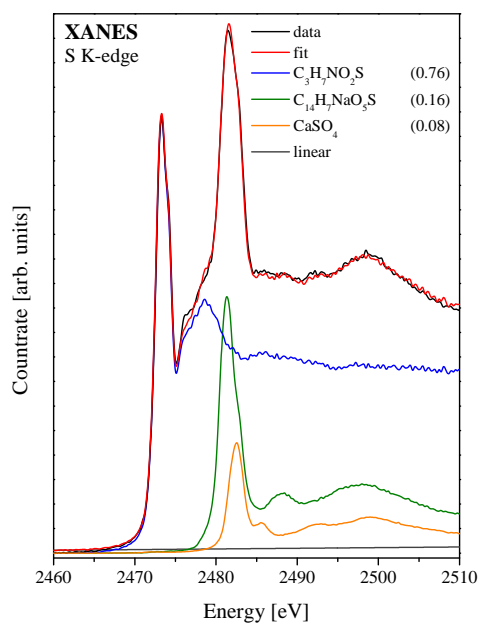


Figure 3.39.: Mixture 8: Cysteine (0.72), Anthraquinone Sulfonic Acid (0.019), CaSO_4 (0.09).

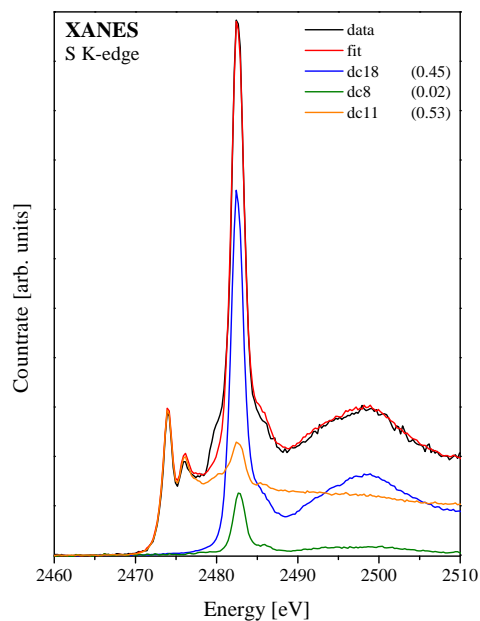


Figure 3.40.: Mixture 9: dc11 (0.75), dc18 (0.23), dc8 (0.02).

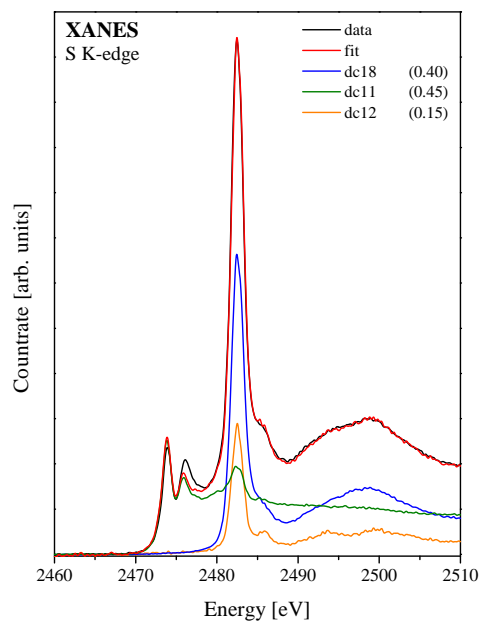


Figure 3.41.: Mixture 10: dc11 (0.72), dc18 (0.21), dc12 (0.07).

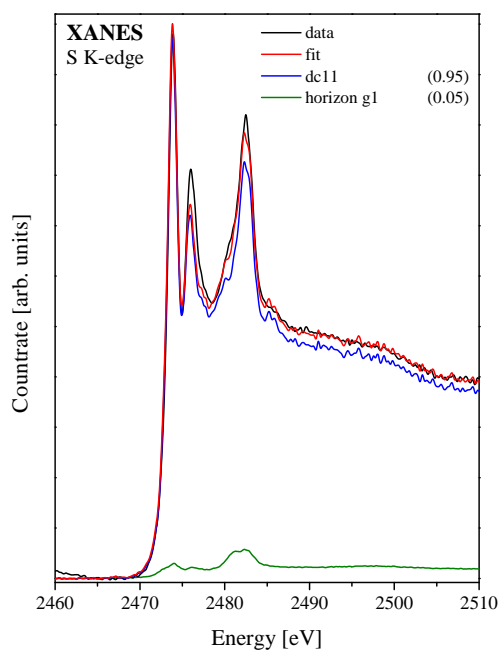


Figure 3.42.: Mixture 11: dc11 (0.95), horizon g1 (0.05).

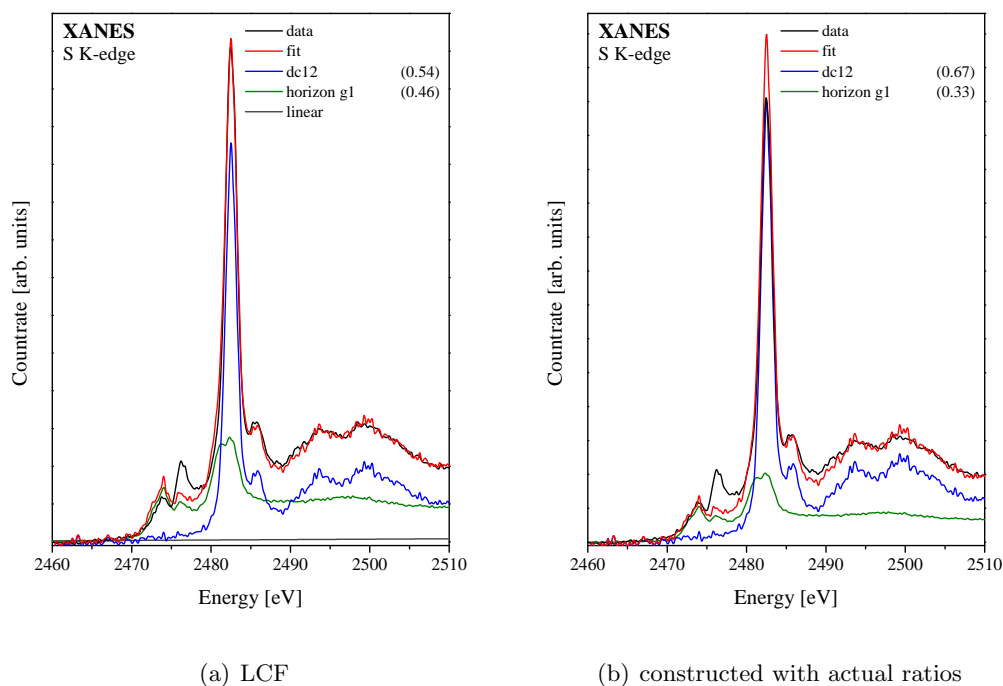


Figure 3.43.: Mixture 12: dc12 (0.67), horizon g1 (0.33).

In conclusion, it can be stated that LCF yields good results if the different species in a mixture are clearly distinguishable by either energy position of the white line (mixtures 1 and 8) or characteristic spectral features (mixtures 3, 4 and 11). The results become inaccurate (mixture 2) or even arbitrary (mixtures 6 and 7), if the involved components are too similar. However, if the goal is to rather extract the total ratio of the occurring oxidation states than to extract the ratios of each compound (e.g. each sulfate), LCF will still work (mixture 8). Small deviations of the fitted from the actual ratios are certainly due to the preparation method and experimental setup. Neither the dilution nor the mixing using a spatula and milligram scales is absolutely exact. Moreover, due to the small spot size at KMC-1, the measurements are sensitive to local variations in sample composition and concentration. The LCF routine, on the other hand, seems to be especially sensitive to white line peak heights, as can explicitly be seen in the fitting results of mixture 5. Constructed fits using the actual ratios of the mixtures always lead to improved fits for a wide energy range, but to increased deviations in the white line peaks (and therefore to a reduced total goodness of fit).

Errors in mixtures 9 and 10 could be due to wrong values of the total sulfur concentration within the involved components.

3.5.5.2. LCF of soil samples

Several Teufelsberg horizons, also analyzed by peak fitting in section 3.5.3, were analyzed with linear combination fitting. A representative selection is shown in figures 3.44 to 3.49. Figures 3.44

to 3.48 are SLRI data, while figure 3.49 is BESSY II data and used for comparison. The utilized standards are listed in table A.1. Initially, it was tried to only use those standards, that yielded good or at least moderate results in target transformation, see section 3.5.4. However, this procedure did not result in meaningful fits, as good and moderate results in target transformation were only obtained for various sulfides, some sulfonates and all sulfates.

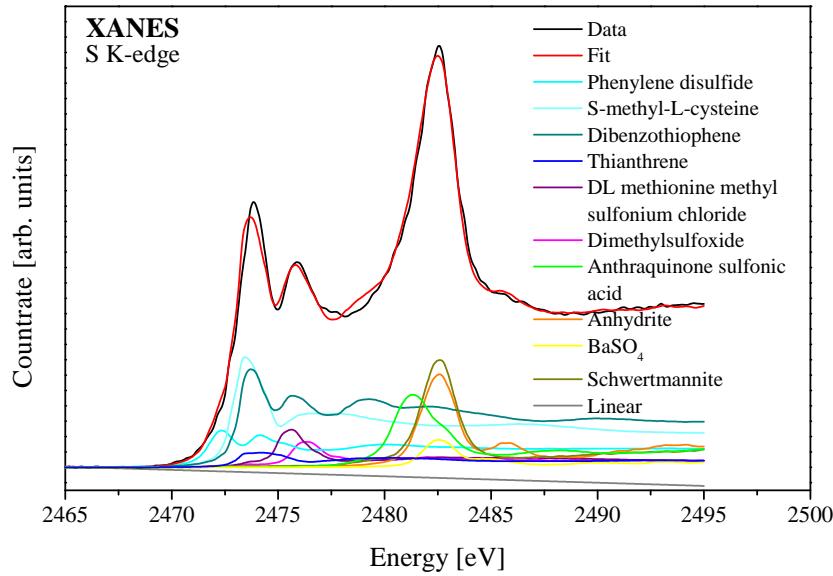


Figure 3.44.: LCF analysis of horizon a2, chi-square = 0.5, $\Delta E = -0.07$ eV.

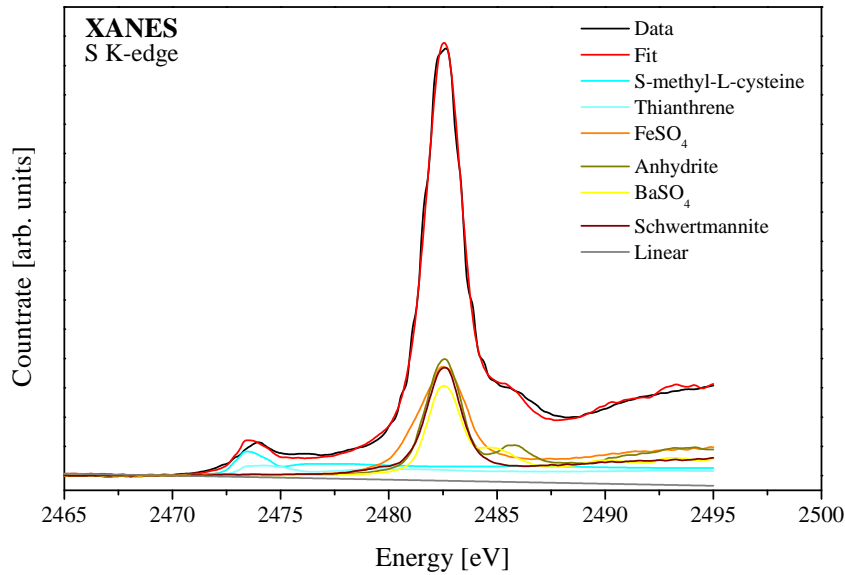


Figure 3.45.: LCF analysis of horizon c4, chi-square = 2.8, $\Delta E = 0.02$ eV.

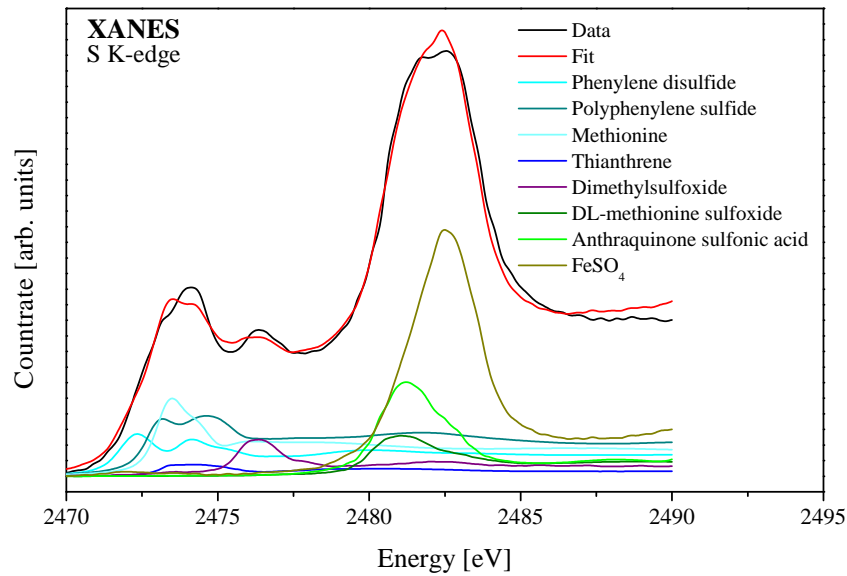


Figure 3.46.: LCF analysis of horizon c1, chi-square = 1.4.

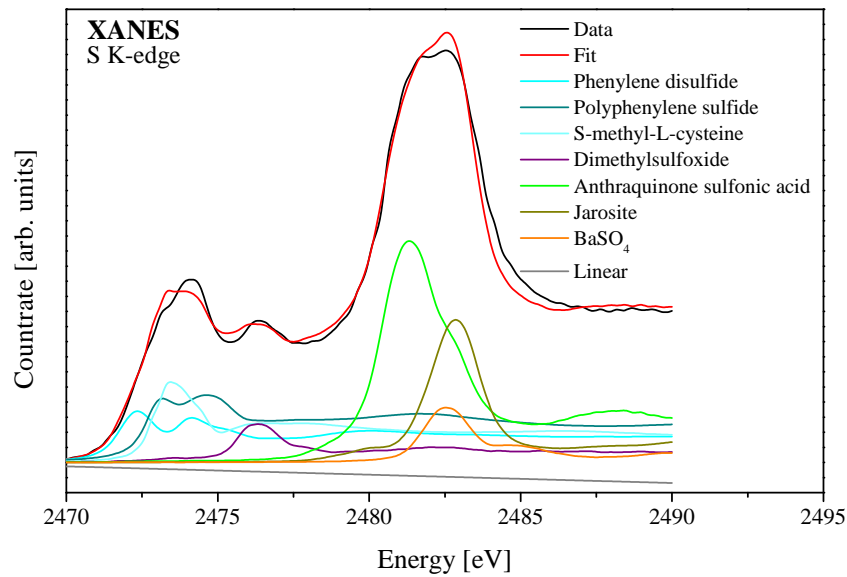


Figure 3.47.: LCF analysis of horizon c1, chi-square = 1.8.

Thereupon, linear combination fitting was performed on all samples trying all available standards in succession. For SLRI data, a linear function was included in the fit, to account for normalization errors. An energy shift was generally allowed in the fits, to account for calibration errors. The resulting shift is generally quite low, in the range of 0.01 to 0.2 eV. The obtained fits are generally quite good, as exemplarily shown for horizons a2 and c4 in figures 3.44 and 3.45. However, deviations remained in many fits for a sharp sulfide feature at roughly

2474 eV, that could not be fitted. Furthermore, in many fits the sulfoxide peak could not be fitted satisfactorily, as the dataset of sulfoxide standards is very limited.

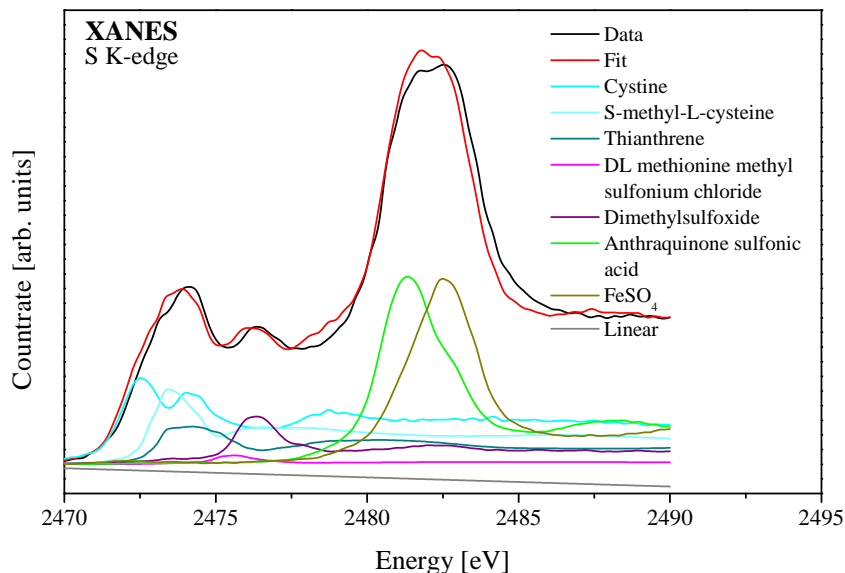


Figure 3.48.: LCF analysis of horizon c1, chi-square = 1.3, $\Delta E = -0.16$ eV.

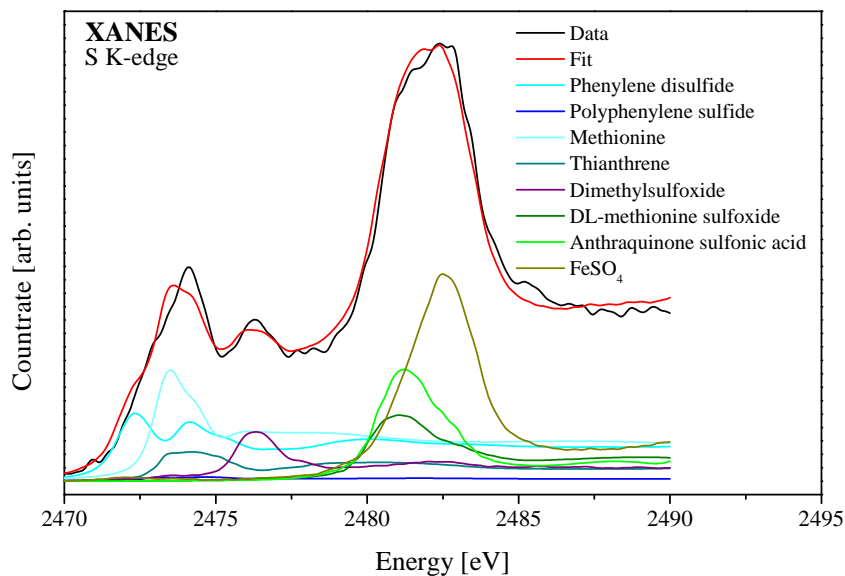


Figure 3.49.: LCF analysis of horizon c1, chi-square = 1.6, $\Delta E = -0.13$ eV.

The substances used for the respective fits are displayed within the diagrams. Remarkably, those standards, that yield the best results in target transformation seldom occur in the fits. CaSO_4 , which obtained the best result, never occurs in a fit. On the other hand, substances

that obtained only bad or moderate results, such as Dimethylsulfoxid, Thiantrene or BaSO₄, occur regularly.

On the basis of horizon c1, the fitting procedure was further evaluated. Initially, the SLRI spectrum of horizon c1 was fitted without linear function and energy shift. The result is shown in figure 3.46. Then, a linear function was added and all standards tried again in succession, yielding a similar fit, but comprising different standard spectra (figure 3.47). In figure 3.48, a linear function was added and an energy shift was allowed. This procedure yields again a satisfying fit, again comprising different standards. Additionally, a BESSY II spectrum of horizon c1 was fitted, which is displayed in figure 3.49. No linear term was added, but an energy shift was allowed. The fit is similar to those obtained for SLRI data, while the general problem of the 2474 eV peak is obvious throughout all fits. Surprisingly, this fit comprises the same standards as the first SLRI fit. The four different fits for horizon c1 demonstrate nicely, that the standard spectra obtained from the LCF routine, with which the data can be reconstructed, are not necessarily real components of the sample. Adding their spectral features simply yields a good fit. One could argue, that for example the real sulfide component is not in the database, particularly since a specific feature could not be fitted. However, the most abundant sulfide compounds in soils are present. Furthermore, an extensive amount of sulfate spectra is available from the database, but the sulfate substances present in the fits also vary and deviations do also occur in this energy range.

sample	sulfide	sulfoxide	sulfone	sulfonate	sulfate	analysis method	diagram
SLRI data:							
horizon a2	62.3	9.2	2.7	4.6	21.2	peak fitting	
	65.6	7.3		7.3	19.8	LCF	figure 3.44
horizon c4	18.1	0.2	5.0		76.6	peak fitting	
	15.9				84.1	LCF	figure 3.45
horizon c1	55.0	2.8	5.3	16.5	20.3	peak fitting	
	50.0	5.0		18.0	27.0	LCF	figure 3.46
	51.9	4.8		21.2	22.1	LCF	figure 3.47
	50.5	7.9		19.8	21.8	LCF	figure 3.48
BESSY II data:							
horizon c1	54.0	4.0	1.4	19.0	21.0	peak fitting	
	51.8	7.0		17.5	23.7	LCF	figure 3.49

Table 3.7.: Comparison of analysis methods for soil horizons displayed in figures 3.44 to 3.49. Contributions of each oxidation state are given in %.

However, the occurring sulfur compounds can be sorted by white line peak energy or rather oxidation state (index), and their specific contributions can be added. This way, ratios of the occurring oxidation states can be calculated, similar to the results obtained from peak fitting. This was done for the six shown fits and is summarized in table 3.7. For comparison, the results for each horizon obtained from peak fitting are added. The listed values show good agreement for sulfides and sulfates, if a linear function is added and an energy shift is allowed. The maximal deviation between both analysis methods is roughly 12%. For intermediate oxidation states, the deviations are much more pronounced. However, in this energy range, significant deviations are also evident for the same sample (horizon c1), which was analyzed by using the same method, but measured at different beamlines.

LCF seems to prove that sulfone species are not abundant within the soil samples and that the fitted peaks in peak fitting analysis are rather due to pre- and post-edge features of other sulfur species. This was already suspected in section 3.5.3, since the amount of sulfone was evenly distributed throughout all horizons, without any meaningful pattern. If the amount of sulfone, obtained in peak fitting analysis is assigned to other oxidation states (depending on the sample mostly to sulfoxides or sulfonates), the deviations between both analysis methods for the intermediate oxidation states are diminished.

As already mentioned, fitting with certain standards chosen from a database, does not imply explicit quantification of that precise compound, but rather of total species of similar spectral shape and therefore same oxidation state (index). Obviously, LCF could be improved by finding more appropriate model compounds respectively standard spectra. Target transformation in PCA already indicated that the model compounds in the database are not ideal to fit the measured spectra. For some oxidation states simply more standards are desirable, while generally various concentrations are required. For fluorescence measurements, self absorption is a crucial issue and therefore, models should be measured in the same concentration as in the samples. If one can assume, that the samples are sufficiently diluted (in absolute concentration but also with respect to grain sizes), electron yield measurements would be desirable for standard spectra.

3.5.6. Error analysis

Error sources in this work are manifold and can be divided into three categories. Errors due to intrinsic sample properties and sample preparation, errors due to the applied measuring technique and beamline properties and errors arising from the applied data analysis method. Some of these errors are quantifiable in principle, others not.

Errors due to intrinsic sample properties and sample preparation mainly arise from the particulate character of the samples. Even thorough grinding only yields a maximal particle size but not a uniform one. Additionally, the small sample particles are of versatile origin (e.g. debris, organic soil material, soil minerals, etc.) and therefore of different sulfur speciation. The application on tape does also not yield a uniform sample thickness. This gives intrinsically heterogeneous samples of variable and eventually unknown thickness, which itself is a problem for quantitative sample analysis, but also results in variable self-absorption effects. Additionally, the particulate character gives rise to scattering effects and enhanced noise in the spectra, cp. section 3.3. These problems were taken into account and minimized by representative sampling, thorough grinding and mixing, and the usage of large spot sizes (SLRI) or measuring and averaging several spots on a sample (BESSY II, NSLS). Therefore, the errors arising from the applied measuring technique

and beamline properties are directly linked to those arising from sample properties and sample preparation. Self-absorption is a problem of the applied measuring technique, i.e. fluorescence, and is worsened and made unquantifiable by the variable and unknown sample thickness. Due to intrinsic sample heterogeneity the spot size of a beamline becomes a crucial factor concerning the representativeness of the measurement. The effects of the different errors can be observed nicely in the spectra of section 3.3. Figures 3.7 and 3.9 demonstrate differences in the spectra, which only occur due to self-absorption. This error declines with decreasing sulfur concentration of the sample (figure 3.9) because possible concentration differences diminish. Figures 3.10 comprise all described errors which may sum up to roughly 50 % (figure 3.10(d)).

Noise in the spectra is quantifiable in principle and could be used for error estimation. However, noise is of versatile origin: beamline layout (e.g. fill gases), type and number of detectors and experimental setup (e.g. dwell time), but also sample characteristics as described above. It can always be diminished by repeated measuring and averaging of the spectra. Hence, the resulting noise level in the shown spectra is a compromise of goodness of the spectra and available measuring time. Due to its large spot size and 13-element detector, SLRI yields good spectra with minimal time consumption. However, errors arising from noise in the spectra are generally much smaller than those arising from sample heterogeneities.

Errors arising from the applied data analysis method are comparable to those arising from noise in the spectra with respect to their order of magnitude, and depend on the noise level at the same time. They are generally calculated by the applied data analysis software and given in chi-square values (e.g. [77]). For peak fitting, errors could be minimized by usage of an indefinite number of gaussians, but then the fit would become physically meaningless. In linear combination fitting, errors can be minimized by usage of more adequate standard spectra, which is very time consuming (in sample preparation as well as actual beamtime).

Therefore, absolute numbers for error estimation are not given throughout this work. A critical contemplation of the obtained results, samples, measuring techniques, available standards, data analysis methods, etc. and their limitations is preferred.

4. Spectromicroscopy experiments

Spectromicroscopy experiments were performed at different beamlines as described in chapter 2. The elemental maps shown in this chapter were created and processed by using the software MAPS [75] or PyMCA [59], depending on the beamline at which the data was taken. MAPS was used for APS data from beamlines 2-ID-B and 2-ID-E, while PyMCA was used for ESRF data taken at beamline ID21. Both programs provide the possibility to create elemental maps from the detected fluorescence signals and to generate overlays of maximally three of these maps. Thereby, colocalizations of different elements within a sample can be investigated.

4.1. Spectromicroscopy samples

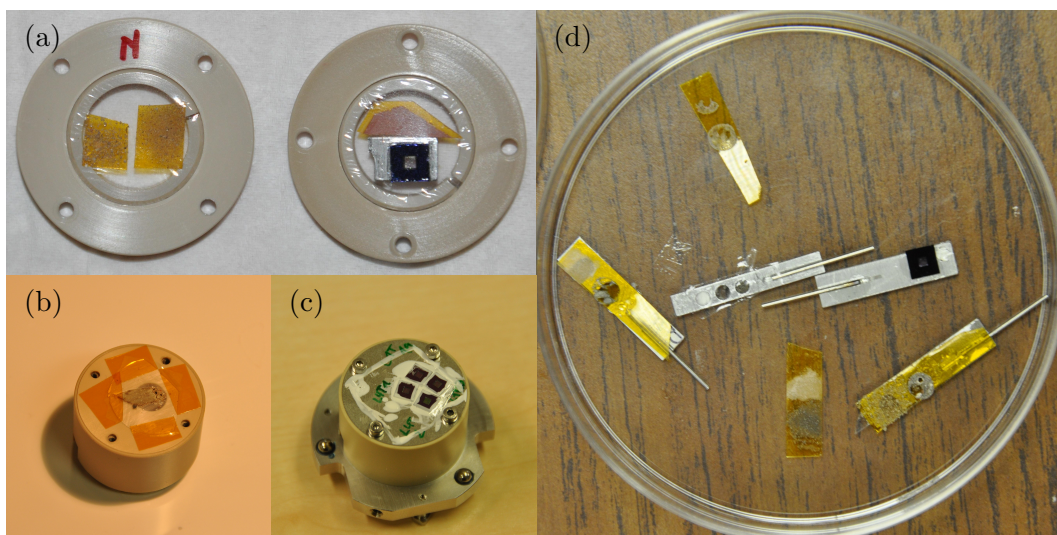


Figure 4.1.: Sample preparation and mountings for microscopy experiments at beamlines (a), (b) and (c) ID21 at ESRF and (d) 2-ID-B and 2-ID-E at APS. Samples are dry soil samples spread on tape or embedded in resin as well as liquid soil solution samples sealed between silicon nitride membranes.

Different types of samples were analyzed by x-ray spectromicroscopy. These are dry soil and debris samples as well as soil solution. All soil samples for spectromicroscopy experiments were taken from Schulgarten, because the Teufelsberg profiles are not available for repeated sampling. Samples were prepared in different ways, depending on sample type and beamline specification. For soil samples two approaches were applied. On the one hand, dry soil horizon samples were spread on sulfur free tape, similar to sample preparation for spectroscopy experiments, see section 3.5. For spectromicroscopy experiments, the soil samples are not ground and therefore, the

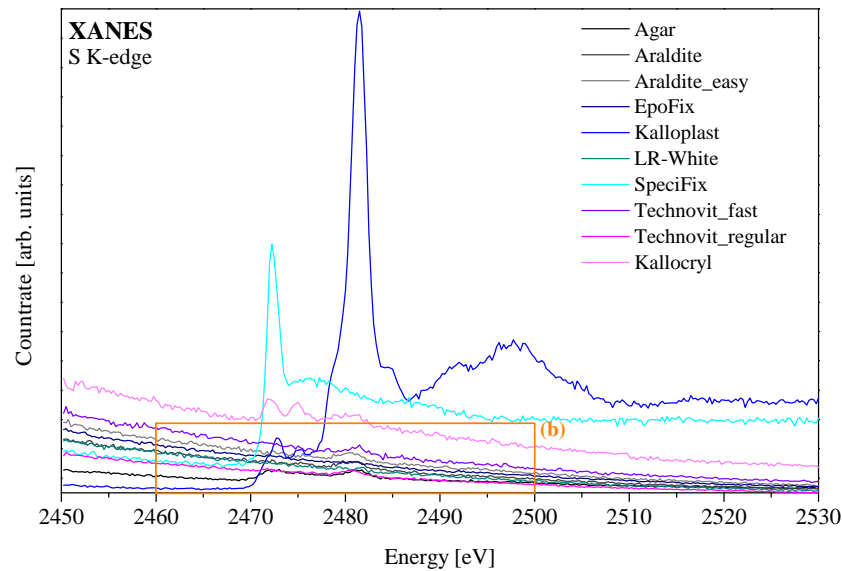
micro- and nanostructure and -composition should be preserved. This allows for studying small soil aggregates and debris particles, abundant in the specific horizon. On the other hand, soil samples were taken with soil sample rings under ambient conditions, dried, embedded in resin, and then cut into thin sections. As the soils contain large amounts of quartz, microtomes could not be applied. Therefore, a so-called "inside hole saw" was used and the thinnest achieved cuts are roughly 30 μm thick. These samples can directly be mounted on the different sample holders of the different beamlines, see figure 4.1.

First experiments on the sulfur load of soil solution obtained from laboratory experiments were also performed. Columns were packed with soils from different horizons and percolation experiments were conducted. For example, periods of dehydration in the soils or periods of extensive rain can be simulated in these columns. It is assumed, that the so called first flush (first rain after dehydration) serves as a major transport mechanism for sulfur components into the groundwater. One possible transport mechanism is the release of sulfur directly into the aqueous phase, by means of washed out colloids. Another one is the dissolution of sulfuric salts. Soil solution was obtained from percolation water and comprises leaching products and soil colloids. For experiments, the soil solution was sealed between two 200 nm thick silicon-nitride windows and then glued on a sample holder.

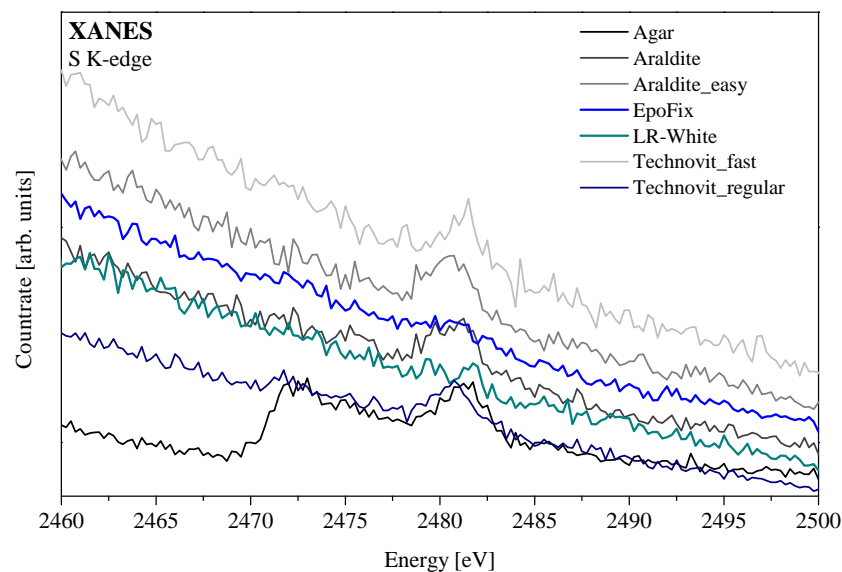
Regions of interest were chosen prior to the experiments by VLM (visible light microscope) and fluorescence (fly) scans. Especially for the soil samples, which are spread on tape, fluorescence fly scans are useful, as debris particles can be identified with high probability by their elevated sulfur content.

Absolute sulfur respectively sulfur species concentrations cannot be calculated. This is mainly due to unknown sample thickness and self-absorption effects. For particulate samples, the grain size is variable and difficult to measure. Additionally, grains are not ideal spheres and may intrinsically be heterogeneous. For thin sections, even the thickness of the sections can only roughly be estimated, as the thickness adjustment of the inside hole saw is rather imprecise and some samples are further thinned by grinding. Moreover, measured grains are not necessarily as thick as the thin sections.

4.1.1. Resins



(a) all tested resins



(b) the best resins

Figure 4.2.: Sulfur XANES spectra of all tested resins, taken at beamline KMC-1 at BESSY II.

Initially, two special resins (Kalloplast and Kallocryl (Speiko)), originally applied in orthodontics for prostheses, were used because the prevalent resins used in geology were suspected to comprise sulfur. However, during ESRF beamtime, significant amounts of sulfur were found just within

these resins. Therefore, samples of a variety of different resins typically used in geology and, in addition, Kallocryl and Kalloplast were measured at KMC-1 at BESSY II, to find the resin that is best suited for sulfur experiments. A list of all tested resins and their manufacturers is given in table A.2 of the Appendix. Cylinders of each pure resin and a sulfide (Cysteine) and sulfate (CaSO_4) standard embedded in each resin were prepared and thin sections were cut out of each. The sulfur K-edge XANES spectra of all tested resins are shown in figure 4.2(a). Obviously, Kalloplast, Specifix and Kallocryl contain significant amounts of sulfur and were therefore rejected. Figure 4.2(b) shows a zoom into figure 4.2(a) and represents all possibly suited resins that were not directly rejected. All of them only show trace amounts of sulfur and two of them are even sulfur free: EpoFix and LR-White. To further analyze their applicability to sulfur spectromicroscopy, their possible impact on sulfur oxidation state was evaluated. Figure 4.3 displays spectra of thin sections cut out of Cysteine and CaSO_4 standards embedded in each of the resins. For comparison, concentration series of both standards are added. Obviously, no changes in oxidation state or spectral features occur during the embedding and cutting process. The spectra of CaSO_4 embedded in both resins are found between the two most concentrated "pure" CaSO_4 spectra, while Cysteine in LR-White superposes "pure" Cysteine 10% and Cysteine in EpoFix is even less concentrated than the lowest "pure" concentration. Pure, in this case, means either in fact pure or diluted with quartz sand. The concentration of the standards in the resins is indeed somewhat arbitrary, as an arbitrary amount of standard substance was used for embedding.

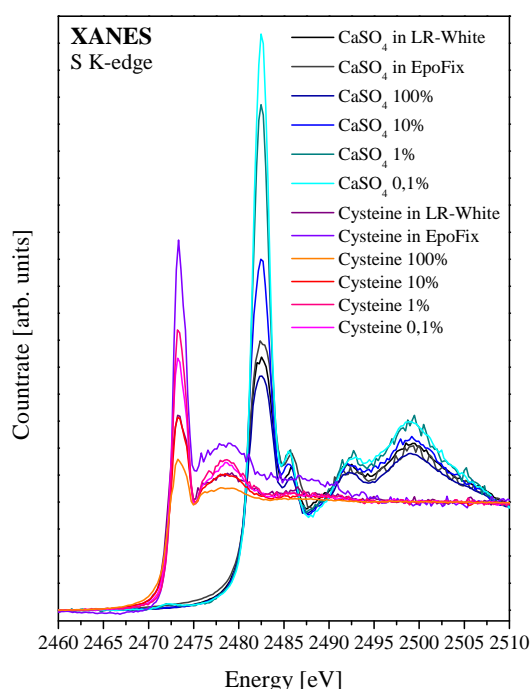
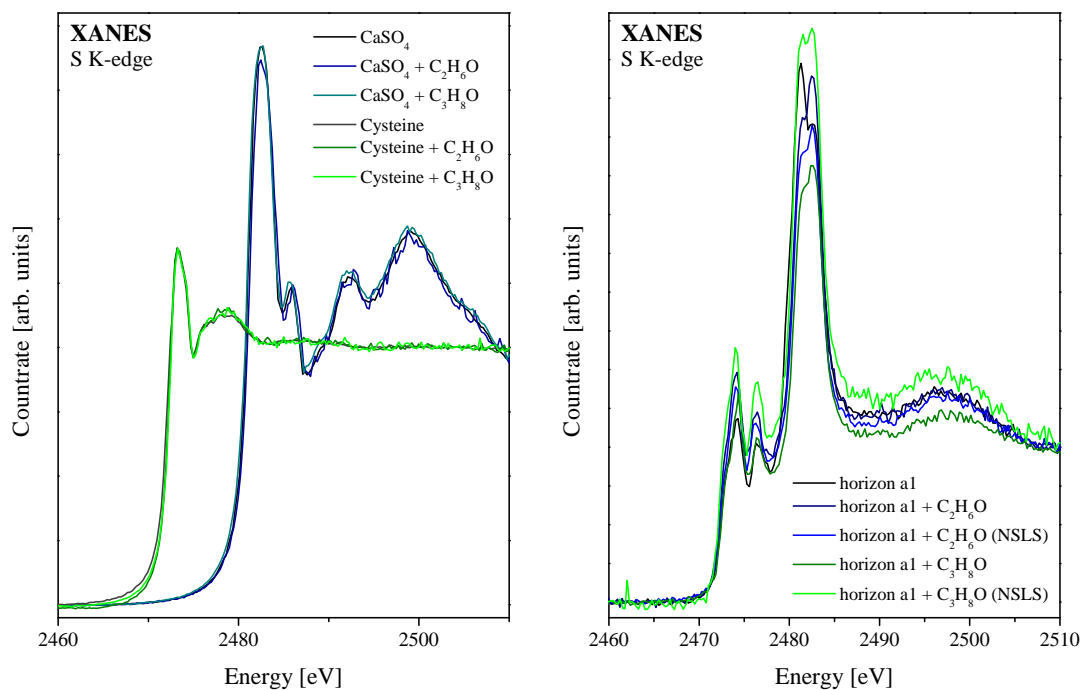
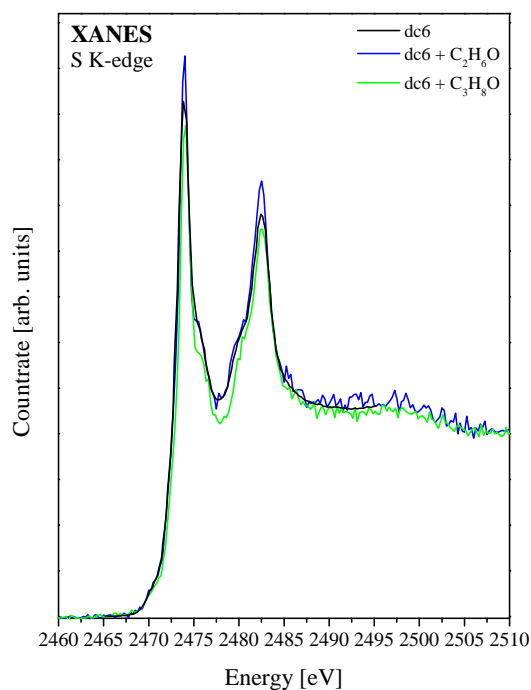


Figure 4.3.: Sulfur XANES spectra of sulfide (Cysteine) and sulfate (CaSO_4) standard embedded in LR-White and EpoFix, respectively; pure standards in different concentration for comparison; spectra taken at KMC-1, BESSY II.



(a) Standards in different solvents

(b) Horizon a1 in different solvents



(c) Sample dc6 in different solvents

Figure 4.4.: Sulfur XANES spectra of sulfide (Cysteine) and sulfate (CaSO_4) standards as well as a soil horizon and a debris component, previously wetted in different solvents; spectra taken at beamline KMC-1 at BESSY II; two of the soil spectra taken at beamline X15B at NSLS.

Since the embedding methods require dilution with isopropanol (C_3H_8O) or dehydration by ethanol (C_2H_6O), a possible impact of these chemicals on the soil samples was also analyzed. For analysis, the two standards Cysteine and $CaSO_4$, the coal dc6, and soil horizon a1 were chosen. Prior to measurements, the samples were wetted in either of the solvents and dried again. The results are shown in figure 4.4. For comparison, untreated sample spectra are added. Obviously, no changes in sulfur oxidation state or other spectral features occur due to the used solvents. Deviations in the horizon spectra are caused by inherent sample heterogeneities. Finally, LR-White was chosen for all further spectromicroscopy experiments, simply due to convenience of the preparation process. A detailed description of the process is given in the appendix.

4.1.2. Soils

4.1.2.1. Soil sample spread on tape

The investigated soil sample shown in this section was taken from the Schulgarten profile, i.e. from horizon H3. The sample was taken under ambient conditions, dried and then spread on Kapton tape. The experiments were conducted at beamlines 2-ID-B and 2-ID-E at the APS. All spectra and element specific images were acquired in fluorescence mode under helium flow or helium atmosphere, respectively. Regions of interest, that is regions and particles of elevated sulfur concentration, were chosen by VLM and fluorescence fly scans. Fluorescence images at beamline 2-ID-B were taken with an incident x-ray energy of 2490 eV, slightly above the sulfate peak energy. This allows the detection of Sodium, Magnesium, Aluminum, Silicon, Phosphorus and Sulfur. Energy calibration was performed with pure $CaSO_4$, its white line peak was set to 2482.5 eV. At characteristic spots on the sample, sulfur K-edge XANES spectra were taken in the energy range of 2460 to 2520 eV with a step size of 0.25 eV and a dwell time of 5 s. All spectra are normalized and processed as described in the previous chapter. Vertical lines in the spectra indicate averaged peak positions of the specific sulfur species. Fluorescence images at beamline 2-ID-E were taken with an incident x-ray energy of 10 keV, allowing the (additional) detection of the important soil and debris elements Calcium and Iron, as well as a variety of possible trace elements. Detector energy calibration was done with NIST standards.

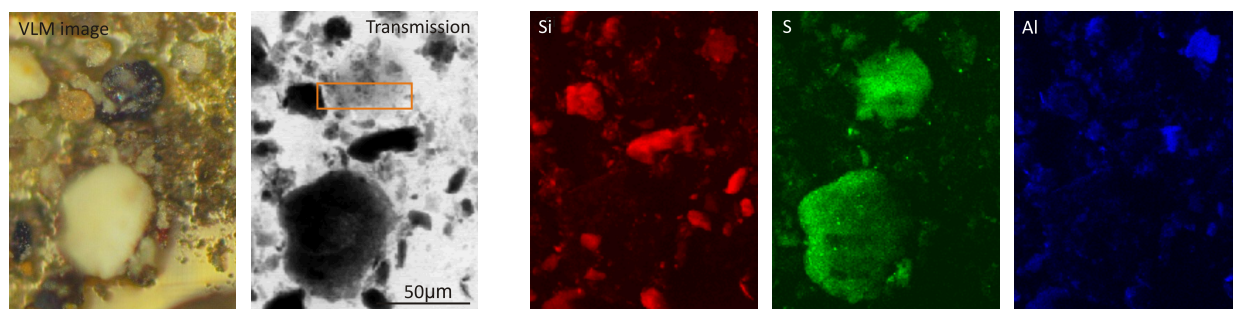


Figure 4.5.: Images of a region of interest by visible light microscopy, soft x-ray microscopy in transmission mode and elemental maps of Si (red), S (green), and Al (blue). X-ray images of $150 \times 180 \text{ pxl}^2$, $0.75 \mu\text{m}$ step size and 0.2 s dwell time per pxl. The box in the transmission image indicates the region studied in more detail in figure 4.9.

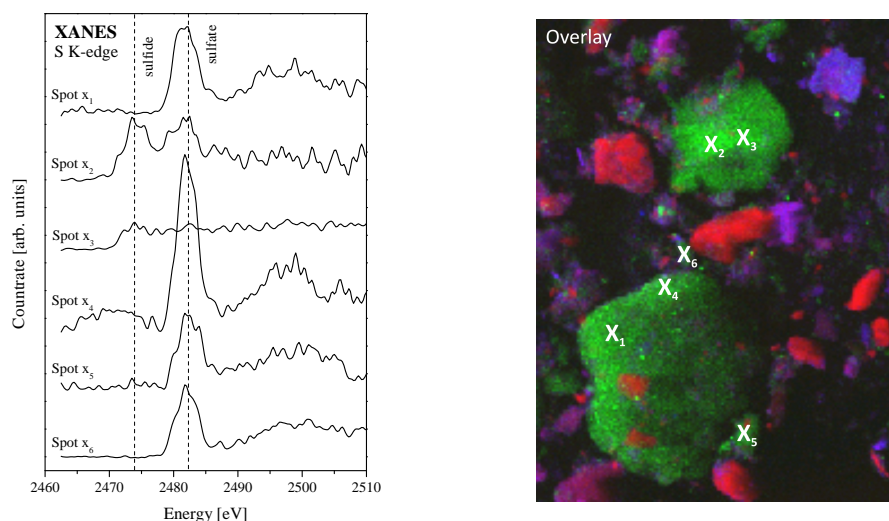


Figure 4.6.: **Right:** Overlay of the elemental maps of Si (red), S (green), and Al (blue) of figure 4.5. **Left:** S XANES spectra taken at different spots as indicated in the overlay with 0.25 eV step size and 5 s dwell time.

Element specific fluorescence images of the chosen region on the sample are shown in figures 4.5 and 4.7, along with a VLM and a transmission image of the same region. The important soil and debris elements Al, Si, S, Ca, and Fe are depicted. Comparing the maps of the different elements, no general correlation can be observed, but several structures are colocalized for different elements and can therefore be ascribed to different soil constituents or debris components. Sulfur K-edge XANES spectra were taken at different spots on the sample, as illustrated in figure 4.6. The overlay as well as the pure sulfur map reveal two particles of elevated sulfur concentration, which considerably differ in thickness and density, as can be concluded from the VLM and transmission images. The lower particle shows a strong and exclusive colocalization of S and Ca, as can be seen in figure 4.7. The spectra taken of this particle reveal pure sulfates. Therefore it can be concluded, that the particle is mainly comprised of CaSO_4 , probably originating from gypsum or stucco.

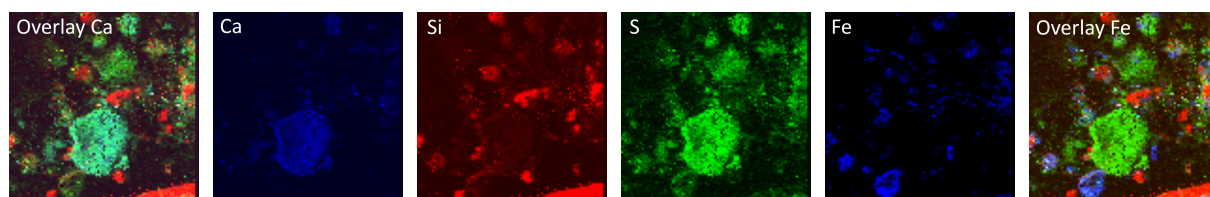


Figure 4.7.: Elemental maps of from left to right: overlay of the elemental maps of Si (red), S (green) and Ca (blue), elemental maps of Ca (blue), Si (red), S (green), Fe (blue), overlay of the elemental maps of Si (red), S (green), and Fe (blue). Hard x-ray fluorescence images of $200 \times 200 \text{ pxl}^2$, $2 \mu\text{m}$ step size and 0.04 s dwell time per pxl.

The smaller particle in the upper half of the images is of more versatile composition, as can be concluded from the elemental maps but also from the spectra shown in figure 4.6. Spot 2 shows a mixture of different sulfur oxidation states, while spot 3 seems to be pure sulfide. This particle

was further analyzed in detail. A new region of interest was chosen, indicated as an orange box in the transmission image. Elemental maps and overlays as well as additional spectra taken of this particle are shown in figures 4.8 and 4.9. This particle is very heterogeneous in composition, sulfur speciation and density. Within this particle, very distinct spots enriched in Al, Si, Ca, and Fe are observed. The same is true for some trace elements: K, Mn, and Zn, while the left half of the particle is also significantly enriched in Cu (images of these elements are not shown). This heterogeneity is also reflected in the spectra. Spots of apparently pure sulfides are located in close proximity to spots of mixed sulfur speciation with varying ratios of the abundant species. These observations may be explained by an accumulation of slags, pyrolyzed material, debris particles, and soil constituents. Especially the strong accumulation of different metals strongly suggests the predominance of slags.

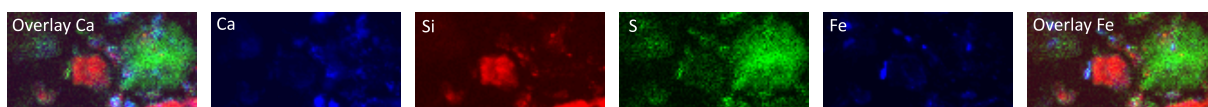


Figure 4.8.: Magnified upper (smaller) debris particle: Elemental maps from left to right: overlay of the elemental maps of Si (red), S (green) and Ca (blue), elemental maps of Ca (blue), Si (red), S (green), Fe (blue), overlay of the elemental maps of Si (red), S (green), and Fe (blue). Hard x-ray fluorescence images of $104 \times 55 \text{ pxl}^2$, $1 \mu\text{m}$ step size and 0.3 s dwell time per pxl.

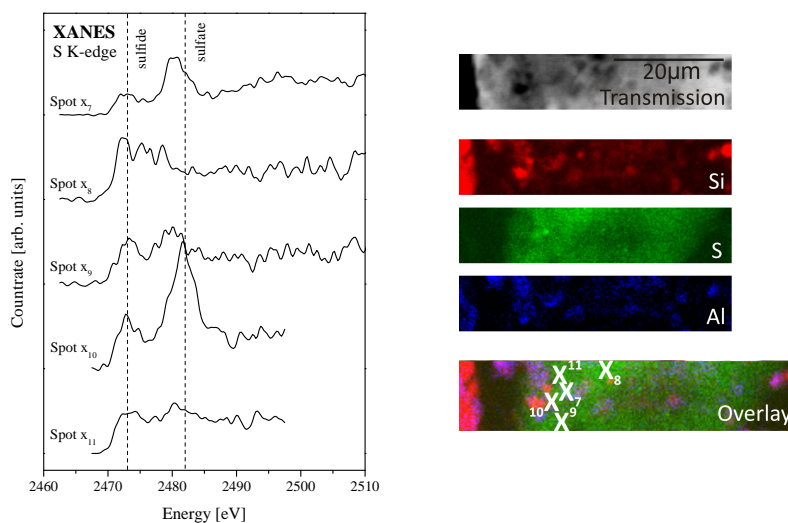


Figure 4.9.: **Right:** Images of the same region of interest (magnified area of Fig. 4.5) by soft x-ray microscopy in transmission mode and elemental maps of Si (red), S (green), and Al (blue), overlay of the elemental maps of Si (red), S (green), and Al (blue). X-ray images of $200 \times 40 \text{ pxl}^2$, $0.25 \mu\text{m}$ step size and 0.2 s dwell time per pxl. **Left:** S XANES spectra taken at different spots as indicated in the overlay with a step size of 0.25 eV and a dwell time of 5 s.

Reconsidering the elemental maps and overlays of figures 4.5 to 4.9, several additional information can be extracted. Obviously, deep green areas represent high sulfur concentration and

therefore most probably debris particles. Slight green areas may represent smaller debris particles, debris particles of lower sulfur concentration, organic soil constituents, or soil minerals. Turquoise regions were only observed in the Ca overlay, representing CaSO_4 , as described above. Red regions within the sample indicate pure Si and therefore quartz particles. Violet regions are exclusively observed in the Al overlay and show a colocalization of Si and Al, most likely representing clays, in terms of aluminosilicates. This interpretation is strengthened by elemental maps of Na and Mg, which are typical interlayer cations and are enriched in the same regions. The maps are not shown. Blue regions only appear in the Fe overlay and possibly represent slags, especially if they are colocalized with other metals. A colocalization of only S and Fe, however, most likely represents soil minerals, e.g. pyrite, which would be verifiable by sulfur XANES spectra.

The used sample preparation method, i.e. to simply spread the soil on tape, inherits a distinct disadvantage. It is difficult or maybe even impossible to directly observe the interface of debris particles and surrounding soil. Furthermore, gradients within debris particles are difficult to observe, as the surface is always contributing to the spectra. Therefore, thin sections of embedded samples taken with soil sample rings were made. Two examples are given in the following sections.

4.1.2.2. Soil sample in Kallocryl

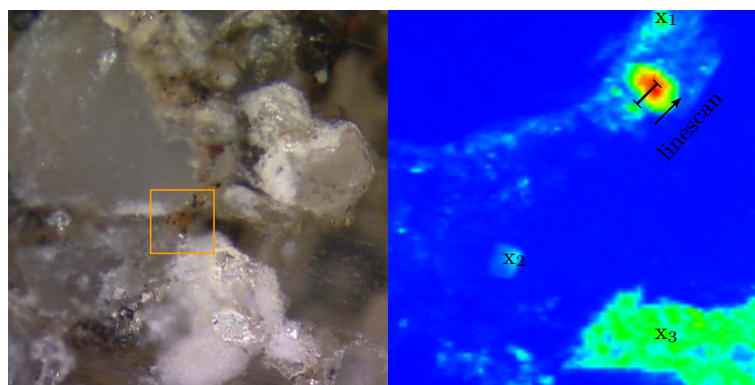


Figure 4.10.: Image of one region of interest taken by VLM and elemental map of sulfur of that region marked by an orange box in the VLM image. X-ray fluorescence image of $100 \times 100 \text{ pxl}^2$, $1 \mu\text{m}$ step size and 0.3s dwell time per pxl. Incident beam energy 2500 eV. Positions of measured sulfur K-edge XANES spectra are given in the sulfur map.

The investigated soil sample shown in this section was taken from horizon H2 of the Schulgarten profile. It was taken under ambient conditions with a soil sample ring, dried, and embedded in Kallocryl. Afterward, it was cut into thin sections using an inside hole saw. The experiments were conducted at beamline ID21 at ESRF. All images and spectra were acquired under vacuum. Prior to the experiments, possible regions of interest were chosen by VLM. These regions can be found again by a VLM mounted in the sample chamber and evaluated by means of sulfur content, respectively possible debris particles, by fluorescence fly scans. Structures seen by VLM can especially be found again in the Silicon maps. Generally, the incident x-ray energy

was set to 2500 eV, well above the sulfate peak energy. This yields elemental maps of Al, Si, and S. Unfortunately, the acquisition of Ca and Fe maps is not possible parallel to sulfur XANES measurements. Energy calibration was performed with pure CaSO_4 , its white line peak was set to 2482.5 eV. Figure 4.10 shows a chosen region of interest. The region of the sulfur fluorescence map on the right is marked by an orange box in the VLM image on the left. The region was chosen because it seemed to comprise a small reddish debris particle, surrounded by soil material at the boundary of a rather big quartz grain. The obtained sulfur map shows a small particle significantly enriched in sulfur, as well as several regions and even smaller spots of moderate sulfur concentration. Sulfur K-edge XANES spectra were taken at different spots on the sample as well as along a line, marked in the sulfur map in figure 4.10. The spectra are shown in figure 4.13. The course of the linescan is indicated by arrows in each of the figures. The spectra were measured over an energy range of 2460 to 2530 eV, to cover an appropriate normalization range for all sulfur species (in the diagrams only the range from 2460 to 2510 eV is printed for better visibility of the spectral features). The spectra were taken with a step size of 0.25 eV and a dwell time of 1 s. Each spectrum is repeated 10 times and then averaged.

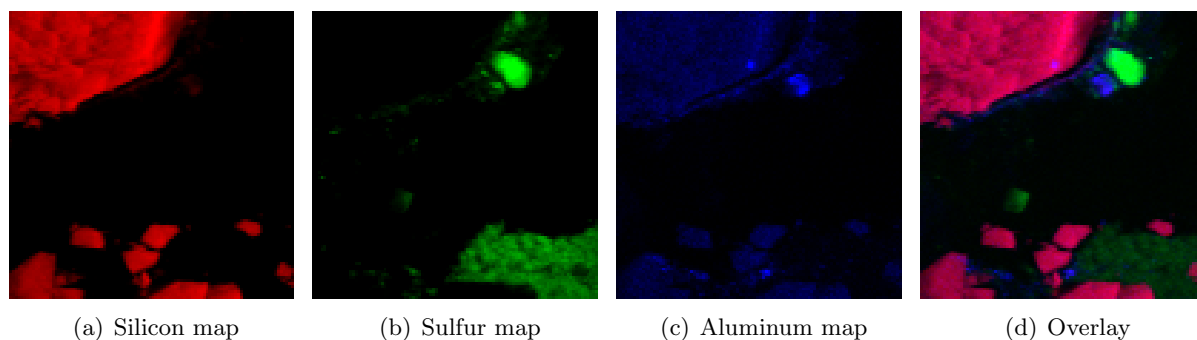


Figure 4.11.: Elemental maps of Si, S, Al, and corresponding overlay. X-ray fluorescence images of $100 \times 100 \text{ pxl}^2$, $1 \mu\text{m}$ step size and 0.3 s dwell time per pxl. Incident beam energy 2500 eV.

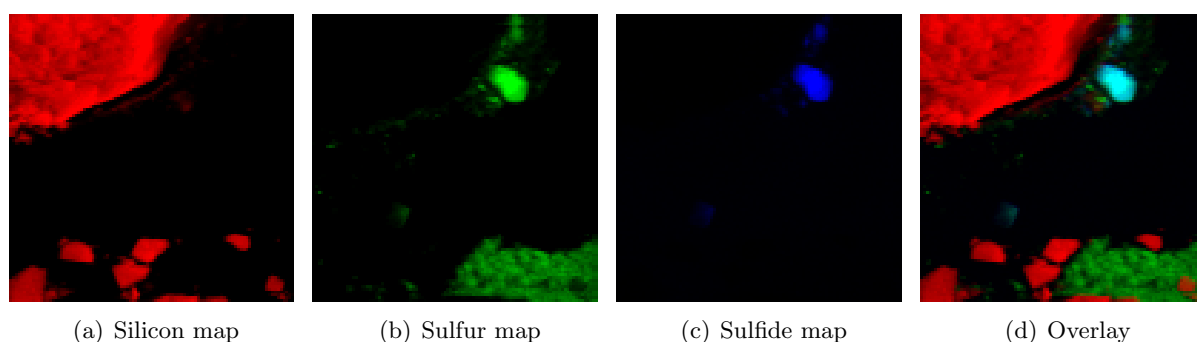


Figure 4.12.: Elemental map of Si, chemical maps of sulfate (total sulfur) and sulfide, and corresponding overlay. X-ray fluorescence images of $100 \times 100 \text{ pxl}^2$, $1 \mu\text{m}$ step size and 0.3 s dwell time per pxl. Incident beam energy 2483 eV and 2474 eV, respectively.

Figure 4.11 shows the elemental maps of Si, S, and Al as well as the corresponding overlay of the chosen region of interest, cp. figure 4.10. Si and S do not show any colocalization, while Al is colocalized with Si, in some regions with S, and in other regions it occurs separately. The colocalization of Al and Si is easily explained by clays, as described in the previous section. Quartz particles in soils are often covered by clays, which seems to be true for all quartz particles in this region of interest. The colocalization of Al and S is explained by two mechanisms. It is well known, that in acidic soils of humid regions, Al released from clay minerals forms aluminum-hydroxyde-sulfates, such as Alunite and Jurbanite. Additionally, Al is enriched in humic matter, which also contains sulfides, e.g. Cysteine and Methionine. On the other hand, pure Al containing compounds, e.g. Aluminum-hydroxides, such as Gibbsite, generally abundant in soils, are represented by the blue areas in the overlay. The big quartz particle in the upper half of the images nicely shows coating by such compounds.

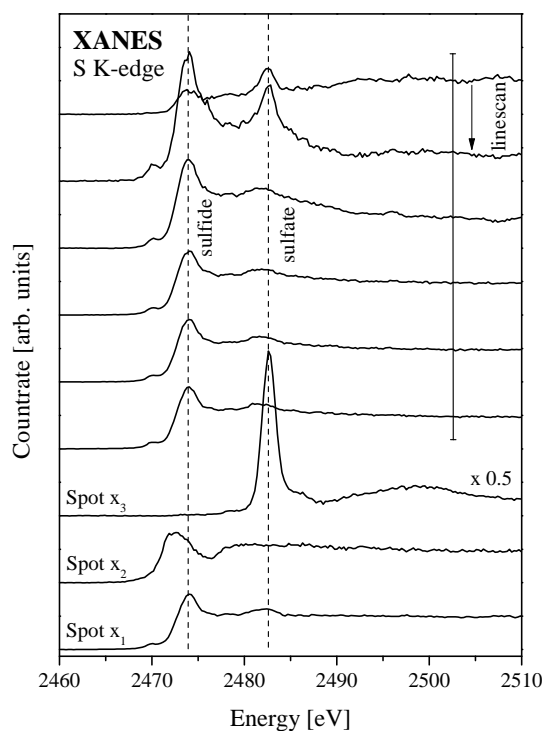


Figure 4.13.: Sulfur K-edge XANES spectra taken at different spots as indicated in figure 4.10 with 0.25 eV step size and 1 s dwell time (each spectrum repeated 10 times and averaged). Spectrum of spot 3 is divided by two.

Additional maps were measured using other incident x-ray energies to achieve a separation of different sulfur species. Fluorescence maps were recorded at 2474 eV, yielding only contributions of sulfides in the sulfur map and at 2483 eV, very close to the sulfate peak, yielding total sulfur. This process is generally referred to as chemical mapping. In principle, the already measured map at 2500 eV could also be used for total sulfur, but the change in energy also changes the focus of the x-ray beam and therefore the imaged region shifts. The higher the energy difference, the bigger is this shift. As the goal is to create an overlay of the different sulfur maps, the shift is

desired to be as small as possible. The remaining shift can then be corrected using the Si maps. One dataset is shifted with respect to the other one until both Si maps are congruent. The result is shown in figure 4.12: fluorescence maps of Si, total S and sulfidic S, as well as the corresponding overlay. In this overlay, green regions represent pure sulfates, while turquoise regions represent either sulfides or mixed oxidation states, depending on the blue content. Therefore, spots 1 and 2, marked in figure 4.10, are supposed to consist of sulfides, while spot 3 consists of pure sulfates. This assumption is approved in the measured spectra, displayed in figure 4.13. The spectra clearly show pure sulfate for spot 3 and pure inorganic sulfide, i.e. Pyrite, for spot 2. Spot 1 is of the same composition as the bigger particle, along which a linescan was measured. The linescan shows a rather homogeneous particle comprising mainly organic sulfides and little sulfates, as well as a small amount of inorganic sulfides at very low energy, i.e. Pyrrhotite. This may indicate the association of inorganic (iron)sulfidic slags to the organic matter. Sulfates are presumably enriched at the surface, because the sulfate content rises when approaching the particle boundaries. This indicates oxidation of the particle.

During the same beamtime, the sulfur content of the used resin, Kallocryl, was tested and found to be considerable. The characteristic spectrum is depicted in figure 4.2(a). However, contributions of Kallocryl could not be observed in the measured sample spectra.

4.1.2.3. Soil sample in LR-White

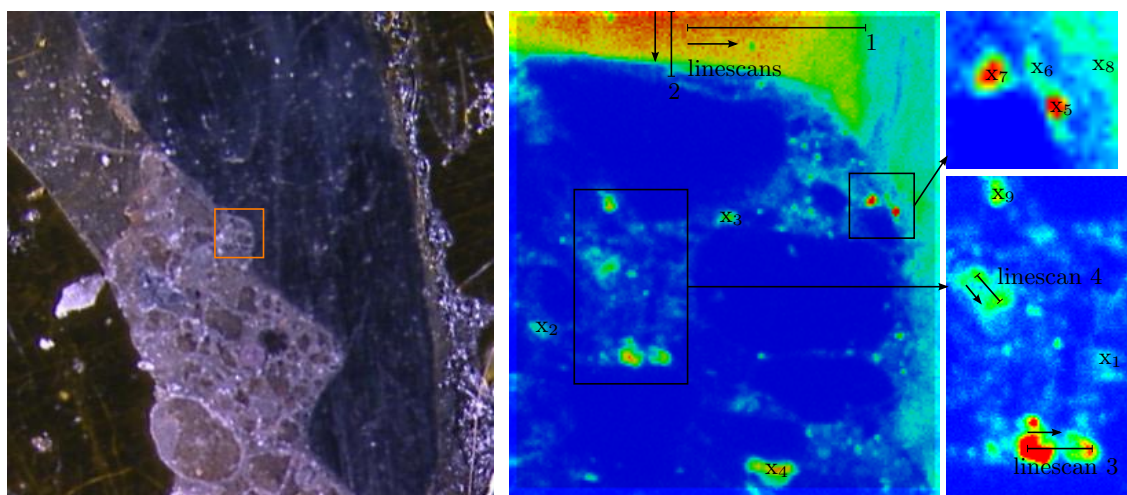


Figure 4.14.: Image of one region of interest taken by VLM and elemental map of sulfur of that region marked by an orange box in the VLM image. X-ray fluorescence image of $170 \times 190 \text{ pxl}^2$, $1 \mu\text{m}$ step size and 0.1 s dwell time per pxl . Two zooms into regions enriched in sulfur as marked in the big sulfur map: sulfur maps of $25 \times 20 \text{ pxl}^2$, $1 \mu\text{m}$ step size and 0.1 s dwell time per pxl and $90 \times 150 \text{ pxl}^2$, $0.5 \mu\text{m}$ step size and 0.1 s dwell time per pxl . Incident beam energy 2500 eV . Positions of measured sulfur K-edge XANES spectra are given in the sulfur maps.

The investigated soil sample shown in this section was taken from horizon H4 of the Schulgarten profile. The soil sample was taken under ambient conditions with a soil sample ring, dried, and embedded into LR-White. Then, it was cut into thin sections using an inside hole saw. These

sections were further thinned by grinding. The spectromicroscopy experiments were performed at beamline ID21 at the ESRF. Therefore, all images and spectra were acquired under vacuum. Regions of interest were chosen by VLM and refined by fluorescence fly scans, as described in the previous section.

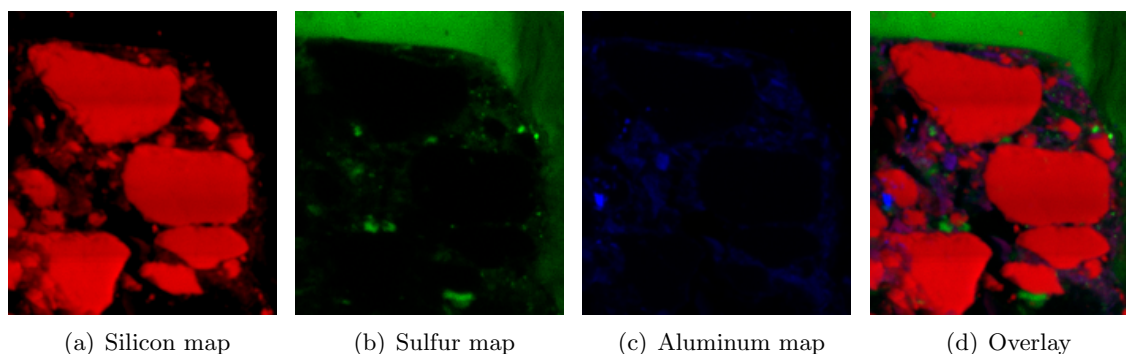


Figure 4.15.: Elemental maps of Si, S, Al, and corresponding overlay. X-ray fluorescence images of 170×190 pxl², $1\mu\text{m}$ step size and 0.1 s dwell time per pxl. Incident beam energy 2500 eV.

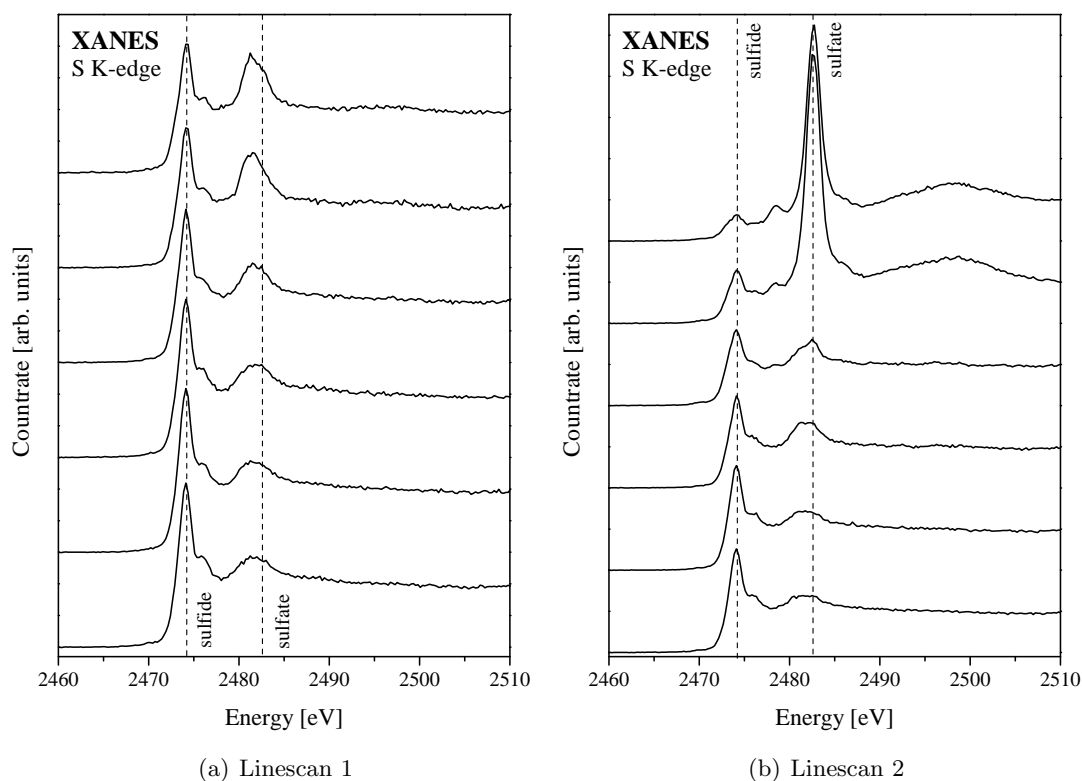


Figure 4.16.: Sulfur K-edge XANES spectra taken along different lines as indicated in figure 4.14 with 0.25 eV step size and 1 s dwell time (each spectrum repeated 10 times and averaged).

Figure 4.14 shows a VLM image of the sample. The chosen region of interest is marked by an orange box. Additionally, the sulfur map of the chosen region is depicted, as well as sulfur maps of two zooms into this region, marked by black boxes. Several spots and lines are added, indicating the positions on the sample, where sulfur K-edge XANES spectra were taken. The chosen parameters are identical to those elucidated in the previous section. These spectra are displayed in figures 4.16 to 4.19. The measured region was chosen because it comprises the interface of a rather big debris particle, which is enriched in sulfur, and adjacent soil material.

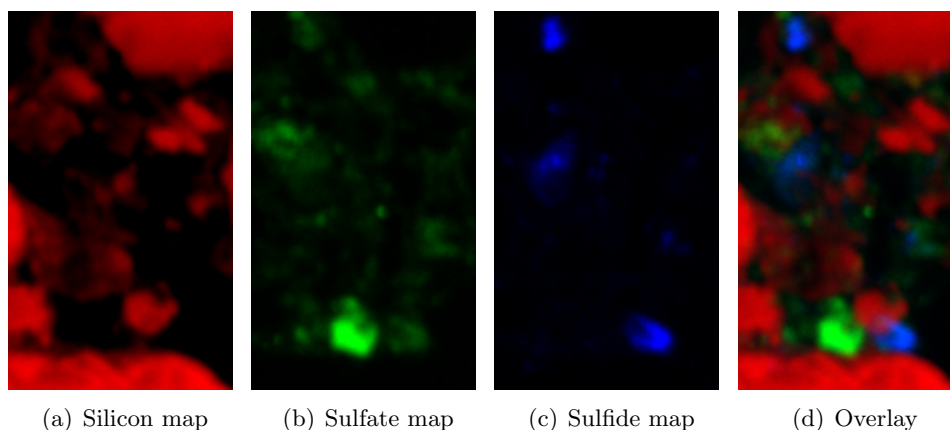


Figure 4.17.: Elemental map of Si, chemical maps of sulfate (total sulfur) and sulfide, and corresponding overlay. X-ray fluorescence images of 90×150 pxl², $0.5\mu\text{m}$ step size and 0.1 s dwell time per pxl. Incident beam energy 2483 eV and 2474 eV, respectively.

Figure 4.15 shows the elemental maps of Si, S, and Al, as well as the corresponding overlay of the measured region. Several features are easily assignable to typical soil and debris constituents: quartz grains of different sizes (red), clays (violet), and the big debris particle (green). Smaller green particles may be smaller debris particles or soil minerals and blurry green regions humic matter. Blue spots are presumably Aluminum-hydroxides, generally abundant in soils.

Sulfur K-edge XANES linescans through the big debris particle, as indicated in figure 4.14, are shown in figure 4.16. Linescan 1 horizontally runs through the debris particle from high to lower concentrated regions. The corresponding spectra in figure 4.16(a) run from bottom to top of the diagram. Linescan 2 vertically runs through the particle, from the bulk region to the interface of particle and soil. The corresponding spectra in figure 4.16(b) run from bottom to top of the diagram. Comparing the bulk spectra with those of other debris components shown in section 3.4, the debris particle is most certainly pyrolyzed material or a coal particle. The spectra show a sharp organic sulfide peak at 2474.1 eV with a shoulder in the sulfoxide energy range and a post-edge feature in the sulfonate to sulfate energy range. In linescan 1, the sulfide content diminishes when moving to the lower concentrated region, while a peak arises in the sulfonate energy range. This clearly indicates the intrinsic oxidation of the obviously heterogeneous particle. The occurring organic sulfides are oxidized to sulfonates, possibly ester sulfates. In linescan 2, the sulfide content diminishes when moving to the interface, while a strong sulfate peak arises together with a small peak in the sulfite energy region. The changeover at the interface is very abrupt. However, this linescan clearly shows oxidation at the interface of

the debris particle, sulfite being an intermediate state of the full oxidation to sulfate.

Figure 4.17 shows chemical mapping of the bigger one of the two magnifications shown in figure 4.14. Chemical mapping is achieved in the same way as explained in the previous section. Displayed are x-ray fluorescence maps of Si, total S, sulfidic S, and the corresponding overlay. In this overlay, green regions represent pure sulfates, while blue regions indicate elevated sulfide ratios. In this map, two additional linescans were measured, as marked in figure 4.14. The corresponding spectra are shown in figure 4.18. The course of the linescans is indicated by arrows in the sulfur map. The corresponding spectra run from bottom to top of each of the diagrams. Linescan 3 therefore starts on the sulfate particle and moves into the area enriched in sulfides, presumably soil material. As expected, the sulfate content rises when moving to the center of the particle and diminishes approaching the boundaries. Moving further into the adjacent soil material, the sulfate content further diminishes. Linescan 4 starts in the sulfate region and moves into a region with elevated sulfide content. While the sulfate area clearly consists of CaSO_4 , recognizable by its post-edge features, cp. section 3.2, the sulfidic region seems to be of similar composition as the big debris particle measured in linescans 1 and 2. The uppermost spectrum in figure 4.18(b) shows the typical sulfide and sulfonate peak, observed at the end of linescan 1, as well as the sulfite peak observed in linescan 2. Therefore, this spot may represent a smaller particle of the same origin, which is not fully oxidized.

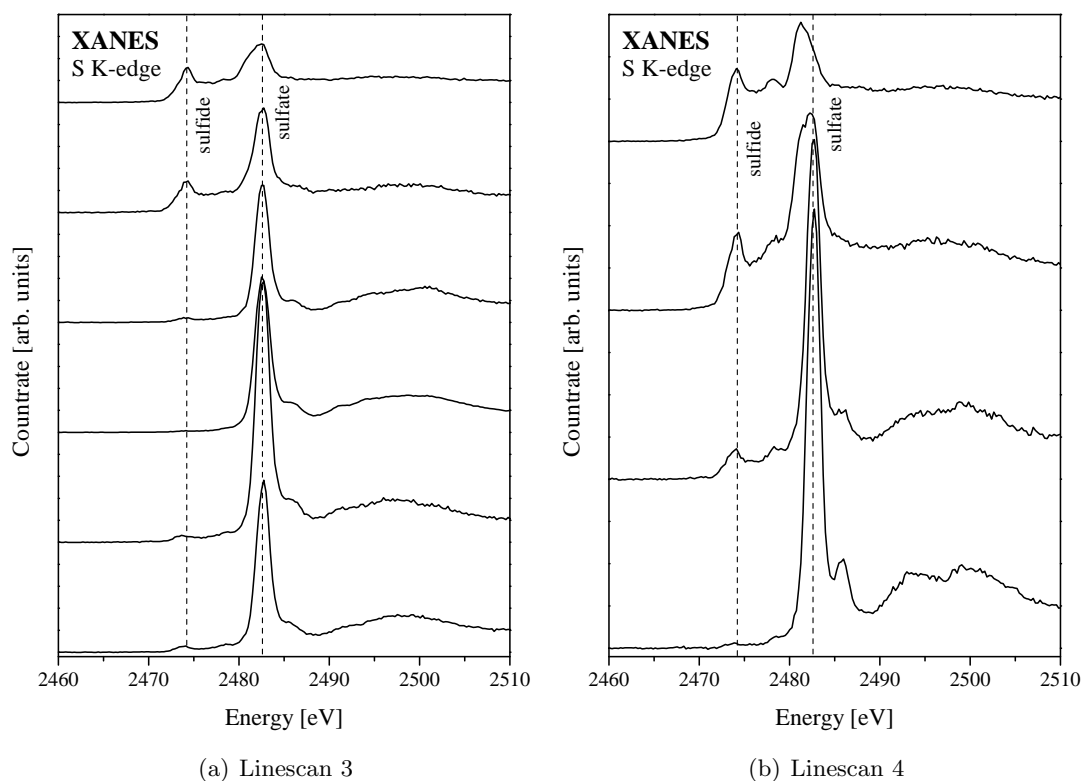


Figure 4.18.: Sulfur K-edge XANES spectra taken along different lines as indicated in figure 4.14 with 0.25 eV step size and 1 s dwell time (each spectrum repeated 10 times and averaged).

Figure 4.19 displays the sulfur XANES spectra of different spots as marked in figure 4.14. Obviously, the sulfur speciation within these spots is very heterogeneous, indicating versatile origin of the occurring particles and possibly different redox conditions. Spots 1 and 3 represent pure sulfates, while e.g. spots 6 and 7 show typical soil spectra. Spot 5 is somewhat special, as it shows a spectrum virtually identical to that of Pyrrhotite. This particle might therefore originate from inorganic sulfidic slag.

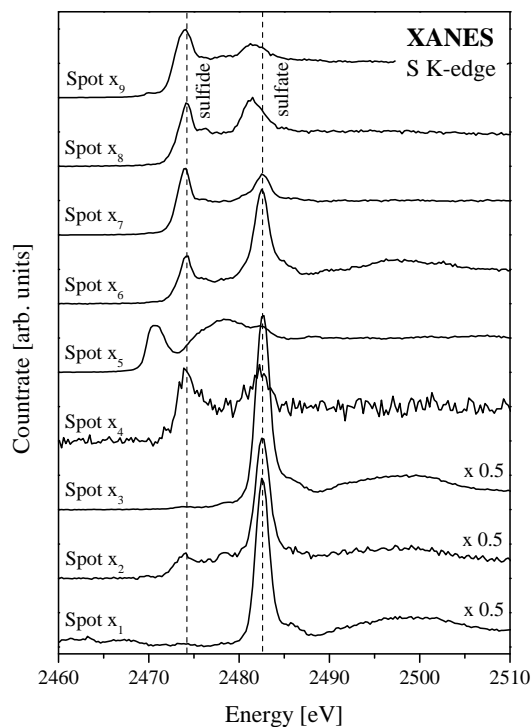


Figure 4.19.: Sulfur K-edge XANES spectra taken at different spots as indicated in figure 4.14 with 0.25 eV step size and 1 s dwell time (each spectrum repeated 10 times and averaged). Spectra of spots 1 to 3 are divided by 2.

4.1.3. Soil solution

In this section, the investigation of a sample of soil solution obtained from percolation experiments, cp. section 4.1, is shown. In this case, the irrigated column was packed with the fine earth fraction of horizon g5. A droplet of the solution was sealed between two 200 nm thick silicon nitride windows without further treatment. Experiments were conducted at ID21 at the ESRF. Therefore, all images and spectra were taken under vacuum. However, the sealed soil solution did not exsiccate during the experiments. Possible regions of interest were chosen by VLM, found again using the VLM mounted at the beamline and assessed by fluorescence fly scans. A sulfur fluorescence image as well as two VLM images of the chosen region of interest are depicted in figure 4.20. Elemental maps of Si, S and, Al as well as the corresponding overlay of this region are shown in figure 4.21. In essence, two particles of similar size are observed, one comprising S and Al and the other one comprising Si and Al. The interpretation is identical to the one given in section 4.1.2.2. The particle in the lower right corner is most likely a quartz particle covered by clays (or a clay particle). The particle in the middle is presumably a debris particle with accumulated Aluminum-hydroxyde-sulfates. Additionally, three very small sulfuric particles can be observed in figure 4.20. All particles are embedded in humic substance which is only visible in the VLM images.

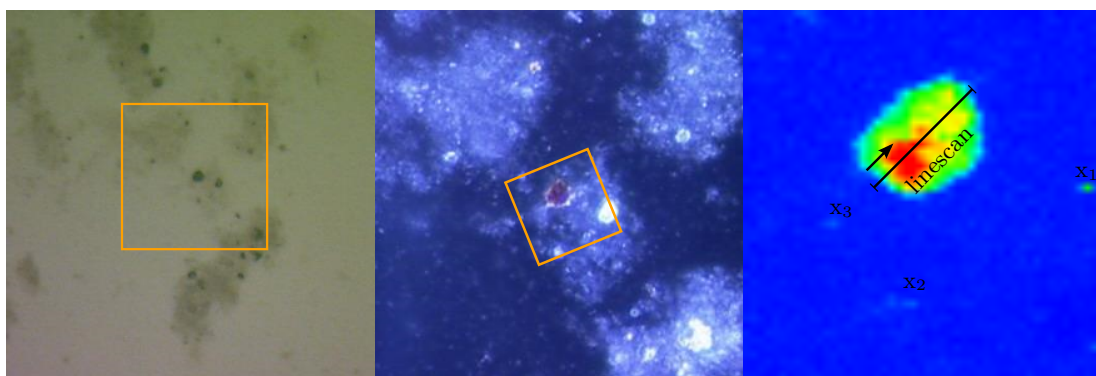


Figure 4.20.: Images of one region of interest taken by VLM and elemental map of sulfur of that region. Orange boxes each mark the area of the respective image to the right. X-ray fluorescence image of $50 \times 50 \text{ pxl}^2$, $1 \mu\text{m}$ step size and 0.3s dwell time per pxl. Positions of measured sulfur K-edge XANES spectra are given in the sulfur map.

Sulfur K-edge XANES spectra were acquired at the small sulfur spots, indicated by x1 to x3, as well as along a linescan across the big debris particle as marked in figure 4.20. Measuring parameters are identical to those described in section 4.1.2.2. The measured spectra are displayed in figure 4.22. The linescan clearly shows a sulfidic particle that is oxidized at the surface. The bulk spectra are very similar to coal spectra shown in section 3.4 and the particle is therefore supposed to consist of pyrolyzed or coalified material. The small sulfate peak visible in all spectra is due to contributions of the surface. Moving along the linescan to the boundaries and therefore to the surface of the particle, clear gradients are visible. The sulfide content diminishes while the sulfate content rises. The surface comprises almost pure sulfates. This is also where the Aluminum-hydroxyde-sulfates might be accumulated. The three additional spectra measured at the small sulfur spots are identical to those obtained at the surface of the big particle. Therefore,

the small spots are supposed to be smaller particles of the same origin that are also exposed to oxidation.

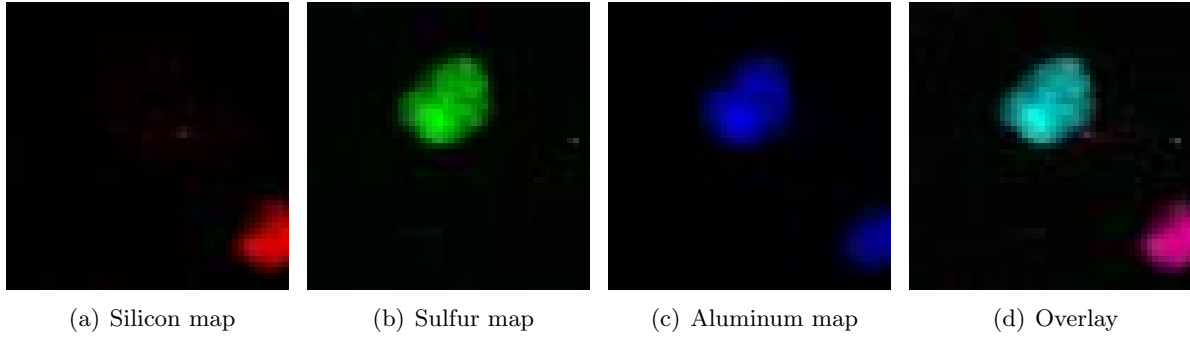


Figure 4.21.: Elemental maps of Si, S, Al, and corresponding overlay. X-ray fluorescence images of $50 \times 50 \text{ pxl}^2$, $1 \mu\text{m}$ step size and 0.3 s dwell time per pxl. Incident beam energy 2500 eV.

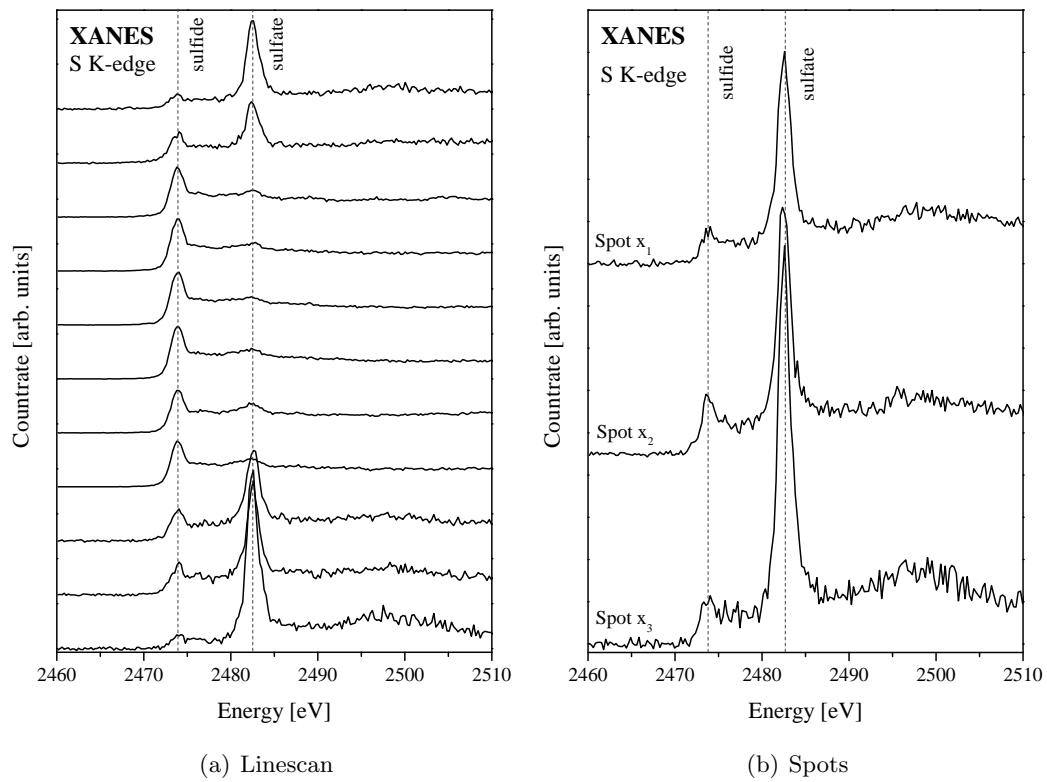


Figure 4.22.: Sulfur K-edge XANES spectra taken along different lines as indicated in figure 4.14 with 0.25 eV step size and 1 s dwell time (each spectrum repeated 10 times and averaged).

5. Conclusion

5.1. Spectroscopy experiments

Sulfur K-edge XANES spectra of a series of soil profiles along the slope of the biggest dump of WWII rubble in Berlin, the so-called Teufelsberg, as well as a variety of dumped building rubble and war debris components found in these profiles were measured and analyzed. The spectra of the different soil profiles (figures 3.14 to 3.15) show a rather general behavior, dependent on the soil type but independent from the position along the hill. In each Pararendzina profile, the sulfate content rises from top to bottom, while the sulfide as well as the sulfonate contents diminish. This trend can be explained by the diminishing humus content from top to bottom of each profile and further characteristics of these soils. All profiles are well aerated from top to bottom, the ground water still being much deeper than the deepest analyzed horizon. Therefore, no reducing but rather oxidizing conditions prevail in all horizons. These findings are, however, different to those made on other soil types on hillsides. In 2006, Thieme et al. [69] performed sulfur speciation on soils in a hillside forest and observed significant changes in sulfur speciation, dependent on the profile depth but also on the position along the hillside, representing a hydrological gradient. No such gradient is found at the Teufelsberg.

Furthermore, the different occurring soil types can be recognized by their spectroscopic profile. For Pararendzina, organic sulfur forms, i.e. sulfide and sulfonate diminish from top to bottom while the sulfate content rises. For Kolluvisol, the enrichment with humic matter in each horizon as well as the mutual independence of the horizons is clearly visible in the spectra. The horizons show elevated sulfide and sulfonate contents without any observable gradient or pattern. Even the transition from Kolluvisol to underlying Pararendzina is discernible in the spectra.

The analysis of a variety of debris components revealed that their sulfur load comprises mainly sulfates (figure 3.11).

Special attention was paid on sample preparation methods, which were evaluated in detail. Neither drying nor grinding of the soil samples induces changes in the sulfur oxidation states (figures 3.13 to 3.13). Moreover, the overall sulfur pool of a soil horizon can be analyzed only using the fine earth fraction, it is not necessary to separately prepare and admix the soil skeleton, see figures 3.13 to 3.13 and 3.14 to 3.15.

The acquired spectra were analyzed using three different methods: peak fitting, principle component analysis (PCA), and linear combination fitting (LCF). For peak fitting, no prior knowledge of the sample or its composition is necessary. The occurring peaks are simply fitted by several Gaussians, that are afterward attributed to different sulfur oxidation states on the basis of their energy position. The different absorption edges are accounted for by two arctangent functions, one for the reduced sulfur species, positioned right behind the second sulfide peak and the second one representing the sum of all oxidized species, positioned behind the sulfate peak. The ratios of the different species can then be calculated using the areas of the fitted Gaussians.

For PCA, prior knowledge of the samples, their composition or speciation is also not necessary.

This method yields the minimal number of different compounds occurring in a given set of samples, that are in some way related. PCA was performed on two datasets, measured at different beamlines and covering different energy ranges. For the first dataset, SLRI (Synchrotron Light Research Institute, Thailand) data measured over a very narrow energy range, a minimal number of six components was obtained, in accordance to the fitted different oxidation states in peak fitting analysis of the same dataset. The second dataset, measured at BESSY (Berliner Elektronenspeicherring-Gesellschaft f'ur Synchrotronstrahlung, Germany) II over an extended energy range that covers the whole normalization range of all sulfur species and therefore also the sulfate post-edge features (post-edge features of lower oxidation states are superimposed by white line peaks of other species), a minimal number of eight components was obtained. This enhanced value is most certainly due to post-edge features that are not included in the first dataset. With target transformation, the probability that a specific standard is a real compound within the analyzed spectra can be evaluated. Therefore, a database of various standard spectra is necessary. Especially when considering a dataset that includes compounds of very heterogeneous origin and composition, such as urban soils and war debris, the database needs to be extensive. In this work, the database seems not to be appropriate, as only several sulfates and a few sulfides yielded good results in target transformation. For other oxidation states, appropriate standards seem to be missing. However, PCA definitely shows the appropriate concentration, if a standard is measured in fluorescence mode.

LCF was applied to the SLRI dataset, previously analyzed by peak fitting and PCA. It was tried to make use of the PCA results in using those standard spectra in LCF that yielded the best results in PCA. This practice was previously reported to significantly shorten the LCF procedure [6]. However, this practice did not yield acceptable fits. Therefore, all sulfur standards within the database were allowed in LCF and acceptable fits were obtained (figures 3.44 to 3.49). Surprisingly, those standards that yielded the best results in PCA never occur in the LCF fits, although the occurrence of different standards is to some extent arbitrary and depends on the succession in which the standards are inserted into the fitting routine. This shows again, that the standard database does not seem to be appropriate or sufficient with respect to the analyzed dataset. However, when considering only the (summed) contributions of standards of different oxidation states, the LCF results are in accordance to those obtained in peak fitting. LCF could even confirm that the contribution of sulfone, assumed to be a fitting error during the peak fitting analysis, in fact results from pre- and post-edge features of compounds of other oxidation states. When only considering the goodness of fit, the LCF results are significantly worse than those obtained by peak fitting, cp. figure 3.16 and figures 3.47 to 3.49. LCF is crucially dependent on an appropriate standards database. Standards need to be measured in appropriate concentration and environment, which is very time-consuming, especially for pronounced heterogeneous samples comprising a huge variety of possible compounds. Obviously, noise in the data significantly complicates fitting.

For highly heterogeneous samples of urban soils, peak fitting is the best analysis method, with respect to goodness of fit, reproducibility, and time consumption. Errors induced by this method can be identified by considering sample characteristics, probabilities of the occurrence of different oxidation states and compounds, and suspect patterns. This can then be confirmed by LCF.

5.2. Spectromicroscopy experiments

Samples of soil aggregates, debris particles, and soil solution were analyzed by x-ray fluorescence imaging and subsequent sulfur K-edge XANES at specific spots on the samples. The samples originate from the same soils analyzed by pure (bulk) x-ray spectroscopy. Although ideal resins were found, sample preparation of soil aggregates and debris particles remained challenging because microtomes (standard for thin sections) could not be used due to the presence of quartz, stone, and possibly metal particles. The dicing procedure which was finally applied made use of a so-called "inside hole saw", which yields sections of minimally 30 μm , that need to be further thinned by grinding.

The studied samples show pronounced heterogeneity on small length scales in the micrometer range with respect to elemental distribution and especially to sulfur oxidation states and compounds. For example, pure pyrite particles without any oxidized ratio are found in close proximity to oxidizing sulfidic particles and pure sulfates. This implies heterogeneous environments, e.g. redox conditions, on these length scales.

The weathering of debris particles is clearly observed by means of oxidation gradients within the particles. Sulfidic particles are oxidized to sulfates at the particle's surface. However, oxidation also occurs within debris particles, due to and depending on their heterogeneous composition (figure 4.16(a)). The different geometric pathways also determine different chemical pathways. Additionally, different soil and debris constituents are discernible by the acquired elemental maps. Especially Ca and Fe maps are useful to identify and characterize anthropogenic material. Chemical mapping also proved to be useful to find regions of interest and understand the sample composition.

In summary, the applied methods allow for sulfur speciation with high precision and spatial resolution in urban soils with major anthropogenic influence. This contributes to the understanding of the chemical behavior of sulfur compounds in anthropogenically influenced soils not only phenomenologically but also in view of the underlying processes.

Bibliography

- [1] AGARWAL, B. *X-ray spectroscopy: an introduction*. Springer series in optical sciences. Springer-Verlag, 1991.
- [2] ALS-NIELSEN, J., AND MCMORROW, D. *Elements of Modern X-ray Physics*. Wiley, 2001.
- [3] ANKUDINOV, A. L., RAVEL, B., REHR, J. J., AND CONRADSON, S. D. Real-space multiple-scattering calculation and interpretation of x-ray-absorption near-edge structure. *Phys. Rev. B* 58 (Sep 1998), 7565–7576.
- [4] ATTWOOD, D. *Soft X-Rays and Extreme Ultraviolet Radiation: Principles and Applications*. Cambridge University Press, 2000.
- [5] BARRETT, R., KAULICH, B., SALOME, M., AND SUSINI, J. Current status of the scanning x-ray microscope at the esrf. *AIP Conference Proceedings* 507, 1 (2000), 458–463.
- [6] BEAUCHEMIN, S., HESTERBERG, D., AND BEAUCHEMIN, M. Principal component analysis approach for modeling sulfur k-xanes spectra of humic acids. *Soil Science Society of America Journal* 66 (2002), 83 – 91.
- [7] BECKHOFF, B., KANNGIESSER, B., LANGHOFF, N., WEDELL, R., AND WOLFF, H. *Handbook of Practical Xray Fluorescence Analysis*. SpringerLink : Bücher. Springer London, Limited, 2006.
- [8] BIANCONI, A. Surface x-ray absorption spectroscopy: Surface exafs and surface xanes. *Applications of Surface Science* 6, 3-4 (1980), 392–418.
- [9] BLUME, H., HORN, R., BRÜMMER, G., KANDELER, E., KOGEL-KNABNER, I., KRETZSCHMAR, R., KÖGEL-KNABNER, I., STAHR, K., WILKE, B., SCHACHTSCHABEL, P., ET AL. *Scheffer/Schachtschabel: Lehrbuch der Bodenkunde*. Spektrum Lehrbuch. Spektrum Akademischer Verlag, 2010.
- [10] BUNKER, G. *Introduction to XAFS*. Cambridge University Press, 2010.
- [11] CHANTLER, C., OLSEN, K., DRAGOSET, R., CHANG, J., KISHORE, A., KOTOCHIGOVA, S., AND ZUCKER, D. X-ray form factor, attenuation, and scattering tables. <http://www.nist.gov/pml/data/ffast/index.cfm>.
- [12] DE GROOT, F., AND KOTANI, A. *Core Level Spectroscopy of Solids*. Advances in Condensed Matter Science. Taylor & Francis, 2008.
- [13] DEHMER, J. L. Evidence of effective potential barriers in the x-ray absorption spectra of molecules. *The Journal of Chemical Physics* 56, 9 (1972), 4496–4504.
- [14] FENDORF, S. *Synchrotron methods in clay science*, vol. 9 of *CMS Workshop lectures*. The Clay Minerals Society, Boulder, CO, 1999, ch. Fundamental aspects and applications of x-ray absorption spectroscopy in clay and soil science.

- [15] FIGUEIREDO, M., SILVA, T. O., AND PEREIRA. Effect of oxygen sharing on the white line of s k-edge xanes spectra of sulphate minerals. *European Journal of Mineralogy* 21, 1 (02 2009), 79–83.
- [16] FLEET, M. E. Xanes spectroscopy of sulfur in earth materials. *The Canadian Mineralogist* 43, 6 (2005), 1811 – 1838.
- [17] FOOD, AND OF THE UNITED NATIONS, A. O. *World reference base for soil resources, 2006: a framework for international classification, correlation and communication*. World soil resources reports. Food and Agriculture Organization of the United Nations, 2006.
- [18] FRANK, P., GEORGE, S. D., ANXOLABÉHÈRE-MALLART, E., HEDMAN, B., AND HODGSON, K. O. A systematic resolution of sulfur in reticulated vitreous carbon using x-ray absorption spectroscopy. *Inorganic Chemistry* 45, 24 (2006), 9864–9876.
- [19] FRANK, P., HEDMAN, B., AND HODGSON, K. O. Sulfur allocation and vanadium? sulfate interactions in whole blood cells from the tunicate ascidia ceratodes, investigated using x-ray absorption spectroscopy. *Inorganic Chemistry* 38, 2 (1999), 260–270.
- [20] FUER STADTENTWICKLUNG UND UMWELT, B. S. Umweltatlas berlin. http://www.stadtentwicklung.berlin.de/umwelt/umweltatlas/da204_06.htm.
- [21] GEORGE, G. N., AND GORBATY, M. L. Sulfur k-edge x-ray absorption spectroscopy of petroleum asphaltenes and model compounds. *Journal of the American Chemical Society* 111, 9 (1989), 3182–3186.
- [22] HUFFMAN, G. P., MITRA, S., HUGGINS, F. E., SHAH, N., VAIDYA, S., AND LU, F. Quantitative analysis of all major forms of sulfur in coal by x-ray absorption fine structure spectroscopy. *Energy & Fuels* 5, 4 (1991), 574–581.
- [23] HUNDAL, L. S., CARMO, A. M., BLEAM, W. L., AND THOMPSON, M. L. Sulfur in biosolids-derived fulvic acid:? characterization by xanes spectroscopy and selective dissolution approaches. *Environmental Science & Technology* 34, 24 (2000), 5184–5188.
- [24] ID21. Esrf database. <http://www.esrf.eu/UsersAndScience/Experiments/Imaging/ID21/php/allbase>.
- [25] JALILEHVAND, F. Sulfur: not a "silent" element any more. *Chem. Soc. Rev.* 35 (2006), 1256–1268.
- [26] JR., N. E. P., MEITZNER, G., AND LOVE, K. M. Identification of sulfate in natural carbonates by x-ray absorption spectroscopy. *Geochimica et Cosmochimica Acta* 59, 12 (1995), 2477 – 2483.
- [27] KLYSUBUN, W., SOMBUNCHOO, P., DEENAN, W., AND KONGMARK, C. Performance and status of beamline BL8 at SLRI for X-ray absorption spectroscopy. *Journal of Synchrotron Radiation* 19, 6 (Nov 2012), 930–936.
- [28] KLYSUBUN, W., TARAWARAKARN, P., SOMBUNCHOO, P., KLINKHIEO, S., CHAIPRAPA, J., AND SONGSIRIRITTHIGUL, P. X-ray absorption spectroscopy beamline at the siam photon laboratory. *AIP Conference Proceedings* 879, 1 (2007), 860–863.
- [29] KONINGSBERGER, D., AND PRINS, R. *X-Ray Absorption: Principles, Applications, Techniques of EXAFS, SEXAFS and XANES*. Chemical Analysis: A Series of Monographs on Analytical Chemistry and Its Applications. Wiley, 1988.

- [30] LI, D., BANCROFT, G. M., KASRAIA, M., FLEET, M. E., FENG, X., AND TAN, K. S. k- and l-edge x-ray absorption spectroscopy of metal sulfides and sulfates; applications in mineralogy and geochemistry. *The Canadian Mineralogist* 33 (1995), 949–960.
- [31] LONGA, S., SOLDATOV, A., POMPA, M., AND BIANCONI, A. Atomic and electronic structure probed by x-ray absorption spectroscopy: Full multiple scattering analysis with the g4xanes package. *Computational Materials Science* 4, 3 (1995), 199 – 210.
- [32] LOUISNATHAN, S., HILL, R., AND GIBBS, G. Tetrahedral bond length variations in sulfates. *Physics and Chemistry of Minerals* 1 (1977), 53–69.
- [33] MACDOWELL, A. A., HASHIZUME, T., AND CITRIN, P. H. A soft/hard x-ray beamline for surface exafs studies in the energy range 0.8–15 kev. *Review of Scientific Instruments* 60, 7 (1989), 1901–1904.
- [34] MAJZLAN, J., AND MYNENI, S. C. B. Speciation of iron and sulfate in acid waters: aqueous clusters to mineral precipitates. *Environmental Science & Technology* 39, 1 (2005), 188–194. PMID: 15667094.
- [35] MALINOWSKI, E. *Factor analysis in chemistry*. Wiley, 2002.
- [36] MALINOWSKI, E. R. Theory of error for target factor analysis with applications to mass spectrometry and nuclear magnetic resonance spectrometry. *Analytica Chimica Acta* 103, 4 (1978), 339 – 354.
- [37] MANCEAU, A., AND NAGY, K. L. Quantitative analysis of sulfur functional groups in natural organic matter by xanes spectroscopy. *Geochimica et Cosmochimica Acta* 99, 0 (2012), 206 – 223.
- [38] McNULTY, I., FENG, Y., FRIGO, S. P., AND MOONEY, T. M. Multilayer spherical grating monochromator for 1- to 4-kev x rays. *SPIE Proceedings* 3150 (1997), 195 – 204.
- [39] McNULTY, I., PATERSON, D., ARKO, J., ERDMANN, M., FRIGO, S. P., GOETZE, K., ILINSKI, P., KRAPP, N., MOONEY, T., RETCH, C. C., STAMPFL, A. P. J., VOGT, S., WANG, Y., AND XU, S. The 2- ! d-b intermediate-energy scanning x-ray microscope at the aps. *Journal de Physique IV (Proceedings)* 104 (2003), 11 – 15.
- [40] MEKIFFER, B. *Eigenschaften urbaner Boeden Berlins - Statistische Auswertung von Gutachtendaten und Fallbeispiele*. PhD thesis, Fakultät IV - Planen Bauen Umwelt, Technische Universität Berlin, 2008.
- [41] MYNENI, S. C. B. Soft x-ray spectroscopy and spectromicroscopy studies of organic molecules in the environment. *Reviews in Mineralogy and Geochemistry* 49, 1 (2002), 485–579.
- [42] OKUDE, N., NAGOSHI, M., NORO, H., BABA, Y., YAMAMOTO, H., AND SASAKI, T. P and s k-edge xanes of transition-metal phosphates and sulfates. *Journal of Electron Spectroscopy and Related Phenomena* 101-103 (1999), 607 – 610.
- [43] ORTHOUS-DAUNAY, F.-R., QUIRICO, E., LEMELLE, L., BECK, P., DEANDRADE, V., SIMIONOVICI, A., AND DERENNE, S. Speciation of sulfur in the insoluble organic matter from carbonaceous chondrites by xanes spectroscopy. *Earth and Planetary Science Letters* 300, 3-4 (2010), 321 – 328.

- [44] PICKERING, I. J., PRINCE, R. C., DIVERS, T., AND GEORGE, G. N. Sulfur k-edge x-ray absorption spectroscopy for determining the chemical speciation of sulfur in biological systems. *FEBS Letters* 441, 1 (1998), 11 – 14.
- [45] PICKERING, I. J., PRINCE, R. C., GEORGE, G. N., RAUSER, W. E., WICKRAMASINGHE, W., WATSON, A. A., DAMERON, C. T., DANCE, I. G., FAIRLIE, D. P., AND SALT, D. E. X-ray absorption spectroscopy of cadmium phytochelatin and model systems. *Biochimica et Biophysica Acta (BBA) - Protein Structure and Molecular Enzymology* 1429, 2 (1999), 351 – 364.
- [46] PRIETZEL, J., BOTZAKI, A., TYUFEKCHIEVA, N., BRETTHOLLE, M., THIEME, J., AND KLYSUBUN, W. Sulfur speciation in soil by s k-edge xanes spectroscopy: Comparison of spectral deconvolution and linear combination fitting. *Environmental Science & Technology* 45, 7 (2011), 2878–2886.
- [47] PRIETZEL, J., THIEME, J., NEUH”AUSLER, U., SUSINI, J., AND K”OGEL-KNABNER, I. Speciation of sulphur in soils and soil particles by x-ray spectromicroscopy. *European Journal of Soil Science* 54, 2 (2003), 423–433.
- [48] PRIETZEL, J., THIEME, J., SALOMÉ, M., AND KNICKER, H. Sulfur k-edge xanes spectroscopy reveals differences in sulfur speciation of bulk soils, humic acid, fulvic acid, and particle size separates. *Soil Biology and Biochemistry* 39, 4 (2007), 877 – 890.
- [49] RAVEL, B., AND NEWVILLE, M. Athena, artemis, hephaestus: data analysis for x-ray absorption spectroscopy using ifeffit. *Journal of Synchrotron Radiation* 12, 4 (Jul 2005), 537–541.
- [50] REHR, J., AND ANKUDINOV, A. Progress in the theory and interpretation of xanes. *Coordination Chemistry Reviews* 249, 1 - 2 (2005), 131 – 140. [jce:title;Synchrotron Radiation in Inorganic and Bioinorganic Chemistry|/ce:title;.](#)
- [51] REHR, J. J., AND ALBERS, R. C. Theoretical approaches to x-ray absorption fine structure. *Rev. Mod. Phys.* 72 (Jul 2000), 621–654.
- [52] RESSLER, T., WONG, J., ROOS, J., AND SMITH, I. L. Quantitative speciation of mn-bearing particulates emitted from autos burning (methylcyclopentadienyl)manganese tricarbonyl-added gasolines using xanes spectroscopy. *Environmental Science & Technology* 34, 6 (2000), 950–958.
- [53] SARANGI, R., FRANK, P., HODGSON, K. O., AND HEDMAN, B. When identical functional groups are not identical: A dft study of the effects of molecular environment on sulfur k-edge x-ray absorption spectra. *Inorganica Chimica Acta* 361, 4 (2008), 956 – 964. Protagonists in Chemistry: Professor Edward I Solomon.
- [54] SARRET, G., CONNAN, J., KASRAI, M., BANCROFT, G., CHARRIÉ-DUHAUT, A., LEMOINE, S., ADAM, P., ALBRECHT, P., AND EYBERT-BÉRARD, L. Chemical forms of sulfur in geological and archeological asphaltenes from middle east, france, and spain determined by sulfur k- and l-edge x-ray absorption near-edge structure spectroscopy. *Geochimica et Cosmochimica Acta* 63, 22 (1999), 3767 – 3779.
- [55] SAYERS, D., LYTLE, F., AND STERN, E. Point scattering theory of x-ray k-absorption fine structure. In *Advances in X-Ray Analysis*, B. Henke, J. Newkirk, and G. Mallett, Eds. Springer US, 1970, pp. 248–271.

- [56] SCHAEFERS, F., MERTIN, M., AND GORGOI, M. Kmc-1: A high resolution and high flux soft x-ray beamline at bessy. *REVIEW OF SCIENTIFIC INSTRUMENTS* 78, 12 (DEC 2007).
- [57] SCHAETZL, R., AND ANDERSON, S. *Soils*. Cambridge University Press, 2005.
- [58] SEKIYAMA, H., KOSUGI, N., KURODA, H., AND OHTA, T. Sulfur k-edge absorption spectra of Na_2SO_4 , Na_2SO_3 , $\text{Na}_2\text{S}_2\text{O}_3$, and $\text{Na}_2\text{S}_2\text{O}_x$ ($x = 5 - 8$). *Bulletin of the Chemical Society of Japan* 59, 2 (1986), 575–579.
- [59] SOLÉ, V., PAPILLON, E., COTTE, M., WALTER, P., AND SUSINI, J. A multiplatform code for the analysis of energy-dispersive x-ray fluorescence spectra. *Spectrochimica Acta Part B: Atomic Spectroscopy* 62, 1 (2007), 63 – 68.
- [60] SOLOMON, E., AND LEVER, A. *Inorganic Electronic Structure and Spectroscopy: Applications and Case Studies*. Inorganic Electronic Structure and Spectroscopy. John Wiley & Sons, 1999.
- [61] SOLOMON, E. I., HEDMAN, B., HODGSON, K. O., DEY, A., AND SZILAGYI, R. K. Ligand k-edge x-ray absorption spectroscopy: covalency of ligand-metal bonds. *Coordination Chemistry Reviews* 249, 1 - 2 (2005), 97 – 129. [jce:title;Synchrotron Radiation in Inorganic and Bioinorganic Chemistry|/ce:title;](#)
- [62] STERN, E. A. Theory of the extended x-ray-absorption fine structure. *Phys. Rev. B* 10 (Oct 1974), 3027–3037.
- [63] STERN, E. A., AND HEALD, S. M. X-ray filter assembly for fluorescence measurements of x-ray absorption fine structure. *Review of Scientific Instruments* 50, 12 (1979), 1579–1582.
- [64] STEVENSON, F., AND COLE, M. *Cycles of Soils: Carbon, Nitrogen, Phosphorus, Sulfur, Micronutrients*. Wiley, 1999.
- [65] STOEHR, J. *Nexafs Spectroscopy*. Springer Series in Surface Sciences. Springer-Verlag, 1992.
- [66] SUSINI, J., SALOMÉ, M., FAYARD, B., ORTEGA, R., AND KAULICH, B. The scanning x-ray microprobe at the esrf "x-ray microscopy" beamline. *Surface Review and Letters* 09, 01 (2002), 203–211.
- [67] SZILAGYI, R. K., FRANK, P., DEBEER GEORGE, S., HEDMAN, B., AND HODGSON, K. O. High covalence in CuSO_4 and the radicalization of sulfate: an x-ray absorption and density functional study. *Inorganic Chemistry* 43, 26 (2004), 8318–8329. PMID: 15606178.
- [68] TAKAHASHI, Y., KANAI, Y., KAMIOKA, H., OHTA, A., MARUYAMA, H., SONG, Z., AND SHIMIZU, H. Speciation of sulfate in size-fractionated aerosol particles using sulfur k-edge x-ray absorption near-edge structure. *Environmental Science & Technology* 40, 16 (2006), 5052–5057.
- [69] THIEME, J., PRIETZEL, J., TYUFEKCHIEVA, N., PATERSON, D., AND McNULTY, I. Speciation of sulfur in oxic and anoxic soils using x-ray spectromicroscopy. *IPAP Conference Series* 7 (2006), 318–320.
- [70] TWINING, B. S., BAINES, S. B., FISHER, N. S., MASER, J., VOGT, S., JACOBSEN, C., TOVAR-SANCHEZ, A., AND SANUDO-WILHELMY, S. A. Quantifying trace elements in individual aquatic protist cells with a synchrotron x-ray fluorescence microprobe. *Analytical Chemistry* 75, 15 (2003), 3806–3816.

- [71] ULERY, A., AND DREES, L. *Methods of Soil Analysis, Part 5: Mineralogical Methods*. Soil Science Society of America book series. Soil Science Society of America, 2008.
- [72] VAIRAVAMURTHY, A. Using x-ray absorption to probe sulfur oxidation states in complex molecules. *Spectrochimica Acta Part A: Molecular and Biomolecular Spectroscopy* 54, 12 (1998), 2009 – 2017.
- [73] VAIRAVAMURTHY, A., ZHOU, W., EGLINTON, T., AND MANOWITZ, B. Sulfonates: A novel class of organic sulfur compounds in marine sediments. *Geochimica et Cosmochimica Acta* 58, 21 (1994), 4681 – 4687.
- [74] VAN LOON, W. M. G. M., BOON, J. J., AND DE GROOT, B. Quantitative analysis of sulfonic acid groups in macromolecular lignosulfonic acids and aquatic humic substances by temperature-resolved pyrolysis-mass spectrometry. *Environmental Science & Technology* 27, 12 (1993), 2387–2396.
- [75] VOGT, S. Maps : A set of software tools for analysis and visualization of 3d x-ray fluorescence data sets. *Journal de Physique IV (Proceedings) IV France* 104 (2003), 635 – 639.
- [76] WALDO, G. S., CARLSON, R. M., MOLDOWAN, J., PETERS, K. E., AND PENNER-HAHN, J. E. Sulfur speciation in heavy petroleums: Information from x-ray absorption near-edge structure. *Geochimica et Cosmochimica Acta* 55, 3 (1991), 801 – 814.
- [77] WEBB, S. M. Sixpack: a graphical user interface for xas analysis using ifeffit. *Physica Scripta* 2005, T115 (2005), 1011.
- [78] WENDE, H. Recent advances in x-ray absorption spectroscopy. *Reports on Progress in Physics* 67, 12 (2004), 2105.
- [79] XIA, K., WEESNER, F., BLEAM, W. F., HELMKE, P. A., BLOOM, P. R., AND SKYLLBERG, U. L. Xanes studies of oxidation states of sulfur in aquatic and soil humic substances. *Soil Science Society of America Journal* 62, 5 (1998), 1240 – 1246.

A. Appendix

A.1. Standard database

chemical name	formula	formal oxidation state	white line energy [eV]	concentration weight-%	source
Aluminum sulfate	$\text{Al}_2(\text{SO}_4)_3$	+6	2482.5	0.1	own data
Ammonium sulfate	$(\text{NH}_4)_2\text{SO}_4$	+6	2482.5	0.1	own data
Barium sulfate	BaSO_4	+6	2482.5	0.1	own data
Calcium sulfate	CaSO_4	+6	2482.5	0.1	own data
Calcium sulfate, Anhydrite	CaSO_4	+6	2482.5	0.1	own data
Calcium sulfate	CaSO_4	+6	2482.5	1	own data
Calcium sulfate	CaSO_4	+6	2482.5	10	own data
Calcium sulfate	CaSO_4	+6	2482.5	100	own data
Copper(II) sulfate	CuSO_4	+6	2482.5	0.1	own data
Iron(II) sulfate	FeSO_4	+6	2482.5	0.1	own data
Iron-oxyhydroxysulfate, Schwertmannite	$\text{Fe}_8\text{O}_8(\text{OH})_6(\text{SO}_4) \cdot n\text{H}_2\text{O}$	+6	2482.5	0.1	own data
Jarosite	$\text{KFe}_3^{3+}(\text{OH})_6(\text{SO}_4)_2$	+6	2482.5	0.1	own data
Magnesium sulfate	MgSO_4	+6	2482.5	0.1	own data
Potassium sulfate	K_2SO_4	+6	2482.5	0.1	own data
Sodium dodecyl sulfate	$\text{NaC}_{12}\text{H}_{25}\text{SO}_4$	+6	2482.5	0.1	own data
Sodium dodecyl sulfate	$\text{NaC}_{12}\text{H}_{25}\text{SO}_4$	+6	2482.5	0.1	own data
Sodium sulfate	Na_2SO_4	+6	2482.5	0.1	own data
Strontium sulfate	SrSO_4	+6	2482.5	0.1	own data
Tin(II) sulfate	SnSO_4	+6	2482.5	0.1	own data
Zinc sulfate	ZnSO_4	+6	2482.5	0.1	own data
Iron(III) sulfate	$\text{FeSO}_4 \cdot 7\text{H}_2\text{O}$	+6	2482.2	unknown	ESRF database
Anthraquinone sulfonic acid	$\text{C}_{14}\text{H}_7\text{NaO}_5\text{S}$	+5	2481.3	unknown	ESRF database
Anthraquinone sulfonic acid	$\text{C}_{14}\text{H}_7\text{NaO}_5\text{S}$	+5	2481.3	0.1	own data
Anthraquinone sulfonic acid	$\text{C}_{14}\text{H}_7\text{NaO}_5\text{S}$	+5	2481.3	1	own data

chemical name	formula	formal oxidation state	white line energy [eV]	concentration weight-%	source
Anthraquinone sulfonic acid	C ₁₄ H ₇ NaO ₅ S	+5	2481.3	10	own data
Anthraquinone sulfonic acid	C ₁₄ H ₇ NaO ₅ S	+5	2481.3	100	own data
Poly...sulfonat		+5	2481.3	0.1	own data
Dithio...di		+5	2481.1	0.1	own data
Sodium methanesulfonate	CH ₃ SO ₃ Na	+4	2481.1	unknown	ESRF database
L-cysteic acid	C ₃ H ₇ NO ₅ S·H ₂ O	+5	2480.9	unknown	ESRF database
DL-methionine sulfoxide	C ₅ H ₁₁ NO ₃ S	+2	2480.8	unknown	ESRF database
Sodium thiosulfate	Na ₂ S ₂ O ₃ ·5H ₂ O	+6	2480.7	unknown	ESRF database
second peak		-2	2471.8		
DL-methionine sulfone	C ₅ H ₁₁ NO ₄ S	+4	2479.8	unknown	ESRF database
Sodium Sulfite	Na ₂ SO ₃	+4	2478.0	0.1	own data
Dimethylsulfoxide	C ₂ H ₆ SO	+2	2476.3	0.1	own data
Dimethylsulfoxide	C ₂ H ₆ SO	+2	2476.3	unknown	ESRF database
Methionine sulfoxide	C ₅ H ₁₁ NO ₃ S	+2	2476.3	0.1	own data
Taurine	C ₂ H ₇ NO ₃ S	+5	2476.2	unknown	ESRF database
DL methionine methyl sulfonium chloride	C ₆ H ₁₄ NO ₂ ClS	+1	2475.3	unknown	ESRF database
Polyphenylene sulfide	C ₆ H ₅ S	+0.5	2474.8	unknown	ESRF database
second peak			2473.4		
Phenylene disulfide	C ₁₂ H ₁₀ S ₂	+0.2	2474.3	unknown	ESRF database
second peak			2472.5		
L-cystine	C ₆ H ₁₂ N ₂ O ₄ S ₂	0	2474.1	unknown	ESRF database
second peak			2472.5		
L-cystine	C ₆ H ₁₂ N ₂ O ₄ S ₂	0	2474.1	0.1	own data
second peak			2472.5		

chemical name	formula	formal oxidation state	white line energy [eV]	concentration weight-%	source
Thianthrene	C ₁₂ H ₈ S ₂	0.5	2474.0	unknown	ESRF database
Dibenzothiophene	C ₁₂ H ₈ S	0	2473.8	unknown	ESRF database
Methionine	C ₅ H ₁₁ NO ₂ S	0	2473.5	unknown	ESRF database
Methionine	C ₅ H ₁₁ NO ₂ S	0	2473.5	0.1	own data
Glutathion reduced	C ₁₀ H ₁₇ N ₃ O ₆ S	-1	2473.4	unknown	ESRF database
S-methyl-L-cysteine	C ₄ H ₉ NO ₂ S	-1	2473.4	unknown	ESRF database
L-cysteine	C ₃ H ₇ NO ₂ S	-1	2473.3	unknown	ESRF database
L-cysteine	C ₃ H ₇ NO ₂ S	-1	2473.3	0.1	own data
L-cysteine	C ₃ H ₇ NO ₂ S	-1	2473.3	1	own data
L-cysteine	C ₃ H ₇ NO ₂ S	-1	2473.3	10	own data
L-cysteine	C ₃ H ₇ NO ₂ S	-1	2473.3	100	own data
Sulfur, elemental	S	0	2472.5	unknown	ESRF database
Iron(II) sulfide, Marcasite	FeS ₂	-1	2472.4	unknown	ESRF database
Mercury chlorine sulfide	Hg ₃ S ₂ Cl ₂	-2	2472.2	unknown	ESRF database
Alpha-lipoic acid	C ₈ H ₁₄ O ₂ S ₂	0	2472.1	unknown	ESRF database
Iron(II) sulfide, Pyrite	FeS ₂	-1	2472.1	unknown	ESRF database
Iron(II) sulfide, Pyrite	FeS ₂	-1	2472.1	0.1	own data
Mercury sulfide	HgS	-2	2471.9	unknown	ESRF database
Antimony sulfide	Sb ₂ S ₃	-2	2471.8	unknown	ESRF database
Arsenic(III) sulfide	As ₂ S ₃	-2	2471.6	unknown	ESRF database
Iron(II) sulfide, Troilite	FeS	-2	2470.8	unknown	ESRF database
Iron (II) sulfide, Pyrrhotite	Fe ₇ S ₈	-2	2470.2	unknown	ESRF database

Table A.1.: All standard spectra used in this work.

A.2. Resins

product name	manufacturer	homepage
Agar	Agar Scientific Ltd.	www.agarscientific.com
Araldite	Bodo Möller Chemie GmbH	www.bm-chemie.de
Araldite easy	Bodo Möller Chemie GmbH	www.bm-chemie.de
EpoFix	STRUERS GmbH	http://www.struers.com
Kallocryl	SPEIKO - Dr. Speier GmbH	www.speiko.de
Kalloplast	SPEIKO - Dr. Speier GmbH	www.speiko.de
LR-White	Polysciences Incorporation	www.polysciences.com
SpeciFix	STRUERS GmbH	www.struers.com
Technovit fast	Heraeus Kulzer GmbH	www.heraeus-kulzer-technik.de
Technovit regular	Heraeus Kulzer GmbH	www.heraeus-kulzer-technik.de

Table A.2.: List of tested resins; manufacturers.

A.3. Embedding procedure LR-White

Prior to embedding, samples are dehydrated in ethanol series:

- $\frac{1}{2}$ h in 15 %
- $\frac{1}{2}$ h in 30 %
- $\frac{1}{2}$ h in 50 %
- $\frac{1}{2}$ h in 70 %
- 1 h in 90 %
- 1 h in 99 %
- at least 12 h in 99 %

Then, samples are stepwise soaked in LR-White:

- 18 h in 1 : 2 (LR-White:ethanol), fridge
- 18 h in 2 : 1 (LR-White:ethanol), fridge
- 18 h in pure LR-White, fridge
- 2 h in pure LR-White, room temperature
- 1 h, 46°C
- 24 h, 60°C

LR-White needs to polymerize (last three steps) in a closed container, because it is sensitive to air.

Acknowledgements

Zuerst möchte ich mich bei dem Betreuer meiner Arbeit, Dr. Jürgen Thieme bedanken, für das spannende Projekt, die angenehme Arbeitsatmosphäre und dafür, dass er auch nach seinem Umzug in die USA fast immer für mich erreichbar war. Außerdem für die Unterstützung bei Messzeiten und spannende Messreisen.

Großer Dank gilt außerdem meinem Doktorvater Prof. Dr. Tim Salditt, für die Möglichkeit, meine Doktorarbeit an seinem Institut anzufertigen.

Ich bedanke mich bei PD Dr. Simone Techert dafür, dass sie das Koreferat meiner Arbeit übernommen hat.

Insbesondere danke ich der DFG für die finanzielle Unterstützung. Diese Arbeit ist aus dem Projekt "Mechanismen der Sulfatfreisetzung aus Trümmerschuttböden" entstanden.

Ich danke Dr. Beate Mekiffer und Prof. Dr. Gerd Wessolek für die Zusammenarbeit am Trümmerschuttprojekt. Besonderer Dank gilt Beate für die Probennahme sowie die Präparation vieler Bodenproben, für viele nette Gespräche und die weitere Unterstützung als sie die Uni schon verlassen hatte.

Herzlicher Dank gilt Dr. Julia Sedlmair für die Unterstützung bei vielen Messzeiten, die witzige Zeit im gemeinsamen Büro und diverse außeruniversitäre Aktivitäten.

Ich danke Dr. Sophie-Charlotte Gleber für das Lesen von Manuskripten, die Unterstützung bei Messzeitanträgen und die Hilfe bei und sogar Übernahme von Messzeiten, sowie für ihre Gastfreundschaft.

Besonderer Dank gilt Wolfgang Dröse für die Einweisung und Hilfe bei den Dünnschnitten, besonders dafür, dass ich zu jeder Zeit auch kurzfristig sein Labor nutzen konnte.

Ich danke apl. Prof. Dr. Jörg Prietzel für viele aufschlussreiche Gespräche und stets prompten E-Mail-Antworten.

Herzlicher Dank gilt den Mitarbeitern an allen Synchrotrons bzw. Beamlines für die nette Einweisung und Betreuung sowie die angenehme Atmosphäre während der Messzeiten und einige nächtliche Einsätze. Insbesondere danke ich Dr. Wantana Klysubun und Dan Legnini.

Lebenslauf

PERSÖNLICHE ANGABEN

Name	Mareike Mathes, geb. Brettholle
Geburtsdatum	15. Dezember 1979
Geburtsort	Ostercappeln

AUSBILDUNG

Schulbildung	
1999	Abitur (Note 1,9), Söderblom Gymnasium Espelkamp

Berufsausbildung	
August 1999 - Juni 2001	Ausbildung zur Bauzeichnerin im Tief-, Stra"sen- und Landschaftsbau bei der Firma H. Dieckmann GmbH & Co. KG in Osnabrück

Studium	
2001 - 2003	Grundstudium der Physik / Phys. Technologien an der TU Clausthal
Oktober 2003	Vordiplom (Note "gut")
2003 - 2007	Hauptstudium der Physik / Phys. Technologien an der TU Clausthal
August - November 2004	Praktikum bei der Firma Multibrid in Bremerhaven: "Einfluss des Schalleintrags von Offshore-Windenergieanlagen auf marine Säugetiere"
Januar - April 2006	Aufenthalt am RISE (Research Institute for Sustainable Energy), angegliedert an die Murdoch University Perth, Australia Studienarbeit: "Inverter influence on the system performance of renewable energy systems"
November 2007	Diplom (Note 1,2)

	<p>Diplomarbeit: "Plasmaelektrochemische Herstellung von metallischen Nanopartikeln in Ionischen Flüssigkeiten - Aufbau und Inbetriebnahme der Apparatur", AG Endres</p> <p>gefördert im DFG Schwerpunktprogramm "Ionische Flüssigkeiten"</p> <p>ausgezeichnet mit dem Bunsen-Bücherpreis 2008</p>
Oktober 2008 - September 2013	Promotionsstudium an der Georg-August-Universität Göttingen, GAUSS-Programm
Mai 2013	Disputation

BERUFSTÄTIGKEIT

Juni 2001 - Oktober 2001	Angestellte Bauzeichnerin bei H. Dieckmann GmbH & Co. KG im Bereich Vermessung und Abrechnung
Dezember 2007 - Juni 2008	<p>Wissenschaftliche Mitarbeiterin an der TU Clausthal, AG Kempter</p> <p>Tätigkeit: Integration einer elektrochemischen Zelle in eine vorhandene UHV-Anlage zur Oberflächenanalyse</p>
Juni 2008 - Oktober 2008	<p>Wissenschaftliche Mitarbeiterin an der FU Berlin, AG Rühl</p> <p>Tätigkeit: Untersuchung der Kristallisation von übersättigten Salzlösungen mittels IR-Spektroskopie und Röntgenspektromikroskopie</p>
Oktober 2008 - März 2013	<p>Wissenschaftliche Mitarbeiterin an der Georg-August-Universität Göttingen, AG Salditt</p> <p>Tätigkeit: Untersuchung der Sulfatfreisetzung von Trümmerschutt in Böden mittels Röntgenspektroskopie, -mikroskopie und -fluoreszenz</p>